

Cover Page



Universiteit Leiden



The handle <http://hdl.handle.net/1887/20828> holds various files of this Leiden University dissertation.

**Author:** Hausmann, Jens

**Title:** Structural and biochemical characterization of autotaxin

**Issue Date:** 2013-04-18

**STRUCTURAL AND BIOCHEMICAL  
CHARACTERIZATION OF AUTOTAXIN**

**Jens Hausmann**

Für meine Familie

## PROMOTIECOMMISSIE

Promoter: Prof. Dr. W.H. Moolenaar

Copromoter: Dr. A. Perrakis

Overige leden: Prof. Dr. J.J. Neefjes  
Prof. Dr. A.J. Morris  
Prof. Dr. H. Ovaa  
Prof. Dr. P.J. Peters  
Prof. Dr. T.K. Sixma

---

ISBN: 978-94-6182-255-0

Layout and printing: Off Page, [www.offpage.nl](http://www.offpage.nl)

Cover: Light at the end of the tunnel

Copyright © 2013 by J. Hausmann. All rights reserved. No part of this book may be reproduced, stored in a retrieval system, or transmitted in any form or by any means, without prior permission of the author.

The work described in this thesis was performed at the Division of Biochemistry of the Netherlands Cancer Institute, Amsterdam, The Netherlands. Financial support was provided by the Netherlands Organization for Scientific Research (NWO), the Dutch Cancer Society and predoctoral fellowship by Pfizer and the Netherlands Cancer Institute.

The printing of the thesis was financially supported by the OOA Graduate School and the Netherlands Cancer Institute.

---

# STRUCTURAL AND BIOCHEMICAL CHARACTERIZATION OF AUTOTAXIN

PROEFSCHRIFT

ter verkrijging van de graad  
van Doctor aan de Universiteit Leiden,  
op gezag van de Rector Magnificus prof. mr. P.F. van der Heijden,  
volgens besluit van het College voor Promoties  
te verdedigen op donderdag 18 april 2013  
klokke 13:45 uur

door

Jens Hausmann  
geboren te Bochum in 1979



## TABLE OF CONTENTS

<b>Chapter 1</b>	General introduction: Structure-function relationships of autotaxin	7
<b>Chapter 2</b>	Mammalian cell expression, purification, crystallization and microcrystal data collection of autotaxin/ENPP2, a secreted mammalian glycoprotein	23
<b>Chapter 3</b>	Structural basis for substrate discrimination and integrin binding by autotaxin	37
<b>Chapter 4</b>	Structural snapshots of autotaxin/ENPP2 and their implications for catalysis	63
<b>Chapter 5</b>	Summary and Discussion	79
<b>Addendum</b>		85
	Nederlandse Samenvatting	87
	Curriculum Vitae	89
	List of Publications	91
	Acknowledgements	93





GENERAL INTRODUCTION:  
STRUCTURE-FUNCTION RELATIONSHIPS  
OF AUTOTAXIN

Adapted from *Adv Biol Regul* 53 (2013) 112–117

## ABSTRACT

Autotaxin (ATX or ENPP2) is an ectonucleotide pyrophosphatase/phosphodiesterase (ENPP) that functions as a secreted lysophospholipase D to produce the multifunctional lipid mediator lysophosphatidic acid (LPA) from more complex lysophospholipids. LPA acts on distinct G protein-coupled receptors thereby activating multiple signaling cascades and cellular responses. The ATX-LPA signaling axis is implicated in a remarkably wide variety of physiological and pathological processes, ranging from vascular and neural development to lymphocyte homing, fibrosis and cancer. Despite much progress in understanding LPA receptor signaling, the precise mode of ATX action has long remained elusive due to the lack of structural data. In particular, it has been unclear what makes ATX a unique lysophospholipase D and how the enzyme is targeted to LPA-responsive cells. Recent structural studies have begun to clarify these issues. Here we discuss new insights and inferences from the ATX structure.

---

Jens Hausmann, Anastassis Perrakis & Wouter H. Moolenaar

---

## ATX

In 1992, Mary Stracke and coworkers at the NIH were the first to describe an autocrine cell motility factor derived from the human melanoma cell line A2058, and named it autotaxin (ATX)<sup>1</sup>. ATX, the product of the *ENPP2* gene, is a secreted 125 kDa extracellular glycoprotein, present in various body fluids<sup>2,3</sup>, such as blister fluid<sup>4</sup>, cerebro-spinal fluid<sup>5,6</sup>, plasma<sup>7</sup>, peritoneal fluid<sup>8</sup>, serum<sup>9,10</sup>, urine<sup>10</sup> and synovial fluid<sup>11</sup>. In 2002, by two independent studies, it became evident, that ATX is the plasma lysophospholipase D (lysoPLD)<sup>12,13</sup>, that hydrolyzes lysophosphatidylcholine (LPC) into lysophosphosphatidic acid (LPA) and choline<sup>14</sup>. LPA is a multifunctional signaling lipid that activates many intracellular pathways by binding to specific G-protein-coupled receptors (LPA<sub>1-6</sub>)<sup>15</sup>. The ATX-LPA signaling axis is involved in physiological processes such as proliferation, cell survival, wound healing, platelet aggregation, inflammation, as well as vascular and neuronal development. It is also associated with multiple pathophysiological conditions, ranging from tumor progression and metastasis to fibrotic diseases and neuropathic pain. As a serum-borne protein, ATX is easily accessible and due to its versatile enzymatic activities to generate various LPA species from different substrate precursors, an attractive target for therapeutic intervention. It is therefore being studied by academia and industry alike.

### The physiology and pathophysiology of the ATX-LPA signaling axis

The ATX-LPA signaling axis has multiple properties in many physiological processes. Important physiological aspects of the ATX-LPA signaling axis have been revealed by the ATX knock-out mice, which die at embryonic day 9.5 with severe problems in the formation of functional blood vessels<sup>16</sup>. None of the known LPA receptor knockout mice (LPA<sub>1</sub>, LPA<sub>2</sub>, LPA<sub>3</sub> and LPA<sub>4</sub>) could account for this phenotype and, moreover, even mice with a triple knockout of LPA<sub>1-3</sub> did not show this phenotypic symptom and were in fact viable<sup>17</sup>. The single loss of the LPA<sub>1</sub> receptor showed developmental effects in the central nervous system and an overall 50% perinatal death rate<sup>18,19</sup>. The constitutive loss of LPA<sub>3</sub> in mice resulted in delayed and abnormal embryo implantation in the uterus<sup>20,21</sup>. The LPA<sub>3</sub> receptor is also implied in immature dendritic cell migration<sup>22</sup>. LPA<sub>4</sub> gene deletion leads to defects in lymphatic vessel development. Further cell culture studies revealed defects in cell motility for this LPA<sub>4</sub> null background<sup>23</sup>. LPA<sub>1</sub> knockout is protected against fibrosis. The targeted deletion of either LPA<sub>1</sub> or LPA<sub>3</sub> identified its involvement in neuropathic pain<sup>24</sup>. Loss of LPA<sub>6</sub> is implicated in human hair growth disorders.

Increased levels of ATX have been correlated with cancer, adipogenesis<sup>25</sup> and cholestatic pruritus<sup>26</sup>. Additionally, LPA<sub>1</sub> has been implicated in the initiation of neuropathic pain<sup>27</sup> and fibrosis in kidney<sup>28</sup> and lung<sup>29</sup>. LPA<sub>2</sub> has been connected to intestinal cancer<sup>30</sup> and lung function in asthma<sup>31</sup>. The homozygous deletion of LPA<sub>6</sub> has been implicated in bladder cancer development<sup>32</sup>.

### ATX, the ENPP enzyme family and substrate diversity

ATX belongs to the family of ecto-nucleotide pyrophosphatases/phosphodiesterases (ENPPs), which encompasses seven family members (ENPP1-7)<sup>33</sup>. ATX is the second family member and therefore also known as ENPP2. The enzyme family can be divided into two subgroups, namely ENPP1-3 and ENPP4-7<sup>34</sup>. ENPP1-3 share the principle domain arrangement of two N-terminal somatomedin B (SMB)-like domains, a central catalytic phosphodiesterase (PDE) domain and a C-terminal inactive nuclease (NUC)-like domain. The second subgroup, ENPP4-7, has

only a single PDE domain in common<sup>33,34</sup>. Apart from ATX, which is exclusively secreted<sup>35</sup>, the remaining six family members can be found on the cell surface, either as type-I (ENPP4-7) or as type-II (ENPP1 and ENPP3) transmembrane proteins (Fig.1)<sup>33,36-39</sup>. Furthermore, ENPP1 was recently found to exist as a secreted fraction next to the membrane bound form<sup>40</sup>. This study also revealed that secreted ENPP1 is the putative consequence of an intracellular proteolytic processing, which chops off the N-terminus till Lys85, including the transmembrane region.

The substrate specificity of the ENPP family members is very diverse: ENPP1-3 recognize (di) nucleotides and their derivatives, as well as lysophospholipids in case of ATX (lysophospholipase D activity)<sup>33</sup>. ENPP6 and ENPP7 accept choline phosphate ester substrates like LPC, but they hydrolyze it to monoacylglycerol and choline phosphate (lysophospholipase C activity). At present, the substrates of ENPP4 and ENPP5 are not known (Fig. 1).

ATX produces LPA from a diverse set of lipid substrate precursors like the LPC, but also from lysophosphatidylserine (LPS) and lysophosphatidylethanolamine (LPE). It does not seem to discriminate between the lipid headgroups (Fig. 2), as indicated by roughly the same catalytic efficiency<sup>41,42</sup>. Apart from the headgroup, the lysolipid substrates of ATX vary not only in acyl chain length and saturation, but also in the position of the acyl chain substitution (sn1 vs. sn2). Moreover, ATX can also hydrolyze sphingosylphosphorylcholine (SPC) into sphingosine1-

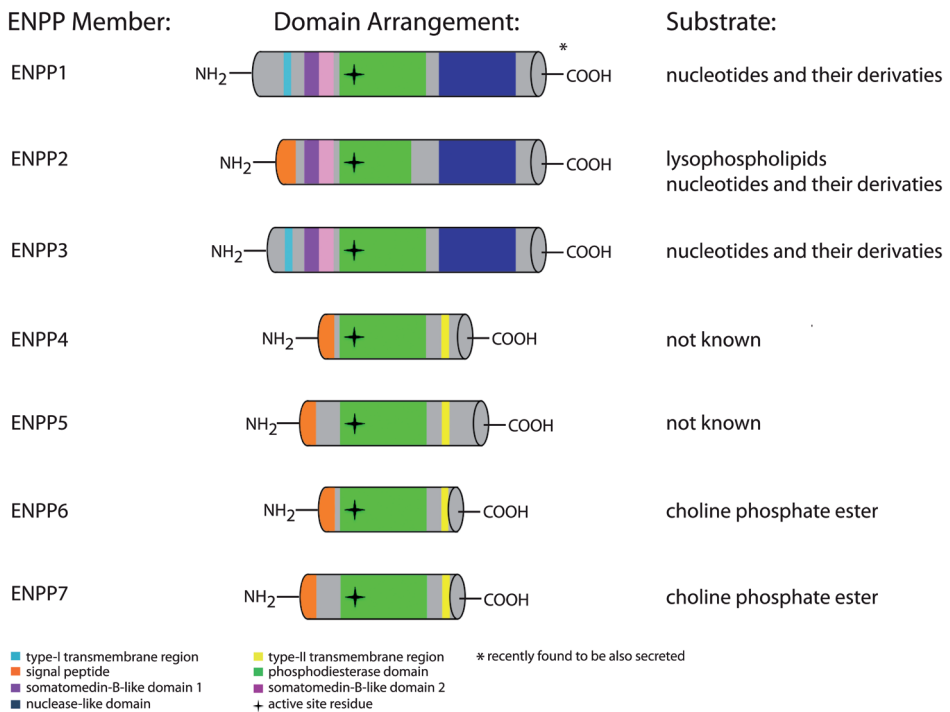


**Fig. 1: Schematic domain presentation of ENPP enzyme family.** The domains (middle column) are colored according to the legend for the individual ENPP member (left column). The known substrates for each family member are indicated in the right column. This figure is adapted from Stefan *et al.*, 2005.

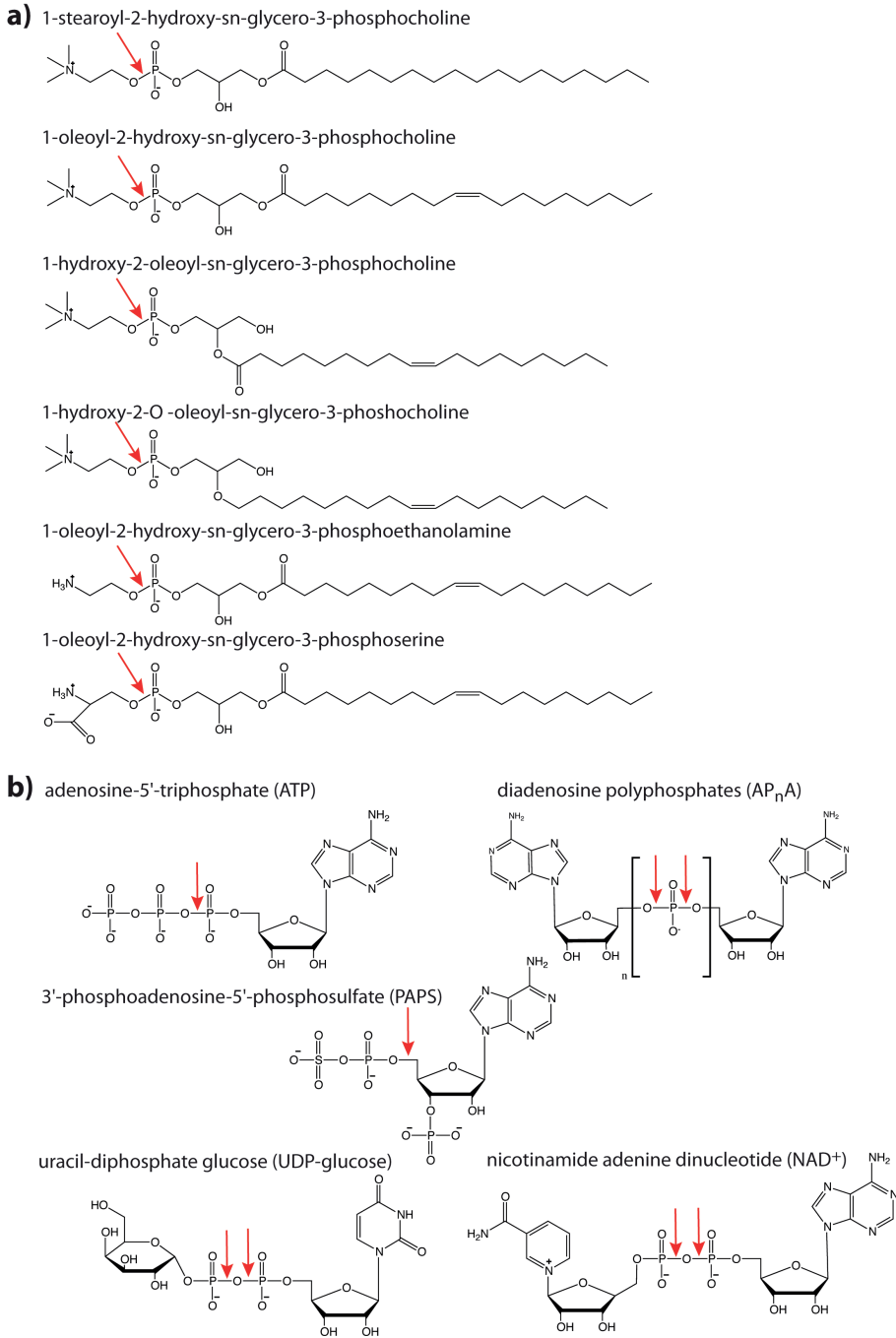


**Fig. 2: Accepted substrates of ATX.** (a) Diversity of lipid substrates for the hydrolysis by ATX to generate LPA. (b) Diversity of the nucleotide substrates. The red arrows indicate the bonds that ATX cleaves. Alternative bond cleavage sites are presented with a second red arrow.

phosphate (S1P). S1P is chemically similar to LPA and shows comparable signaling properties. However, S1P stimulates its own G-protein coupled receptors, termed S1P<sub>1-5</sub>. Currently, there exist no evidence that ATX generates S1P *in vivo*, as S1P is mainly considered to be produced by the phosphorylation of sphingosine by sphingosine kinase<sup>43</sup>. Furthermore, at least *in vitro*, ATX shows catalytic activity towards nucleotides and their derivatives, accepting natural substrates such as ATP, UDP-glucose, NAD<sup>+</sup>, Ap<sub>n</sub>A, and 3'Phosphoadenosine-5'-phosphosulfate (Fig. 2)<sup>44,45</sup>.

### The isoforms of ATX

In mice and humans, four different isoforms of ATX, namely ATX  $\alpha$ ,  $\beta$ ,  $\gamma$  and  $\delta$ , are detected<sup>46,47</sup>. These isoforms result from alternative splicing of *ENPP2*, which generates human ATX $\alpha$  with a length of 915 aa, ATX $\beta$  with 863 aa, ATX $\gamma$  with 889aa and ATX $\delta$  with 859 aa. These splicing variants of *ENPP2* are characterized by a lack of exon 21 for ATX $\alpha$  and of exon 12 for ATX $\gamma$ . ATX $\beta$  and ATX $\delta$ , both miss exon 12 and 21. All four isoforms of ATX are differentially expressed. ATX $\alpha$  shows the overall lowest expression in the central nervous system and in the peripheral tissue. ATX $\beta$  is the best-studied isoform of ATX with high expression in the peripheral tissue and lower expression in the central nervous system. ATX $\gamma$  is mainly expressed in the central nervous system. Within the group of ATX isoforms, ATX $\alpha$  catches one's eye, as it has a 52 amino acid long polybasic insert in the middle of the catalytic domain, including a functional protease cleavage site. The insert of ATX $\alpha$  is shown to be cleaved by the endoprotease furin, however ATX $\alpha$  remains functionally intact, as observed by comparable enzyme kinetics of ATX $\alpha$  and  $\beta$ . After proteolytic cleavage the overall structural stability of N- and C-terminal fragments of ATX $\alpha$  is secured by an extensive interface. This interface is stabilized by van der Waals, hydrogen and ionic interactions, as well as an interfragmental disulfide linkage.

### Overview on the crystal structures of ATX

The domain structure of ATX comprises known folds, but *in silico* predictions have failed to model the relative domain orientation correctly<sup>48</sup>. The surprisingly compact architecture of ATX was revealed by the crystal structures (Fig. 3)<sup>49,50</sup>. The central element of the ATX structure is the PDE domain, which interacts with both SMB domains on one side and the NUC domain on the opposite side, giving ATX a plate-like three-dimensional appearance. The domain arrangement between the PDE and NUC domain is stabilized by four important structural features, namely (i) the interdomain disulfide bond and (ii) the "lasso loop" (iii) the N-linked glycan chain at Asn524 (iv) the C-terminal  $\alpha$ -helix. The disulfide bridge between Cys413 and Cys805 also connects the PDE domain directly to the Nuc domain<sup>49-51</sup> and has a crucial contribution to the fold stability of ATX. The "lasso-loop" extends from the end of the PDE domain and wraps almost around the entire NUC domain. Both, the essential glycan chain of Asn524 and the C-terminal  $\alpha$ -helix (residue 844-859) reinforce the stability of the fold by contributing to the generation of an extensive hydrogen bonding network in the interface between the PDE and NUC domain<sup>49,50,52</sup>. Due to these structural features, the connection between the PDE and NUC domain is stabilized<sup>49,50</sup>. The fold of the PDE domain of ATX is energetically unfavorable and most likely unstable. Thus, evolution had to select for these interactions to ensure a functional enzyme. The ATX structure represents beautifully the long way nature undertook to evolve it.

## The catalytic phosphodiesterase domain and the active site

All ENPP family members share a common catalytic PDE domain of about 400 amino acids (Fig. 1)<sup>33,44,36</sup>. So far structural data of ENPP family members are only available for ATX<sup>49,50</sup> and the recently solved crystal structures of ENPP1<sup>40,53</sup>. Both ATX and ENPP1 have a PDE domain fold that is similar to other members of the alkaline phosphatase (AP) superfamily<sup>45,53</sup>. The AP superfamily groups a diverse set of metalloenzymes<sup>54</sup>, such as the nucleotide pyrophosphatase from *Xanthomonas axonopodis* ((XaNPP) (2GSN))<sup>55</sup>, but also the name-giving member of the AP superfamily from *Escherichia coli*<sup>56</sup>. The architecture of the active sites of ATX and ENPP1 around the Threonine nucleophile, including the two zinc ions and their coordination shell, is structurally comparable to the active site of XaNPP. The metal ions coordination shell of ATX is constructed by three aspartates (Asp171, Asp311 and Asp358) and three histidines (His315, His359 and His474). All ENPP family members have conserved residues at these positions and moreover the active site residue threonine is also conserved within ENPP1-5 and ENPP7. ENPP6 has a serine as catalytic residue, which is a structural common feature of other members of the AP superfamily. Interestingly, these family members preferably hydrolyze phosphomonoesters. These similarities could suggest a conserved two-step in-line displacement mechanism for ATX and ENPP1, in accordance with other phosphodiesterases and alkaline phosphatase family members (chapter 3)<sup>40</sup>.

## The substrate binding site of ATX

The hydrophilic binding groove next to the active site is a further structurally conserved element between ATX, ENPP1 and XaNPP. For XaNPP, the hydrophilic binding groove was shown to bind the ribose and base moieties of nucleotide products<sup>55</sup> and in ATX it accommodates the glycerol backbone of the lipid products<sup>50</sup>. This shallow groove extends into a hydrophobic pocket, about 15 Å in depth<sup>57</sup>, which is not present in ENPP1 and XaNPP. It is considered to originate from a deletion of an 18-amino acid stretch that is specific to ATX within the ENPP family<sup>40,49,50</sup>. The absence of this deletion in other ENPP family members, suggests that these enzymes possess neither a pocket, nor a tunnel and accordingly, ENPP1 lacks both structural elements of ATX<sup>40,49,50</sup>.

The crystal structures of ATX complexed with LPA molecules of different chain length and saturations have shown that the hydrophobic pocket binds the lipid acyl chain in distinct conformations<sup>50</sup>. These studies revealed that LPAs with saturated alkyl chains (e.g. 16:0, 18:0) bind in the hydrophobic pocket in a more elongated fashion. In contrast to LPAs with unsaturated chains (e.g. 18:1, 18:3 and 22:6), which have a more bent conformation, most likely due to the rigidity the carbon carbon double bond. In case of the ATX-LPA (22:6) complex structure, the aliphatic chain is even positioned in a U-shaped conformation in the hydrophobic pocket. It would be of interest to understand the lipid substrate binding properties of ENPP6 and ENPP7, as both enzymes are expected to lack a hydrophobic pocket, while still being able to hydrolyse lipid substrates like LPC.

At least *in vitro*, ATX shows catalytic activity towards nucleotide substrates, although weaker than ENPP1<sup>40</sup>. Currently, there are no structural complex data available for both ENPP1 and ATX, bound to a nucleotide. However, superposition of ATX and ENPP1 to the AMP-bound complex of XaNPP (PDB 2GSU) might suggest a functionally important role of a loop region<sup>40</sup>. This loop is disordered in ATX, while in ENPP1, the corresponding region is well ordered in crystal structure and in close proximity to an active site bound phosphate<sup>40</sup>. It is suggested that this loop might explain the higher catalytic efficiency of ENPP1 over ATX to hydrolyse nucleotide

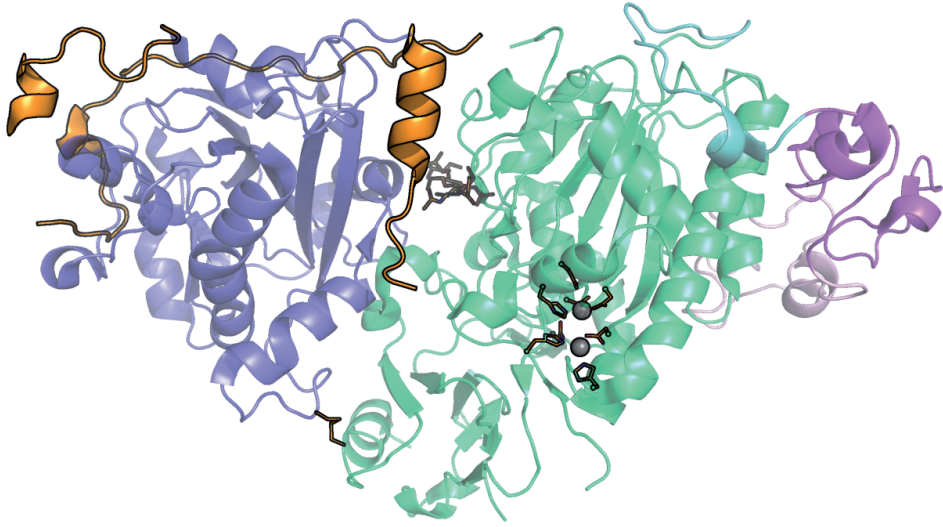


**Fig. 3: The structure of ATX shown as secondary structure representation.** Distinct domains are colored according to the scheme in Fig. 1. Crucial structural stability elements are highlighted in gold. Side chains of important active site residues and zinc ions are depicted in the PDE domain. The image was generated using PyMOL ([www.pymol.org](http://www.pymol.org)) (PDB entry: 2XR9).

substrates, by functioning as “phosphate-capture loop” that could be important for substrate binding to shield the phosphate groups from solvent<sup>40</sup>. Nevertheless, structural binding study data of nucleotidic substrates and products for ENPP1 and ATX are indispensable to grasp the underlying catalytic mechanisms.

### The SMB domains of ATX

SMB domains are relatively small and cysteine-rich domains, which are known to mediate protein-protein interactions. ATX, as well as ENPP1 and ENPP3 have tandem C-terminal SMB domains (SMB1 and SMB2), while ENPP4-7 lack both SMB domains<sup>44</sup>. The known X-ray and NMR structures of the SMB domain from the plasma protein vitronectin (vSMB) are consistent with the principle domain organization of the SMB domains from ATX (chapter 3). The domain organization is achieved by an intrachain disulfide knot with all eight cysteines being arranged in four pairs of crossed disulfide bonds<sup>44,49,58</sup>, which is in agreement with ATX and ENPP1<sup>40,49,50</sup>.

In ATX, the SMB1 domain binds to the PDE domain with a similar surface as the vSMB binds to the plasminogen activator inhibitor-1 (PAI-1) and the urokinase-type plasminogen activator (chapter 3). The SMB2 domain of ATX binds to platelet integrins in a  $\beta$ 3-dependent manner<sup>49,59</sup>. A truncated version of ATX, which only contains the two SMB domains, could still bind to activated platelets<sup>49</sup>. Furthermore, it was shown that the SMB2-mediated complex formation of ATX and platelets integrins accelerates the LPA generation<sup>59</sup>. Currently, it is still unclear how this is exactly achieved on molecular level.

Initially, for ENPP1 the SMB domains were considered to be involved in the homodimerization via interchain disulfide bridges<sup>60,61</sup>. However, recent investigations indicate that the dimerization

is more likely facilitated by transmembrane disulfide bond formations<sup>40</sup>. Consistently, neither ATX nor ENPP3 are so far known to dimerize, although both enzymes possess SMB domains.

Both SMB domains of ATX are connected to the PDE domain via extensive interactions, which locate them in close proximity to the active site, in contrast to the observed SMB domains of ENPP1 that point away from the PDE domain in one monomer of the crystallographic dimer. The SMB domains of the second ENPP1 monomer in this crystal structure disappear in the bulk solvent<sup>40</sup>. These observations suggest a high flexibility of both SMB domains of ENPP1, contradictory to the rigid orientation of the SMB domains observed in different crystal packings of ATX<sup>49,50</sup>. Nevertheless, this stable interaction between the SMB1 and the PDE domain in ATX allow the formation of the tunnel, which is suggested to be an important structural feature of ATX.

### The tunnel of ATX

An unexpected and intriguing observation revealed by the crystal structures is the tunnel of ATX<sup>49,50</sup>. It spans from the active site to the opposite side of ATX (Fig. 4). It connects to the hydrophobic pocket and the catalytic site, thereby shaping the formation of a "T-junction"<sup>34,57</sup>. Residual electron density in the tunnel was detected by Nishimasu *et al.* and us; however, so far this density was not unambiguously modelled. Nishimasu and colleagues used mass spectrometry and detected LPA in their protein preparation used for the crystal structure determination. Additionally, these researchers explored the function of the tunnel by the generation of insertion mutants (LI1-3), which were predicted to occlude the tunnel. When

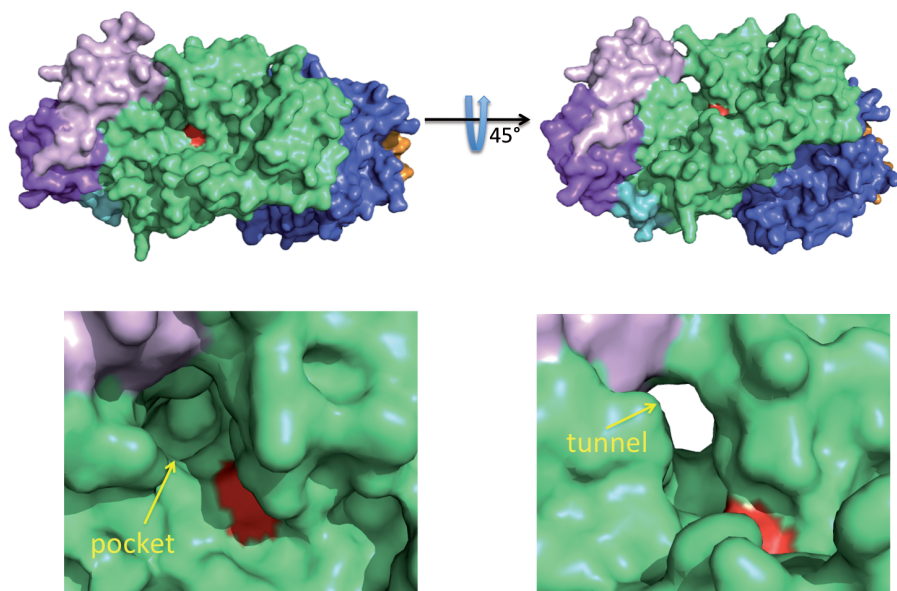


**Fig. 4:** The structure of ATX shown as a surface representation. Distinct domains are colored according to the scheme in Fig. 1. Lower panels: the hydrophobic lipid binding pocket and the open tunnel in the catalytic domain are depicted as close-ups. The Thr nucleophile is colored in red. The images were generated using PyMOL ([www.pymol.org](http://www.pymol.org)) (PDB entry: 2XR9). See text for further details.

compared to wildtype ATX, these mutants had similar nucleotide hydrolysis activities towards pNP-TMP and reduced, but significant lysoPLD activities. Strikingly, the L11-3 mutants showed impaired cell motility. Based on these results, it was concluded that the tunnel might function as an LPA product binding site and that LPA is specifically delivered to its GPCRs via exiting through the tunnel<sup>50</sup>. It is tempting to speculate (based on the close proximity and accessibility of the tunnel to the active site) that it may function as a substrate entry tunnel or product exit channel<sup>34,49,57</sup>, however, a functional role of this unique tunnel still has to be demonstrated.

### Potential cell surface immobilization routes of ATX

LPA production is expected to be spatially and temporally tightly regulated<sup>57</sup>. One way to achieve this can be via the binding of ATX to target cells and thereby producing specific LPA species at the site of action. Different scenarios could fulfill such an immobilization and it was already shown that ATX binds to surface exposed integrin molecules<sup>49,59</sup>. The immobilization of ATX via the binding to cell surface proteoglycans to like heparan sulfate and the direct association of ATX to its cognate GPCRs are hypotheses that remain to be experimentally addressed.

### ATX binding to cell surface integrins

Integrins are cell-surface receptors, which are composed of an  $\alpha$ - and  $\beta$ -subunit. In mammals, 18  $\alpha$  and eight  $\beta$  subunits are known, forming a combination of 24 unique integrins<sup>62</sup>. These 24 integrins mediate cell-cell, cell-extracellular matrix, and cell-pathogen interactions and have been found to have a pivotal role in leukocyte recruitment, phagocytosis and immunological synapse formation<sup>63,64</sup>. Their bidirectional signaling molecule character allows them on one hand to transduce a signal from outside of the cell into the cytosol (outside-in signaling) and on the other hand they can also signal from the cytosol into the extracellular space (inside-out signaling)<sup>63</sup>. The integrin's structure can undergo a conformational change from low to a high ligand affinity state for ligands. The low-affinity state is characterized by an inverted v-shape or bent structure of the extracellular domains, while in the high-affinity state the structure resembles an extended conformation, pointing out far into the extracellular space<sup>62</sup>. Switching from low to high ligand affinity is also known as the activation of integrins. This activation is crucial for the modulation of the extracellular ligand affinity<sup>62</sup>. Generally, the activation of integrins is dependent on the disruption of the non-covalent clasp between the  $\alpha$  and  $\beta$  cytoplasmic integrin tails<sup>65</sup>. In a  $\beta 3$  dependent context, the binding of talin to the cytoplasmic integrin domain can achieve this disruption<sup>65,66</sup>. It was recently revealed that the intracellular G-protein  $G_{\alpha_{13}}$  binds integrin  $\beta 1$  and  $\beta 3$  subunits and mediates integrin outside-in signaling in platelets<sup>67</sup>, supporting the concept of a tight regulation of G-protein subunit and the activation of integrins.

### ATX complexed to leukocyte $\alpha_4\beta_1$

Kanda *et al.* were the first to suggest a complex of ATX to an integrin, namely  $\alpha_4\beta_1$ , which is expressed on leukocytes<sup>68</sup>. This complex formation is thought to be an important step in the recruitment of leukocytes to inflamed tissue<sup>68,69</sup>. Leukocyte recruitment is a multi-event cascade, including the capturing and rolling of leukocytes, mediated predominately by selectins, the slow rolling and arresting to the microvascular endothelium, mainly assured by integrins and finally the transmigration into the site of the cellular destination facilitated by PECAM<sup>64,70</sup>. During

the rolling of leukocytes over endothelium, immune cells are exposed to ligands that trigger G-protein dependent pathways<sup>64</sup>. It is thinkable that specific G-protein subunits subsequently modulate an inside-out signaling event on particular integrins of leukocytes and in turn, the integrins get activated, which leads to high ligand affinity during adhesion.

Until now, the mode of the interaction between ATX and leukocytes is not clear, but it may happens via the canonical  $\alpha 4\beta 1$  <sup>458</sup>LDV<sup>460</sup>-motif on ATX<sup>57</sup>. However, the fact that the formation of the interaction of ATX with leukocytes cannot be inhibited by either integrin-specific antibodies against  $\beta 1$ ,  $\beta 2$  and  $\alpha 4$ , nor integrin-binding peptides (RGD and LDV)<sup>68</sup>, argue for an alternative molecular interaction.

### ATX complexed to $\alpha 11\beta 3/\alpha v\beta 3$

ATX interacts with integrins from platelet and CHO cells in a  $\beta 3$  subunit dependent manner<sup>49,59,71</sup>. Two different  $\beta 3$  containing integrins are localized on the surface of platelets, which are several hundred molecules of  $\alpha v\beta 3$  and about 80000  $\alpha 11\beta 3$  molecules per platelet<sup>72</sup>. Many members of the integrin family, including  $\alpha 5\beta 1$ ,  $\alpha 8\beta 1$ ,  $\alpha v\beta 5$ ,  $\alpha v\beta 6$ ,  $\alpha v\beta 8$ , but also  $\alpha v\beta 3$  and  $\alpha 11\beta 3$  recognize an Arg-Gly-Asp (RGD) motif within their ligands<sup>73</sup>. However, residues outside the RGD motif often provide specificity as well as high affinity for each integrin-ligand pair<sup>74</sup>. ATX contains a <sup>127</sup>RGD<sup>129</sup>-motif in the SMB2 domain and noteworthy even when mutated to AGA the binding to platelet integrins is only marginally reduced<sup>49</sup>. Alanine mutations of Glu109 or His119 show a significantly lower binding of ATX to activated platelets<sup>49,59</sup> and CHO cells overexpressing the  $\beta 3$  subunit<sup>59</sup>.

### ATX $\alpha$ binding to heparin

Another possible way for ATX to bind to target cells is via the immobilization on cell surface proteoglycans. A recent report could show an isoform-dependent, specific binding of ATX $\alpha$  in a low nanomolar range to heparin, whereas binding of ATX $\beta$  could hardly be detected (Houben et al., JBC 288: 510-519, 2013). Interestingly, in these investigations it was reported that the binding of heparin accelerates the lysoPLD activity of ATX $\alpha$  up to two-fold, which could be a result of a lower  $K_d$  value for LPA (18:1) and thus higher catalytic efficiency.

Currently, structural data are only available for ATX $\beta$  and ATX $\delta$ . Both isoforms do not possess this insert. It would be of interest to obtain structural insights of ATX $\alpha$  to understand how the insert exactly mediates high affinity binding to heparin. However, the former described experiments demonstrate the need to test if ATX $\alpha$  binds to heparan sulfate or other proteoglycans on the cell surface.

### ATX binding to GPCRs?

Another hypothetical, but nevertheless tempting mechanism to speculate on, is the immobilization of ATX via binding to LPA<sub>1-6</sub> receptors. According to this concept the tunnel of ATX is thought to support the delivery of LPA to its receptors by functioning as a substrate entry or product exit tunnel. Recently this concept is challenged by structural data from Hanson et al. of the S1P<sub>1</sub> receptor<sup>75</sup>. These researchers found that the lipid binding pocket of S1P<sub>1</sub> is buried in the plasma membrane without an extracellular entry possibility and therefore suggest a likely delivery of S1P into the outer leaflet of the plasmamembrane, a subsequent lateral diffusion of S1P in the cell membrane and an resulting entry into the binding pocket of S1P<sub>1</sub>, that is formed

by the helical segment 1 and 7<sup>75</sup>. In helix 7 Arg292 is of particular interest and it was suggested to support the guidance of the SIP into the binding pocket by functioning as cationic lure, which could direct the lateral diffusion of phospholipids ligands towards the binding pocket<sup>76</sup>. Further experiments will have to validate whether this concept holds also true for the LPA delivery to its receptors and whether ATX has or has not a role in this delivery.

### **ATX Inhibitors**

The upstream position of ATX in the capability to produce of a variety of LPA molecules to modulate a multitude of signaling pathways, as well as the easy accessibility of this serum-derived enzyme, makes it an interesting target for therapeutic intervention and therefore it is being targeted by academia and pharmaceutical industry likewise. Many small molecule inhibitors have been reported in academic and patent literature and these inhibitors have been reviewed elsewhere<sup>45</sup>. However, surprisingly only two nanomolar inhibitors, called HA130<sup>77</sup> and PF8380<sup>78</sup>, were tested for their efficiency *in vivo* so far and at the moment structural data are only available for HA155<sup>49</sup>, an inhibitor based on further development of HA130<sup>45,77</sup>. ATX binds HA155 in a specific way as its warhead boronic acid forms a low energy covalent bond to the O $\gamma$  of the active site residue Thr209<sup>49</sup>. At the other end of HA155, the hydrophobic fluoro-benzene ring is accommodated the hydrophobic lipid binding pocket of ATX<sup>49</sup>. Unfortunately, further specific interaction of ATX with other small molecule inhibitors such as PF8380, are not known yet, due to the lack of structural data. However continuous scientific endeavors will surely accelerate structural advances of inhibitor driven binding modes to ATX, which will lead to further optimized small ligand inhibitors.

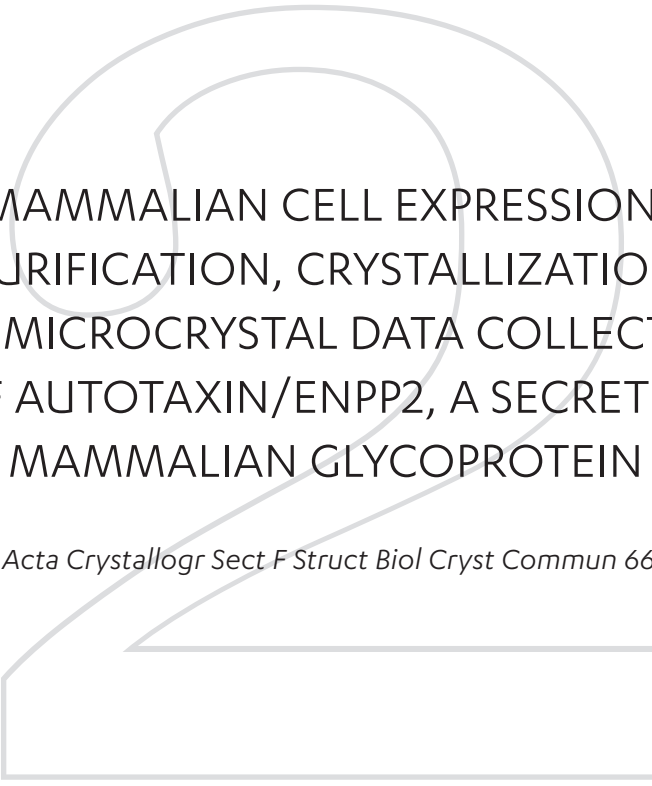
## REFERENCES

1. Stracke, M.L. et al. Identification, purification, and partial sequence analysis of autotaxin, a novel motility-stimulating protein. *J Biol Chem* **267**, 2524-9 (1992).
2. Aoki, J. Mechanisms of lysophosphatidic acid production. *Semin Cell Dev Biol* **15**, 477-89 (2004).
3. Boutin, J.A. & Ferry, G. Autotaxin. *Cell Mol Life Sci* **66**, 3009-21 (2009).
4. Mazereeuw-Hautier, J. et al. Production of lysophosphatidic acid in blister fluid: involvement of a lysophospholipase D activity. *J Invest Dermatol* **125**, 421-7 (2005).
5. Hammack, B.N. et al. Proteomic analysis of multiple sclerosis cerebrospinal fluid. *Mult Scler* **10**, 245-60 (2004).
6. Sato, K. et al. Identification of autotaxin as a neurite retraction-inducing factor of PC12 cells in cerebrospinal fluid and its possible sources. *J Neurochem* **92**, 904-14 (2005).
7. Koh, E., Bandle, R.W., Roberts, D.D., Stracke, M.L. & Clair, T. Novel point mutations attenuate autotaxin activity. *Lipids Health Dis* **8**, 4 (2009).
8. Tokumura, A. et al. Peritoneal fluids from patients with certain gynecologic tumor contain elevated levels of bioactive lysophospholipase D activity. *Life Sci* **80**, 1641-9 (2007).
9. Nakamura, K. et al. Validation of an autotaxin enzyme immunoassay in human serum samples and its application to hypoalbuminemia differentiation. *Clin Chim Acta* **388**, 51-8 (2008).
10. Nakamura, K. et al. Analysis of serum and urinary lysophospholipase D/autotaxin in nephrotic syndrome. *Clin Chem Lab Med* **46**, 150-1 (2008).
11. Nochi, H. et al. Stimulatory role of lysophosphatidic acid in cyclooxygenase-2 induction by synovial fluid of patients with rheumatoid arthritis in fibroblast-like synovial cells. *J Immunol* **181**, 5111-9 (2008).
12. Tokumura, A. et al. Identification of human plasma lysophospholipase D, a lysophosphatidic acid-producing enzyme, as autotaxin, a multifunctional phosphodiesterase. *J Biol Chem* **277**, 39436-42 (2002).
13. Umezu-Goto, M. et al. Autotaxin has lysophospholipase D activity leading to tumor cell growth and motility by lysophosphatidic acid production. *J Cell Biol* **158**, 227-33 (2002).
14. van Corven, E.J., Groenink, A., Jalink, K., Eichholtz, T. & Moolenaar, W.H. Lysophosphatidate-induced cell proliferation: identification and dissection of signaling pathways mediated by G proteins. *Cell* **59**, 45-54 (1989).
15. Noguchi, K., Herr, D., Mutoh, T. & Chun, J. Lysophosphatidic acid (LPA) and its receptors. *Curr Opin Pharmacol* **9**, 15-23 (2009).
16. van Meeteren, L.A. et al. Autotaxin, a secreted lysophospholipase D, is essential for blood vessel formation during development. *Mol Cell Biol* **26**, 5015-22 (2006).
17. Ye, X., Skinner, M.K., Kennedy, G. & Chun, J. Age-dependent loss of sperm production in mice via impaired lysophosphatidic acid signaling. *Biol Reprod* **79**, 328-36 (2008).
18. Contos, J.J., Ishii, I. & Chun, J. Lysophosphatidic acid receptors. *Mol Pharmacol* **58**, 1188-96 (2000).
19. Contos, J.J., Fukushima, N., Weiner, J.A., Kaushal, D. & Chun, J. Requirement for the lpA1 lysophosphatidic acid receptor gene in normal suckling behavior. *Proc Natl Acad Sci U S A* **97**, 13384-9 (2000).
20. Ye, X. et al. LPA3-mediated lysophosphatidic acid signalling in embryo implantation and spacing. *Nature* **435**, 104-8 (2005).
21. Hama, K. et al. Embryo spacing and implantation timing are differentially regulated by LPA3-mediated lysophosphatidic acid signaling in mice. *Biol Reprod* **77**, 954-9 (2007).
22. Chan, L.C. et al. LPA3 receptor mediates chemotaxis of immature murine dendritic cells to unsaturated lysophosphatidic acid (LPA). *J Leukoc Biol* **82**, 1193-200 (2007).
23. Lee, Z. et al. Role of LPA4/p2y9/GPR23 in negative regulation of cell motility. *Mol Biol Cell* **19**, 5435-45 (2008).
24. Lin, M.E., Rivera, R.R. & Chun, J. Targeted deletion of LPA5 identifies novel roles for lysophosphatidic acid signaling in development of neuropathic pain. *J Biol Chem* **287**, 17608-17 (2012).
25. Pradere, J.P., Tarnus, E., Gres, S., Valet, P. & Saulnier-Blache, J.S. Secretion and lysophospholipase D activity of autotaxin by adipocytes are controlled by N-glycosylation and signal peptidase. *Biochim Biophys Acta* **1771**, 93-102 (2007).
26. Kremer, A.E. et al. Serum autotaxin is increased in pruritus of cholestasis, but not of other origin and responds to therapeutic interventions. *Hepatology* (2012).
27. Inoue, M. et al. Lysophosphatidylcholine induces neuropathic pain through an action of

- autotaxin to generate lysophosphatidic acid. *Neuroscience* **152**, 296-8 (2008).
28. Pradere, J.P. et al. LPA1 receptor activation promotes renal interstitial fibrosis. *J Am Soc Nephrol* **18**, 3110-8 (2007).
  29. Tager, A.M. et al. The lysophosphatidic acid receptor LPA1 links pulmonary fibrosis to lung injury by mediating fibroblast recruitment and vascular leak. *Nat Med* **14**, 45-54 (2008).
  30. Lin, S. et al. The absence of LPA2 attenuates tumor formation in an experimental model of colitis-associated cancer. *Gastroenterology* **136**, 1711-20 (2009).
  31. Zhao, Y. et al. Role of lysophosphatidic acid receptor LPA2 in the development of allergic airway inflammation in a murine model of asthma. *Respir Res* **10**, 114 (2009).
  32. Lee, C.W., Rivera, R., Dubin, A.E. & Chun, J. LPA(4)/GPR23 is a lysophosphatidic acid (LPA) receptor utilizing G(s)-, G(q)/G(i)-mediated calcium signaling and G(12/13)-mediated Rho activation. *J Biol Chem* **282**, 4310-7 (2007).
  33. Stefan, C., Jansen, S. & Bollen, M. NPP-type ectophosphodiesterases: unity in diversity. *Trends Biochem Sci* **30**, 542-50 (2005).
  34. Nishimasu, H., Ishitani, R., Aoki, J. & Nureki, O. A 3D view of autotaxin. *Trends Pharmacol Sci* **33**, 138-45 (2012).
  35. Jansen, S. et al. Proteolytic maturation and activation of autotaxin (NPP2), a secreted metastasis-enhancing lysophospholipase D. *J Cell Sci* **118**, 3081-9 (2005).
  36. Gijsbers, R., Ceulemans, H., Stalmans, W. & Bollen, M. Structural and catalytic similarities between nucleotide pyrophosphatases/phosphodiesterases and alkaline phosphatases. *J Biol Chem* **276**, 1361-8 (2001).
  37. Sakagami, H. et al. Biochemical and molecular characterization of a novel choline-specific glycerophosphodiester phosphodiesterase belonging to the nucleotide pyrophosphatase/phosphodiesterase family. *J Biol Chem* **280**, 23084-93 (2005).
  38. Ohe, Y. et al. Characterization of nucleotide pyrophosphatase-5 as an oligomannosidic glycoprotein in rat brain. *Biochem Biophys Res Commun* **308**, 719-25 (2003).
  39. Wu, J., Liu, F., Nilsson, A. & Duan, R.D. Pancreatic trypsin cleaves intestinal alkaline sphingomyelinase from mucosa and enhances the sphingomyelinase activity. *Am J Physiol Gastrointest Liver Physiol* **287**, G967-73 (2004).
  40. Jansen, S. et al. Structure of NPP1, an Ectonucleotide Pyrophosphatase/Phosphodiesterase Involved in Tissue Calcification. *Structure* (2012).
  41. Aoki, J. et al. Serum lysophosphatidic acid is produced through diverse phospholipase pathways. *J Biol Chem* **277**, 48737-44 (2002).
  42. Tokumura, A., Nishioka, Y., Yoshimoto, O., Shinomiya, J. & Fukuzawa, K. Substrate specificity of lysophospholipase D which produces bioactive lysophosphatidic acids in rat plasma. *Biochim Biophys Acta* **1437**, 235-45 (1999).
  43. Clair, T. et al. Autotaxin hydrolyzes sphingosylphosphorylcholine to produce the regulator of migration, sphingosine-1-phosphate. *Cancer Res* **63**, 5446-53 (2003).
  44. Stefan, C., Jansen, S. & Bollen, M. Modulation of purinergic signaling by NPP-type ectophosphodiesterases. *Purinergic Signal* **2**, 361-70 (2006).
  45. Albers, H.M. & Ovaa, H. Chemical evolution of autotaxin inhibitors. *Chem Rev* **112**, 2593-603 (2012).
  46. Giganti, A. et al. Murine and human autotaxin alpha, beta, and gamma isoforms: gene organization, tissue distribution, and biochemical characterization. *J Biol Chem* **283**, 7776-89 (2008).
  47. Hashimoto, T. et al. Identification and biochemical characterization of a novel autotaxin isoform, ATXdelta, with a four-amino acid deletion. *J Biochem* **151**, 89-97 (2012).
  48. Kryshchak, A. et al. Target highlights in CASP9: Experimental target structures for the critical assessment of techniques for protein structure prediction. *Proteins* **79 Suppl 10**, 6-20 (2011).
  49. Hausmann, J. et al. Structural basis of substrate discrimination and integrin binding by autotaxin. *Nat Struct Mol Biol* **18**, 198-204 (2011).
  50. Nishimasu, H. et al. Crystal structure of autotaxin and insight into GPCR activation by lipid mediators. *Nat Struct Mol Biol* **18**, 205-12 (2011).
  51. Jansen, S., Andries, M., Derua, R., Waelkens, E. & Bollen, M. Domain interplay mediated by an essential disulfide linkage is critical for the activity and secretion of the metastasis-promoting enzyme autotaxin. *J Biol Chem* **284**, 14296-302 (2009).
  52. Jansen, S. et al. An essential oligomannosidic glycan chain in the catalytic domain of autotaxin, a secreted lysophospholipase-D. *J Biol Chem* **282**, 11084-91 (2007).

53. Kato, K. et al. Crystal structure of Enpp1, an extracellular glycoprotein involved in bone mineralization and insulin signaling. *Proc Natl Acad Sci U S A* **109**, 16876-81 (2012).
54. Galperin, M.Y., Bairoch, A. & Koonin, E.V. A superfamily of metalloenzymes unifies phosphopentomutase and cofactor-independent phosphoglycerate mutase with alkaline phosphatases and sulfatases. *Protein Sci* **7**, 1829-35 (1998).
55. Zalatan, J.G., Fenn, T.D., Brunger, A.T. & Herschlag, D. Structural and functional comparisons of nucleotide pyrophosphatase/phosphodiesterase and alkaline phosphatase: implications for mechanism and evolution. *Biochemistry* **45**, 9788-803 (2006).
56. Kim, E.E. & Wyckoff, H.W. Reaction mechanism of alkaline phosphatase based on crystal structures. Two-metal ion catalysis. *J Mol Biol* **218**, 449-64 (1991).
57. Moolenaar, W.H. & Perrakis, A. Insights into autotaxin: how to produce and present a lipid mediator. *Nat Rev Mol Cell Biol* **12**, 674-9 (2011).
58. Zhou, A., Huntington, J.A., Pannu, N.S., Carrell, R.W. & Read, R.J. How vitronectin binds PAI-1 to modulate fibrinolysis and cell migration. *Nat Struct Biol* **10**, 541-4 (2003).
59. Fulkerson, Z. et al. Binding of autotaxin to integrins localizes lysophosphatidic acid production to platelets and mammalian cells. *J Biol Chem* **286**, 34654-63 (2011).
60. Bollen, M., Gijssbers, R., Ceulemans, H., Stalmans, W. & Stefan, C. Nucleotide pyrophosphatases/phosphodiesterases on the move. *Crit Rev Biochem Mol Biol* **35**, 393-432 (2000).
61. Gijssbers, R., Ceulemans, H. & Bollen, M. Functional characterization of the non-catalytic ectodomains of the nucleotide pyrophosphatase/phosphodiesterase NPPI. *Biochem J* **371**, 321-30 (2003).
62. Barczyk, M., Carracedo, S. & Gullberg, D. Integrins. *Cell Tissue Res* **339**, 269-80 (2010).
63. Hynes, R.O. Integrins: bidirectional, allosteric signaling machines. *Cell* **110**, 673-87 (2002).
64. Zarbock, A., Kempf, T., Wollert, K.C. & Vestweber, D. Leukocyte integrin activation and deactivation: novel mechanisms of balancing inflammation. *J Mol Med (Berl)* **90**, 353-9 (2012).
65. Shattil, S.J., Kim, C. & Ginsberg, M.H. The final steps of integrin activation: the end game. *Nat Rev Mol Cell Biol* **11**, 288-300 (2010).
66. Anthis, N.J. et al. The structure of an integrin/talin complex reveals the basis of inside-out signal transduction. *EMBO J* **28**, 3623-32 (2009).
67. Gong, H. et al. G protein subunit G $\alpha$ 13 binds to integrin  $\alpha$ IIb $\beta$ 3 and mediates integrin "outside-in" signaling. *Science* **327**, 340-3 (2010).
68. Kanda, H. et al. Autotaxin, an ectoenzyme that produces lysophosphatidic acid, promotes the entry of lymphocytes into secondary lymphoid organs. *Nat Immunol* **9**, 415-23 (2008).
69. Vestweber, D. & Wild, M.K. A new player in lymphocyte homing. *Nat Immunol* **9**, 347-8 (2008).
70. Woodfin, A., Voisin, M.B. & Nourshargh, S. PECAM-1: a multi-functional molecule in inflammation and vascular biology. *Arterioscler Thromb Vasc Biol* **27**, 2514-23 (2007).
71. Pamuklar, Z. et al. Autotaxin/lysopholipase D and lysophosphatidic acid regulate murine hemostasis and thrombosis. *J Biol Chem* **284**, 7385-94 (2009).
72. Bennett, J.S., Berger, B.W. & Billings, P.C. The structure and function of platelet integrins. *J Thromb Haemost* **7 Suppl 1**, 200-5 (2009).
73. Takagi, J., Strokovich, K., Springer, T.A. & Walz, T. Structure of integrin  $\alpha$ 5 $\beta$ 1 in complex with fibronectin. *EMBO J* **22**, 4607-15 (2003).
74. Takagi, J. Structural basis for ligand recognition by RGD (Arg-Gly-Asp)-dependent integrins. *Biochem Soc Trans* **32**, 403-6 (2004).
75. Hanson, M.A. et al. Crystal structure of a lipid G protein-coupled receptor. *Science* **335**, 851-5 (2012).
76. Parrill, A.L., Lima, S. & Spiegel, S. Structure of the first sphingosine 1-phosphate receptor. *Sci Signal* **5**, pe23 (2012).
77. Albers, H.M. et al. Boronic acid-based inhibitor of autotaxin reveals rapid turnover of LPA in the circulation. *Proc Natl Acad Sci U S A* **107**, 7257-62 (2010).
78. Gierse, J.K. et al. A Novel Autotaxin Inhibitor Reduces Lysophosphatidic Acid Levels in Plasma and the Site of Inflammation. *J Pharmacol Exp Ther* (2010).





MAMMALIAN CELL EXPRESSION,  
PURIFICATION, CRYSTALLIZATION  
AND MICROCRYSTAL DATA COLLECTION  
OF AUTOTAXIN/ENPP2, A SECRETED  
MAMMALIAN GLYCOPROTEIN

*Adapted from Acta Crystallogr Sect F Struct Biol Cryst Commun 66, 1130-5 (2010)*

## ABSTRACT

Autotaxin (ATX or ENPP2) is a secreted, glycosylated mammalian enzyme that exhibits lysophospholipase D activity, hydrolyzing lysophosphatidylcholine (LPC) into the signalling lipid lysophosphatidic acid (LPA). ATX is a ~100 kDa multi-domain protein, encompassing two N-terminal somatomedin-B-like domains, a central catalytic phosphodiesterase domain, and a C-terminal nuclease-like domain. We report protocols for the efficient expression of ATX in amounts sufficient for crystallographic studies, from stably transfected mammalian HEK293 cells. Purification resulted in protein that crystallized readily, but various attempts to grow crystals suitable in size for routine crystallographic structure determination were not successful. The available micron-thick plates however diffracted X-rays beyond 2.0 Å and allowed collection of complete diffraction data to about 2.6 Å resolution. We discuss the problems we encountered, and the current advantages and limitations for diffraction data collection from thin crystal plates.

---

Jens Hausmann<sup>1</sup>, Evangelos Christodoulou<sup>1</sup>, Mobien Kasiem, Valeria De Marco, Laurens A. van Meeteren, Wouter H. Moolenaar, Danny Axford, Robin Owen, Gwyndaf Evans & Anastassis Perrakis

<sup>1</sup>These authors contributed equally to this work

---

## INTRODUCTION

Autotaxin (ATX), the second member of ecto-nucleotide phosphodiesterase/pyrophosphatase family (ENPP), is a secreted ~100 kDa glycoprotein<sup>1</sup>. ATX/ENPP2 is classified as a phosphoric diester hydrolase (EC 3.1.4) that displays alkylglycerophosphoethanolamine phosphodiesterase (lysophospholipase D) activity<sup>2</sup> (EC 3.1.4.39). Autotaxin converts extracellular lysophosphatidylcholine (LPC) into lysophosphatidic acid (LPA), a signalling phospholipid acting on at least six distinct G protein-coupled receptors (LPA<sub>1-6</sub>) and eliciting a great variety of both short-term and long-term cellular responses<sup>3</sup>. ATX and LPA signalling are strongly implicated in tumour progression and metastasis, as well as in inflammation, fibrotic disease and neurological disorders<sup>4-6</sup>. As such, ATX holds great promise as a therapeutic target<sup>7</sup>.

ATX harbours a central catalytic domain similar to bacterial phosphodiesterases and alkaline phosphatases. This domain is flanked N-terminally by two Cys-rich somatomedin-B-like (SMB) domains, and C-terminally by a nuclease-like domain. The intact secreted protein is needed for activity and glycosylation has been shown to be crucial for function<sup>8</sup>. We have therefore set out to make ATX in amounts sufficient for crystallographic studies.

Protocols for overexpression of secreted proteins in amounts suitable for crystallographic studies have been established as part of the SPINE consortium<sup>9</sup>. We adapted these protocols and extended them for use of stably transfected cell lines.

Although ATX was easy to crystallize once produced in homogenous form and good quantity, we could only obtain micro-crystals. Despite older<sup>10,11</sup> and more recent advances<sup>12-15</sup> in micro-crystallography, data collection from plate-like crystals presented a challenge which we discuss.

## EXPERIMENTAL PROCEDURES AND RESULTS

### Construction of a stable cell line expressing ATX

A *rATX* construct retaining only one glycosylation site essential for activity<sup>8</sup> was amplified by PCR from plasmid DNA (using 5'-TGGTACCGCCACCATGGCAAGACAAGGCTGTCTC-3' and 5'-ACCGTAATCTCGCTCTCATATGT-3' primers) and the reaction product was cut with Asp718I and AgeI restriction enzymes, and cloned into the plasmid pcDNA3.1/V5-His (Invitrogen) to introduce a C-terminal His6 tag. The *rATX*-His gene was amplified by PCR, (using 5'-TGGTACCGCCACCATGGCAAGACAAGGCTGTCTC-3' and 5'-GGATCCTCAATGGTGA TGGTGATG-3' primers), cut with Asp718I and PstI restriction enzymes and cloned into the plasmid pcDNA5/FRT. Restriction digests were performed for 1h at 37°. PCR reactions were performed using Pfu (Stratagene Cat. Nr. 600353-51) polymerase in 50 µl reactions volumes, using 30 PCR cycles (denaturation 96° for 30s, annealing 55° for 30s, 72° for 120s). All other conditions were according to manufacturer instructions and reaction buffers supplied by the manufacturer. The final clone was verified by sequencing.

HEK 293 Flp-In cells (Invitrogen) were grown in 10-cm tissue culture dishes in DMEM medium (Invitrogen, Cat. Nr. 41966-052) containing 10% FCS (Sigma, Cat. Nr. 8200496835) and 100µg/ml Zeocin (Invitrogen, Cat. Nr. 45-0430). On the day of transfection, the cells (80-90% confluent) were washed with medium without Zeocin and co-transfected with 2µg pcDNA5/FRT-*rATX*-His and 18µg pOG44 (Invitrogen Cat. Nr. K6010-01) using lipofectamine (Invitrogen

Cat. Nr. 18324012). Next day the cells were washed using fresh medium without antibiotics. The following day the cells were split to ~20% confluence in fresh medium containing 100µg/ml Hygromycin B (Invitrogen, Cat. Nr. 10687-010) and allowed to grow for approximately ten days until foci could be identified. Six foci were picked and expanded in T175 tissue culture flasks in DMEM medium containing 10% FCS and 100µg/ml Hygromycin B, to verify resistance in Hygromycin B. Cells were flash frozen in liquid nitrogen for future use.

### Large scale expression

For large scale expression, cells were first grown in T175 tissue culture flasks in DMEM medium containing 10% FCS and 100µg/ml Hygromycin B. Cells were grown to 80-90% confluence, washed twice with fresh DMEM medium, and transferred to roller bottles (GreinerBioOne, Cat. Nr. 681070). Typically a single T175 flask was used to inoculate one roller bottle and the cells were cultured for four days after transfer into 125 ml of DMEM containing 10% FCS. The medium was changed to 125 ml DMEM supplemented with 2 mM Glutamate (GIBCO, Cat.Nr. 25030-123) and the cells were then left to express protein for four days. The medium was collected and the cells were supplemented with fresh medium and left to express protein for a further four days.

### Purification of secreted ATX

The medium was collected, and filtered through a 0.45 µm bottle-top filter. The filtered medium was subsequently applied to a ~10ml POROS-20 MC column, pre-loaded with Ni<sup>2+</sup>, at a flow rate of 10-15 ml/min. The column was washed with eight to ten column volumes of Buffer A (20 mM Tris/HCl pH 8.0, 150 mM NaCl and 10-20 mM imidazole). The protein was eluted with a short (2-3 column volumes) linear gradient to Buffer A containing 750 mM imidazole. The rATX fractions were mostly pure, with the exception of a ~200 kDa band. To remove this band the pooled fractions were concentrated and subsequently applied to a Superose 6 10/30 size exclusion column in Buffer A. rATX eluted as a single symmetric peak at a column volume corresponding to a monomer of ~100 kDa. The peak fractions were pooled and concentrated to ~3-4 mg/ml for crystallization.

Concentration posed a serious practical problem, as rATX would 'stick' in most commonly used centrifugal filters, preventing concentration. We initially resorted to dialysis against 30% PEG 10,000 to concentrate the protein. The use of Ultra-15 (Amicon, 10 kDa MWCO) centrifugal filters however, allowed more efficient concentration later in the course of the project. Preparation of eight roller bottles typically allowed 2-3 mg of protein to be produced.

### Crystallization

rATX was initially crystallized by vapour-diffusion in nano-drops using the protocols summarized in<sup>16</sup>. Crystals in the shape of microscopic plates appeared in many conditions in the PACT screen (described in<sup>16</sup> and manufactured by Qiagen). All conditions that produced initial hits contain PEG by definition, and given the highly redundant nature of the PACT screen, hits appeared in about ten drops; the conditions giving the best crystals were: (B5) 0.1 M MIB buffer pH 8, 25% w/v PEG 1500; (B6) 0.1 M MIB buffer pH 9, 25% w/v PEG 1500; and (E11) 0.2 M Sodium citrate, 20% w/v PEG 3350. Various attempts to improve the size of these crystals failed; the biggest crystals that we were able to grow in these conditions were plates of several tenths of microns across, but sub-micron thick at best.

After additive screening, octanoyl-N-methylglucamide (MEGA-8) appeared to have a positive effect on crystal size. Crystallization in very large drops of a total volume of 10  $\mu$ l produced plate-like crystals of excellent morphology, where the smallest dimension was estimated to be just above 1 micron, Table 1.

Following optimization of the rATX purification protocol additional optimization showed that micron-thick crystals could be grown, without a need for detergent or large drops, in standard SBS format crystallization plates in drops of 300 nl total volume using the Mosquito liquid handling robot. The presence of phosphate ions at concentrations 20-200 mM was crucial for formation of these crystals, which appeared over a wide pH range, and had a morphology identical to the ones produced in the presence of detergent, Table 1. These crystals were formed with or without seeding, although seeding accelerated crystal formation.

In both crystallization protocols, higher concentration of protein correlated well with increased crystal size. However, the practical yields of protein did not allow concentration above a certain limit, which was maximally  $\sim$ 5 mg/ml.

Although we have successfully produced Se-Met substituted protein in the stable HEK-293 cell line, yields were significantly lower due to the toxicity of the Se-methionine, which precluded concentrating the protein enough for growing crystals of size similar to the native.

Crystals were transferred to a solution typically containing 20-25% glycerol in addition to the mother liquor, and mounted in loops. All were vitrified by plunging them in liquid nitrogen, mounted in 'SPINE' pins and transferred into SPINE/ESRF pucks for shipment and data collection at the synchrotron<sup>17</sup>. During the course of about two years, a couple of thousand crystals were mounted, and about a third of these attempts gave single crystals in the loop. Roughly five hundred crystals were tested for diffraction. In total about thirty datasets were collected, and the best data are presented in this paper. The crystals used for these data are shown in Figure 1.

### Collection of diffraction data and analysis

We discuss the measurement of three datasets: two are collected from crystals grown from very large crystallization drops (10 $\mu$ l), one with a micro-beam (10x10  $\mu$ m) and one with a

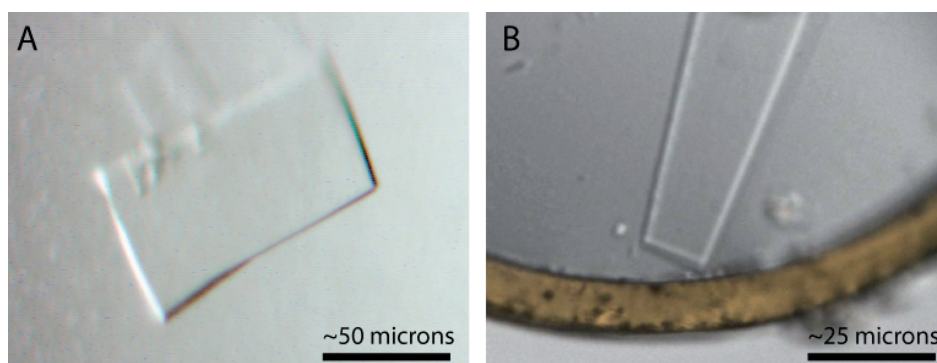


**Fig. 1: The crystals used for data collection.** (A) 'Crystal 2', exposed at the SLS in the crystallization drop and (B) 'Crystal 3', exposed at Diamond as seen at the beamline mounted in a loop and flash-frozen.

**Table 1:** Sample information

Macromolecule details	ENPP2/ATX		
Mass (Da)	98,000		
Source organism	Rattus norvegicus		
Crystallization and crystal data	Crystal 1	Crystal 2	Crystal 3
Crystallization method	Sitting-drop vapour diffusion	Sitting-drop vapour diffusion	Sitting-drop vapour diffusion
Temperature (K)	293	293	293
Crystal growth time	4-5 days	4-5 days	2 days
Crystallization solutions			
Macromolecule	4 $\mu$ l, rATX (3-4 mg ml <sup>-1</sup> ), NaCl (150 mM), tris hydrochloride (pH 8, 20 mM)	4 $\mu$ l, rATX (3-4 mg ml <sup>-1</sup> ), NaCl (150 mM), tris hydrochloride (pH 8, 20 mM)	200 nl, rATX (3-4 mg ml <sup>-1</sup> ), NaCl (150 mM), Tris/HCl (pH 8.0, 20 mM)
Precipitant	5 $\mu$ l, polyethylene glycol 6000 (20%(w/v)), potassium citrate (100 mM), MIB buffer (pH 8.5, 100 mM)	5 $\mu$ l, polyethylene glycol 6000 (18-22%(w/v)), potassium citrate (100 mM), MIB buffer (pH 8.5, 100 mM)	100 nl, polyethylene glycol 3350 ( $\pm$ 20%(w/v)), Bis Tris propane (pH 6.5-8.5, 100 mM)
Additive	1 $\mu$ l of 1 M MEGA-8/10	1 $\mu$ l of 1M MEGA-8/10	20-200 Na/K PO <sub>4</sub>
Crystal data			
Crystal size ( $\mu$ m)	~ 100 $\times$ 50 $\times$ 1	~ 150 $\times$ 30 $\times$ 1	~ 200 $\times$ 30 $\times$ ~1
Matthews coefficient, $V_M$ ( $\text{\AA}^3 \text{Da}^{-1}$ )	2.38	2.38	2.38
Solvent content (%)	48	48	48
Unit-cell data			
Crystal system, space group	Orthorhombic, $P2_12_12_1$	Orthorhombic, $P2_12_12_1$	Orthorhombic, $P2_12_12_1$
a, b, c ( $\text{\AA}$ )	95.3, 121.8, 158.4	96.2, 121.7, 160.0	95.4, 120.2, 157.1
a, b, g ( $^\circ$ )	90, 90, 90	90,90,90	90, 90, 90
No. of molecules in unit cell, Z	2	2	2

typical size beam (40x100  $\mu$ m); the third dataset was collected from crystals grown in small crystallization drops (0.3  $\mu$ l).

### SLS data collection with a micro-diffractometer

A good quality crystal was obtained after extensive screening at the SLS X06SA beamline (PX1) in the setup equipped with the EMBL/ESRF micro-diffractometer<sup>11</sup> and a 10  $\mu$ m beam-defining aperture. Based on experience from previous crystals, we knew they had a limited lifetime. The longer dimension of the crystal was oriented along the rotation axis, to allow translation between successive ‘wedges’ and minimize radiation damage. The first ‘wedge’ of thirty degrees was collected ‘edge-on’, while the last twenty degrees were collected ‘face-on’. It can be seen in Figure 2A and B that in the edge-on orientation the diffraction is strong but spots are imperfect due to crystal imperfections along the long plate axis fully bathed in the beam, while in the ‘face-on’ orientation the diffraction is significantly weaker, but the spots are very small, round-shaped with clear edges, since only a very limited volume of the crystal is exposed. This strategy resulted in a dataset of good quality; the spot intensities were integrated in MOSFLM,

using the 'RESOLUTION CUTOFF 1.0' keyword, that limits the radial integration area in each image to the resolution bin that the average  $I/\sigma(I)$  fell below 1.0. The resulting dataset was complete to about 3.2 Å resolution, and had useful data to 2.6 Å resolution (Table 2).

## SLS DATA COLLECTION WITH A 'TYPICAL' BEAM AND A PILATUS DETECTOR.

At a later data collection trip, a crystal of similar quality, but possibly exceeding 1 µm in thickness, was identified. At that time we were using the SLS 'high-resolution diffractometer' with a beam of approximately 40x100 µm and we were aware that we were missing 'face-on' data from the previous dataset. We were able to only collect 25 degrees of data before the crystal suffered from radiation damage. The data quality statistics for this ~50% complete dataset (Table 2) demonstrate that the crystal plates were of excellent quality with minimal distortion around their surface. We observed that our crystal could withstand a higher X-ray dose in the shutterless data collection mode enabled the Pilatus 6M detector<sup>18</sup>, than in the same beam with the same exposure and a normal CCD detector.

### A combined native data and obstacles in collecting a Se-Met dataset.

Combining the above data, we obtained a dataset to 2.6 Å resolution, (Table 3). This dataset had improved completeness, specifically in the higher resolution shell (69.7% instead of 40.2%)

**Table 2:** Data collection statistics from individual crystals

	Crystal 1	Crystal 2	Crystal 3
Source	SLS/X06SA	SLS/X06SA	Diamond/I24
X-ray beam size	10 x 10 µm	40 x 100 µm	8x8 / 15x20 / 30x50 µm
"Wedges" collected (°)	0-30 / 40-60 / 70-90	0-25	0-10 / 10-50 / 60-100
Detector distance (mm)	300	520.0	535.9
Exposure time (s)	1	1	2
Rotation range/image (°)	1.0	0.25	1.0
Diffraction protocol	Single wavelength	Single wavelength	Single wavelength
Wavelength (Å)	0.933	0.978	0.978
Detector	CCD (Mar225)	Pilatus 6M	Pilatus 6M
Temperature (K)	100	100	100
Resolution range (Å)	50.0-2.6 (2.74-2.6) [3.36-3.11]	50.0-2.6 (2.74-2.6) [3.36-3.11]	50.0-2.6 (2.74-2.6) [3.36-3.11]
No. of unique reflections	46204(3355)	30282(3567)	48210(3048)
No. of observed reflections	120917(6162)	42546(4112)	131664(3748)
Completeness (%)	80.5(40.2)[97.5]	52.9(43.2)[58.8]	86.8(38.6)[97.8]
Redundancy	2.6(1.8)[2.7]	1.4(1.2)[1.4]	2.7(1.2)[3.2]
$\langle I/\sigma(I) \rangle$	4.9(1.6)[3.1]	4.0(1.4)[3.8]	4.5(1.3)[3.7]
$R_{\text{merge}}$	0.180(0.511)[0.371]	0.106(0.299)[0.180]	0.186(0.364)[0.300]
Data-processing software	MOSFLM/SCALA	XDS/SCALA	XDS/SCALA

Values for the outer shell are given in parentheses, and for around 3.2 Å resolution in square brackets (to appreciate the data completeness issues better).

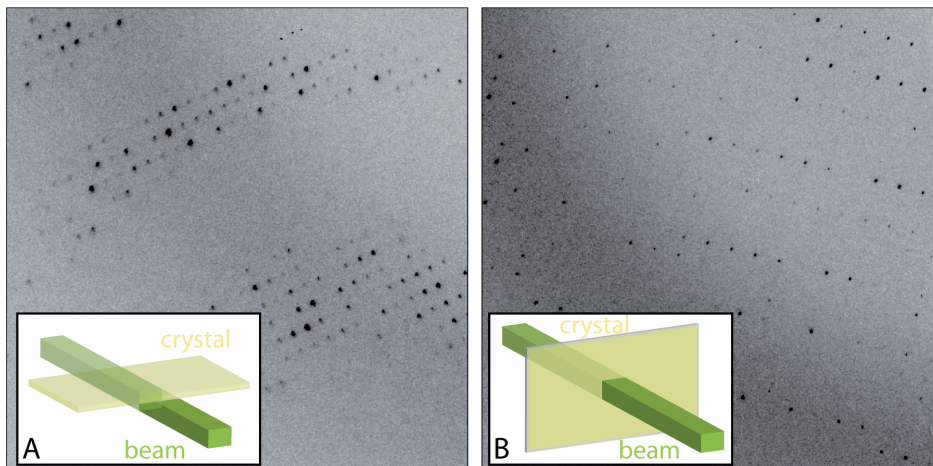


**Fig. 2: Setup for diffraction data collection** (with the beam shown in green and the crystal in yellow) and the corresponding sample diffraction images illustrating the differences in (A) 'edge-on'; and (B) 'face-on' orientations. The size of the beam and crystal in the diagram are approximate.

owing to the contribution of the 25° wedge contributed by the second crystal in the 'face-on' orientation. Although that region was collected for crystal 1 with the micro-beam, the 'face-on' images were diffracting at much lower resolution.

This dataset was used for molecular replacement using as a search model a bacterial phosphodiesterase domain<sup>19</sup>, homologous to one of the four domains of ATX (with 28% identity). Although a clear solution was easily obtained in PHASER<sup>20</sup>, our efforts to refine this model and complete the structure were unsuccessful. The free R factor did not decrease and the electron density maps did not show any features for either the differences between the bacterial and mammalian sequences, or the three domains not present in the search model (~60% of the molecule).

Therefore we focused our attention on obtaining a Se-Met dataset, a quest that failed. This effort was hampered by lack of enough Se-Met protein required for obtaining large enough native crystals. Crystals did not exceed 1 µm in thickness, and the other two plate dimensions were typically less than 40 µm. We were thus unable to allow collection of a redundant and high quality dataset, even to a modest resolution of about ~3.5 Å. Minimizing exposure to increase lifetime led to data that were too weak. While the SAD data we were able to collect from a few small crystals were of reasonable quality, the redundancy was too low (anomalous redundancy 3.7 for our best dataset) to generate a good enough anomalous signal to noise ratio (anomalous correlation dropped below 30% at ~7Å resolution for the best data). Attempts to combine datasets from different crystals did not produce a better anomalous signal to noise ratio. Soaking experiments proved physically difficult to perform due to the small crystal size and did not result in usable data.

#### **Data collection at the Diamond I24 microfocus beamline using variable beam size**

During our attempts to obtain a Se-Met crystal from nano-drops for diffraction studies, we produced native crystals with some alterations in the crystallization protocol (Table 1). The

**Table 3:** Data collection statistics for the combined dataset

	Crystal 1+2
Source	SLS/X06SA
Resolution range (Å)	50.0-2.6 (2.74-2.6) [3.36-3.11]
No. of unique reflections	52092(5747)
No. of observed reflections	162655(10544)
Completeness (%)	91.0 (69.7) [99.0]
Redundancy	3.1 (1.8) [3.4]
$\langle I/\sigma(I) \rangle$	7.7 (1.5) [4.1]
$R_{\text{merge}}$	0.191(0.488)[0.359]
Data-processing software	MOSFLM/SCALA

Values for the outer shell are given in parentheses.

size of these crystals was similar to that of the previous crystals, despite being grown from nano-drops, and they were used to test data collection protocols for subsequent Se-Met data collection at I24, a tuneable microfocus beamline that was at the time in late stages of commissioning at Diamond Light Source. I24's versatile optical design (Evans *et al.*, 2006) allowed the use of three beam sizes, a micro-beam of 8x8 microns, a medium-size beam of 15x20 microns and a larger 30x50 micron beam (v×h). As changes in beamsizes were achieved via the refocusing of mirrors rather than through the use of apertures or defining slits, the total flux at the sample position of  $\sim 10^{12}$  ph/s is preserved for each of these different sized beams. I24 was designed specifically to allow matching of X-ray beam properties to sample properties and in the simplest case this means that, where possible, the beam size is matched to the projected dimensions of the crystal along the beam axis.

For these crystals the beamsizes were adjusted accordingly for different crystal orientations and this allowed a dataset of good quality and completeness to be collected from a single micro-crystal.

## DISCUSSION

### Protein production in stably transfected mammalian cells for crystallographic studies

We have expressed a mammalian glycoprotein in stably transfected HEK-293 cells. Producing a stable cell line with the Flip-in system is straightforward, and allows routine production of protein without the need for transfection, minimizing the routine costs (the cost of large DNA preparations for transfection of large volumes of cell culture as well as the cost of transfection media are eliminated), as well as the uncertainty and heterogeneity of transfection success. Production in roller bottles allows straightforward scale-up of the procedure, at a low cost since the use of FCS is eliminated in final stages. Loading of the medium containing the secreted protein in a fast flow resin, allowed much faster protein purification without prior concentration. Additionally, screening commercial products to find a device that allowed centrifugal protein concentration, was important to be able to concentrate the protein further, faster and in smaller volumes, and enabled more efficient crystallization screening. Finally, we were able to use nano-crystallization vapour diffusion experiments in 0.3  $\mu$ l drops, yielding

excellent quality small crystals, similar to these obtained in 10  $\mu\text{l}$  drops. This is another case in the largely anecdotal line of evidence that argues that drop size does not correlate well with crystal size and quality.

### Limitations of using micron-thick plate-like crystals

Crystallization screening using the vapour diffusion method in nano-drops allowed the production of very small plate-like crystals. Subsequent optimization in very large drops (10  $\mu\text{l}$  total) in the presence of detergent, or later also in nano-drops (0.3  $\mu\text{l}$ ), allowed the formation of micron-thick crystals that were suitable for collecting 2.6  $\text{\AA}$  resolution diffraction data.

Despite recent excellent advances in instrumentation, the manipulation of very thin plate crystals presents clear challenges that need to be resolved. Since plates have a preferred orientation in mounting loops, they are invisible in 'edge-on' orientation, calling for grid-scan procedures<sup>21-23</sup> such as the one available in I24, to determine the ideal centring by diffraction in that orientation.

Furthermore, while a micro-beam is ideal for collecting data at the 'edge-on' orientation, a larger size beam is preferable 'face-on', as illustrated in Figure 3. As an example consider two possible beam sizes, a micro-beam of 10x10  $\mu\text{m}$ , and a more common beamsize of 100x50  $\mu\text{m}$ , being used to measure data from a typical rATX crystal of 100x50x1  $\mu\text{m}$ . Clearly neither situation is optimal. In the 'edge-on' orientation, a micro-beam is best, Figure 3A. With such a thin crystal, in the 'edge-on' orientation the maximal volume is exposed: for the sizes above, at that orientation a volume of  $\sim 500 \mu\text{m}^3$  is exposed (1  $\mu\text{m}$  of crystal thickness x 10  $\mu\text{m}$  of crystal along the long axis across the beam, which is limited by the beam size, x 50  $\mu\text{m}$  of the crystal's other long axis along the beam). At the 'face-on' orientation, only  $\sim 100 \mu\text{m}^3$  of crystal volume would be exposed to the micro-beam, Figure 3B (1  $\mu\text{m}$  of crystal thickness x 10  $\mu\text{m}$  x 10  $\mu\text{m}$  of crystal limited by the beam size in both long crystal directions). However, after a few degrees rotation, one can afford a larger beam, and finally in the 'face-on' orientation, a large beam matching the plate size is best suited, Figure 3D (1  $\mu\text{m}$  of crystal thickness x 100  $\mu\text{m}$  x 50  $\mu\text{m}$  of crystal along the long axes across the beam) and would result in  $\sim 5,000 \mu\text{m}^3$  of crystal being exposed. However, the large beam would result in a too high background in the edge-on orientation, as effectively only 2% of the beam would hit the crystal, Figure 3C. In our opinion, variable beam sizes where the beam size adapts dynamically during data collection could have possibly improved data collection on these crystals.

The availability of a variable beam size at I24 allowed data collection from a single plate crystal even though only three discrete sizes were offered at the time. The data obtained using the grid-scan technique to centre the edge-on orientation and the subsequent use of variable beam sizes resulted in data being measured from a single crystal of a quality comparable to that obtained from two crystals at the SLS X06SA beamline using two different micro-diffractometers. At the time of these experiments only three discrete beam sizes were available at I24 but the design goal for this beamline is continuous, independent, variability of beamsizes in both directions so as to permit optimal adaptation of beam characteristics to the size and orientation of the sample.

We argue here that an X-ray beam that could be changed in size every few degrees throughout a data collection or software that would allow three-dimensional data collection strategies utilizing all the volume of thin plate crystals, a micro-beam, and varying exposure times to account for crystal volume changes, allows more efficient data collection. If the

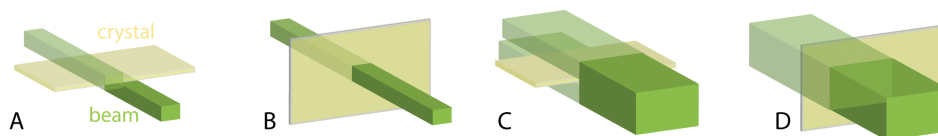


**Fig. 3: A schematic diagram illustrating benefits and problems of small and large beams (shown in green) for plate-like crystals (shown in yellow): (A) thin plate edge-on with micro-beam (good); (B) thin plate face-on with micro-beam (bad); (C) thin plate edge-on with large beam (bad); and (D) thin plate face-on with large beam (good).**

available beam size matches the smallest crystal dimension, micro-crystals, in a way, present the lesser challenge for data collection: the choice is limited to a single volume. Needle-like crystals provide an additional dimension of complexity: to utilize the whole crystal volume a one-dimensional ‘scan’ across the length of the needle is desirable<sup>24</sup>, using a fixed beam size. Plate-like crystals however create a more complex challenge: to utilize the crystal volume efficiently, two-dimensional scanning would be needed, along with variation of the beam size dependent on crystal orientation. Such procedures could have maybe allowed data collection from a single Se-Met crystal of *rATX*, which might in turn have enabled to record the anomalous signals more accurately, to facilitate structure solution. In retrospect, the main obstacle to structure solution from these data was in fact the size of the crystals rather than the diffraction limit or other basic problems.

Determination of the crystal structure of *rATX* was made possible by the addition of two components in the precipitating solution of our ‘basic’ crystallization protocol, and is described separately in the paper by Day *et al* (submitted for publication).

## ACKNOWLEDGEMENTS

J.H and A.P. thank Clemens Schultze-Briese and the scientists at SLS for their expert help and access to the SLS PX1 beamline for the duration of this project, Jonathan Grimes for help in I24/Diamond data collection, and Tom Walter and Karl Harlos for help in crystal growth and mounting.

## REFERENCES

1. Stracke, M.L. et al. Identification, purification, and partial sequence analysis of autotaxin, a novel motility-stimulating protein. *J Biol Chem* **267**, 2524-9 (1992).
2. Umezu-Goto, M. et al. Autotaxin has lysophospholipase D activity leading to tumor cell growth and motility by lysophosphatidic acid production. *J Cell Biol* **158**, 227-33 (2002).
3. vanMeeteren, L.A. & Moolenaar, W.H. Regulation and biological activities of the autotaxin-LPA axis. *Prog Lipid Res* **46**, 145-60 (2007).
4. Fotopoulou, S. et al. ATX expression and LPA signalling are vital for the development of the nervous system. *Dev Biol* **339**, 451-64.
5. Tanaka, M. et al. Autotaxin stabilizes blood vessels and is required for embryonic vasculature by producing lysophosphatidic acid. *J Biol Chem* **281**, 25822-30 (2006).
6. van Meeteren, L.A. et al. Autotaxin, a secreted lysophospholipase D, is essential for blood vessel formation during development. *Mol Cell Biol* **26**, 5015-22 (2006).
7. Albers, H.M. et al. Boronic acid-based inhibitor of autotaxin reveals rapid turnover of LPA in the circulation. *Proc Natl Acad Sci U S A*.
8. Jansen, S. et al. An essential oligomannosidic glycan chain in the catalytic domain of autotaxin, a secreted lysophospholipase-D. *J Biol Chem* **282**, 11084-91 (2007).
9. Aricescu, A.R. et al. Eukaryotic expression: developments for structural proteomics. *Acta Crystallogr D Biol Crystallogr* **62**, 1114-24 (2006).
10. Cusack, S. et al. Small is beautiful: protein micro-crystallography. *Nat Struct Biol* **5 Suppl**, 634-7. (1998).
11. Perrakis, A. et al. Protein microcrystals and the design of a microdiffractometer; current experience and plans at EMBL and ESRF/ID13. *Acta Crystallographica D* **55**(1999).
12. Cherezov, V. et al. Rastering strategy for screening and centring of microcrystal samples of human membrane proteins with a sub-10 microm size X-ray synchrotron beam. *J R Soc Interface* **6 Suppl 5**, S587-97 (2009).
13. Moukhametzianov, R. et al. Protein crystallography with a micrometre-sized synchrotron-radiation beam. *Acta Crystallogr D Biol Crystallogr* **64**, 158-66 (2008).
14. Sanishvili, R. et al. A 7 microm mini-beam improves diffraction data from small or imperfect crystals of macromolecules. *Acta Crystallogr D Biol Crystallogr* **64**, 425-35 (2008).
15. Schneider, T.R. Synchrotron radiation: micrometer-sized x-ray beams as fine tools for macromolecular crystallography. *Hfsp J* **2**, 302-6 (2008).
16. Newman, J. et al. Towards rationalization of crystallization screening for small- to medium-sized academic laboratories: the PACT/JCSG+ strategy. *Acta Crystallogr D Biol Crystallogr* **61**, 1426-31 (2005).
17. Beteva, A. et al. High-throughput sample handling and data collection at synchrotrons: embedding the ESRF into the high-throughput gene-to-structure pipeline. *Acta Crystallogr D Biol Crystallogr* **62**, 1162-9 (2006).
18. Broennimann, C. et al. The PILATUS1M detector. *J Synchrotron Radiat* **13**, 120-30 (2006).
19. Zalatan, J.G., Fenn, T.D., Brunger, A.T. & Herschlag, D. Structural and functional comparisons of nucleotide pyrophosphatase/phosphodiesterase and alkaline phosphatase: implications for mechanism and evolution. *Biochemistry* **45**, 9788-803 (2006).
20. McCoy, A.J. et al. Phaser crystallographic software. *J Appl Crystallogr* **40**, 658-674 (2007).
21. Aishima, J. et al. High-speed crystal detection and characterization using a fast-readout detector. *Acta Crystallogr D Biol Crystallogr* **66**, 1032-5 (2010).
22. Bowler, M.W. et al. Diffraction cartography: applying microbeams to macromolecular crystallography sample evaluation and data collection. *Acta Crystallogr D Biol Crystallogr* **66**, 855-64.
23. Song, J. et al. Diffraction-based automated crystal centering. *J Synchrotron Radiat* **14**, 191-5 (2007).
24. Flot, D. et al. The ID23-2 structural biology microfocus beamline at the ESRF. *J Synchrotron Radiat* **17**, 107-18.







STRUCTURAL BASIS FOR SUBSTRATE  
DISCRIMINATION AND INTEGRIN BINDING  
BY AUTOTAXIN

Adapted from *Nat Struct Mol Biol* 18, 198-204 (2011)

## ABSTRACT

Autotaxin (ATX) or ecto-nucleotide pyrophosphatase/phosphodiesterase-2 (ENPP2) is a secreted lysophospholipase D that generates the lipid mediator lysophosphatidic acid (LPA), a mitogen and chemoattractant for many cell types. ATX-LPA signaling has roles in various pathologies including tumour progression and inflammation. However, the molecular basis of substrate recognition and catalysis, and the mechanism of interaction with target cells, has been elusive. Here we present the crystal structure of ATX, alone and in complex with a small-molecule inhibitor. We identify a hydrophobic lipid-binding pocket and map key residues required for catalysis and selection between nucleotide and phospholipid substrates. We show that ATX interacts with cell-surface integrins via its N-terminal somatomedin-B-like domains, using an atypical mechanism. Our results define determinants of substrate discrimination by the ENPP family, suggest how ATX promotes localized LPA signaling, and enable new approaches to target ATX with small-molecule therapeutics.

---

Jens Hausmann<sup>1</sup>, Satwik Kamtekar<sup>1</sup>, Evangelos Christodoulou, Jacqueline E. Day, Tao Wu, Zachary Fulkerson, Harald M.H.G. Albers, Laurens A. van Meeteren, Anna Houben, Leonie van Zeijl, Silvia Jansen, Maria Andries, Troii Hall, Lyle E. Pegg, Timothy E. Benson, Mobien Kasiem, Karl Harlos, Craig Vander Kooi, Susan S. Smyth, Huib Ovaa, Mathieu Bollen, Andrew J. Morris, Wouter H. Moolenaar & Anastassis Perrakis

<sup>1</sup>These authors contributed equally to this work

---

## INTRODUCTION

Autotaxin (ATX), also known as ecto-nucleotide pyrophosphatase/phosphodiesterase 2 (ENPP2), is a secreted glycoprotein<sup>2</sup> that acts as a lysophospholipase D (lysoPLD), converting lysophosphatidylcholine (LPC) into the lipid mediator lysophosphatidic acid (LPA)<sup>3,4</sup>. LPA acts on specific G protein-coupled receptors eliciting responses ranging from chemotaxis and neurite remodelling to cell proliferation and survival<sup>5,6</sup>. The ATX-LPA signalling axis is implicated in vascular and neural development<sup>7-10</sup>, tumour progression and metastasis<sup>11-16</sup>, as well as inflammation<sup>17</sup>, fibrotic disease<sup>18,19</sup> and neuropathic pain<sup>20</sup>. As such, ATX holds promise as an attractive and easily accessible therapeutic target. We and others have recently described potent small-molecule inhibitors of ATX that are capable of lowering LPA levels in the circulation<sup>21,22</sup>.

ATX is a ~100 kDa glycoprotein that has several distinct domains (Fig. 1a). At the N-terminus it harbours two consecutive cysteine-rich somatomedin-B-like (SMB) domains, a fold known to be involved in protein-protein interactions<sup>23</sup>. The ATX SMB domains are attractive candidates for mediating the demonstrated binding of ATX to activated platelets and lymphocytes in an integrin-dependent manner<sup>17,24</sup>, thereby providing a possible route for localized LPA production and signalling at sites of injury and inflammation. The central catalytic phosphodiesterase (PDE) domain follows the SMB domains. It is similar to the catalytic domain of alkaline phosphatases, and its closest homologue with a known structure is a well-characterised bacterial phosphodiesterase<sup>1</sup>. Finally, at its C-terminus, ATX contains a nuclease-like (NUC) domain, which is catalytically inert and has been suggested to be involved in substrate binding and presentation<sup>25</sup>.

ATX/ENPP2 is one of seven mammalian ENPP type ectophosphodiesterases<sup>26</sup>, containing central PDE domains. Due to lack of structural data, the molecular basis for the diverse substrate preferences of ENPP family enzymes is not well understood. For example, the phosphodiesterase activity of the founding member ENPP1, a protein that has been implicated in the aetiology of mineralisation diseases and diabetes, is nucleotide-selective, whereas ATX/ENPP2 preferentially hydrolyzes lysophospholipids although it also accepts nucleotides as substrates.

The most potent small-molecule inhibitor we have recently described<sup>22</sup> contains a boronic acid, designed to specifically bind to the catalytic threonine of ATX. A structure-based mechanistic understanding of how boron binds to the threonyl nucleophile, and of the details of substrate recognition and catalysis by ATX will accelerate the further development of selective ATX inhibitors.

To understand how the domains of ATX are organized, their role in determining selectivity for lipid over nucleotide substrates, how our boronic acid inhibitors interact with ATX, and how the integrin-mediated interaction with platelets takes place, we determined the crystal structure of ATX/ENPP2; in this paper we present the structure of ATX from rat (*rATX*) and the structure-based biochemical analysis of human ATX (*hATX*).

## MATERIAL AND METHODS

### Protein production, crystallization and diffraction data collection

All protocols are described in references<sup>27,28</sup>. The HA155 inhibitor was mixed in three-molar excess with *rATX* and co-crystallized in conditions similar to the native data form<sup>27</sup>.



## Structure solution and refinement

Crystallographic statistics are shown in Table 1. Structure solution was performed using PHASER<sup>29</sup> in the hybrid molecular replacement - single anomalous dispersion mode. We used the structure of XaNP (2GSN<sup>1</sup>) as a search model, with non-conserved side chains truncated to the last common atom between residues. A clear rotation function solution was obtained (Z-score 15.01), sufficient to orient the single molecule of the asymmetric unit in the P1 space group. Using the phase probability distribution from that solution, PHASER identified ten heavy atom sites, using the anomalous differences from the zinc and iodine ions, resulting in phases with a figure of merit of 0.4. Solvent flattening followed by automated model building with ARP/wARP<sup>30</sup> resulted in 737 residues distributed in 8 chains. The model was completed manually using COOT<sup>31</sup>, interspersed with reciprocal space refinement cycles in REFMAC5<sup>32</sup>. The final model was validated using the MolProbity<sup>33</sup> server, and is of excellent quality without any Ramachandran outliers, ranking in the 93<sup>rd</sup> best percentile of PDB structures in that resolution. The second native crystal form, without Iodine in the crystallization conditions, was solved by

**Table 1:** Data collection and refinement statistics

	Native + I	Native 2	HA155 Inhibitor
<b>Data collection</b>			
Space group	P1	P2 <sub>1</sub> 2 <sub>1</sub> 1	P2 <sub>1</sub> 2 <sub>1</sub> 1
Cell dimensions			
<i>a</i> , <i>b</i> , <i>c</i> (Å)	53.8, 63.3, 70.5	95.3, 121.8, 158.4	63.99, 90.2, 152.7
$\alpha$ , $\beta$ , $\gamma$ (°)	98.8, 106.2, 99.8	90.0, 90.0, 90.0	90.0, 90.0, 90.0
Resolution (Å)	20.0-2.05 (2.12-2.05)	20.0-2.6 (2.74-2.6)	20.0-3.2 (3.36-3.2)
<i>R</i> <sub>merge</sub>	0.097 (0.378)	0.191 (0.488)	0.128 (0.571)
<i>I</i> / $\sigma$ ( <i>I</i> )	13.9 (2.5)	7.7 (1.5)	10.3 (3.5)
Completeness (%)	96.8 (93.9)	91.9 (69.7)	98.5 (98.5)
Redundancy	4.8(3.0)	3.1 (1.8)	6.0 (5.6)
<b>Refinement</b>			
Resolution (Å)	20.0-2.05	20.0-2.6	20.0-3.2
No. reflections	49561	49273	15034
<i>R</i> <sub>work</sub> / <i>R</i> <sub>free</sub>	17.2 / 22.0	21.6 / 27.5	20.1 / 25.5
No. atoms			
Protein	6396	12333	6140
Ligand/Ion/Glycan	5/3/39	-/6/56	34/3/39
Water/Iodine	332/28	19/-	11/6
<b>B-factors</b>			
Protein	38	29	53
Ligand/ion/Glycan	34/35/42	-/30/27	40/40/56
Water/Iodine	24/51	6/-	23/9
<b>R.m.s. deviations</b>			
Bond lengths (Å)	0.017	0.013	0.008
Bond angles (°)	1.62	1.52	0.93

\* For the 'Native + I' and 'HA155 Inhibitor' datasets a single crystal was used. For the 'Native 2' dataset two crystals were used.

molecular replacement and refined; apart from minor differences in disordered regions the two models are identical. The HA155 complex was determined by molecular replacement using the native ATX model without ions; the difference map showed clear density for the omitted zinc ions and the HA155 ligand. This structure was refined with autoBUSTER<sup>34</sup>. After adjusting protein regions, HA155 was modeled and refined using a dictionary generated by PRODRG<sup>35</sup> and manually adjusted to conform to the tetrahedral geometry expected for the reversibly covalent bound boron atom. Validation with Molprobrity shows 96.2% of all residues in Ramachandran favored regions, ranking in the 100<sup>th</sup> percentile for that resolution.

### Structure analysis

Structural similarity searches were performed with SSM<sup>36</sup> using default parameters. All interface calculations were performed with PISA<sup>37</sup>. The reported interface area is the difference in the accessible surface of isolated and interacting structures divided by two.

The HADDOCK web server was used<sup>38</sup> for docking a flexible LPC molecule into the structure of *r*ATX. The phosphate atom was restrained to a position consistent with the observed phosphate in the AMP:xaNPP complex. The binding pocket residues that were in contact with the HA155 inhibitor were treated as 'active' residues that make contacts with the LPC substrate. All other parameters were used with default values. Docking experiment resulted to a single cluster of 200 structures.

### Site directed mutagenesis

All constructs were made using standard molecular biology procedures and verified by sequencing.

### Protein production for EF-hand mutants

Cells were transiently transfected at 30-40% confluency using Fugene. The medium was collected 72 h later and the cells were lysed in 50 mM Tris/HCl, pH 7.5, 150 mM NaCl, 1% (w/v) Triton X-100 supplemented with 0.5 mM PMSF and 0.5 mM benzamide. After three freeze-thaw-cycles and ultracentrifugation (30 min at 100,000g) the supernatant was collected and used as 'cell lysate' in Western blots and to determine NPP2 activity.

### Protein production for binding site mutants

HEK293 cells were transiently transfected at 30-40% confluency using Fugene-6. The medium was collected 96 h later and used for pNP-TMP assays and LPC assays. Protein levels were quantified by Western blot.

### ATX/lysoPLD activity assay

ATX lysoPLD activity was measured by the release of choline from LPC<sup>22</sup>. Briefly, medium from transfected HEK293 cells containing approximately 5 nM *h*ATX (quantified by Western blot analysis using purified wild-type ATX as a standard), was incubated with 500  $\mu$ M LPC species in Tris-HCl buffer (pH 7.4), 0.01% (w/v) Triton X-100 for 4 h at 37 C. Liberated choline was detected colorimetrically using choline oxidase (1 Unit mL<sup>-1</sup>), horseradish peroxidase (2 Unit mL<sup>-1</sup>) and homovanillic acid (HVA) (2 mM). Fluorescence was determined at  $\lambda_{ex}/\lambda_{em} = 320/450$ nm in 96-well plates.

### Nucleotide phosphodiesterase assay

ATX nucleotide phosphodiesterase activity was measured colorimetrically using the nucleotide derivative pNP-TMP (p-nitrophenyl thymidine 5' -monophosphate) as a substrate<sup>39</sup>. 15 nM hATX of the preparations used also for the lysoPLD assay above, was incubated with 1 mM pNP-TMP in glycine-buffered saline at pH 9.5 in 96-well plates. The amount of liberated para-nitrophenolate (pNP) was determined by the absorbance at 405 nm for 3 h. For investigations of LPA inhibition, incubations contained 0.01% (w/v) Triton X-100 and varying concentrations of LPA (18:1).

### Protein production for platelet binding assays and LPA inhibition experiments

ATX proteins were generated by expression in CHO cells using variants of pSecTag engineered to fuse an IgK leader sequence and furin protease site N-terminal of a His6 sequence. Secreted proteins were purified from conditioned medium and concentrated to ~1 mg ml<sup>-1</sup> for use in binding assays.

### Static platelet adhesion assays

The interaction of ATX to activated platelets was studied by measuring binding of calcein labeled platelets to fibrinogen, ATX or fragments using a microtiter plate assay as described previously<sup>24</sup>. In brief, human platelets were isolated from citrate anticoagulated blood. Platelets were labeled by incubation with 7 mM calcein-AM and 150 nM PGI<sub>2</sub> and then isolated by gel filtration using Sepharose 2B eluted with Tyrodes buffer (12 mM NaHCO<sub>3</sub>, 138 mM NaCl, 5.5 mM glucose, 2.9 mM KCl, 10 mM HEPES, 0.35% (w/v) fatty-acid-free BSA, pH 7.35). ATX, ATX fragments or fibrinogen were diluted in 50 mM Tris pH 7.4 100 mM NaCl and incubated in a Microfluor 96-well plate for 16 h at 4° C. The wells were washed and blocked by incubation with Tyrodes buffer for 1 h at RT. Gel filtered platelets were diluted 200 times in Tyrodes buffer containing 2 mM CaCl<sub>2</sub>, 1 mM MgCl<sub>2</sub> and platelet activators, small molecule inhibitors or blocking antibodies. After incubation for 60 min at RT, wells were washed with Tyrodes buffer containing 2 mM CaCl<sub>2</sub>, 1 mM MgCl<sub>2</sub> and bound platelets were quantified by measurement of calcein fluorescence.

## RESULTS

### The crystal structure of Autotaxin

We determined the crystal structure of the full-length secreted form of rat ATX (*rATX*), which is 93% identical to the human enzyme *hATX* (Fig.1). A variant of *rATX*, in which two of the three glycosylation sites were mutated, leaving the single site needed for activity<sup>40</sup>, was produced in HEK293 cells, purified and crystallized<sup>27,28</sup>. The structure was determined to 2.0 Å resolution by a combination of molecular replacement and single-wavelength anomalous dispersion (Table 1).

*rATX* presents a compact and robust architecture for a multi-domain protein (Fig. 2a); two differently packed crystal forms show virtually identical domain placement (Fig. 2b,c). The two N-terminal cysteine-rich somatomedin-B-like (SMB) domains and the C-terminal nuclease-like (NUC) domain contact opposing sides of the catalytic phosphodiesterase (PDE) domain.

The structures of the individual domains of *rATX* (Fig. 2a) all resemble known folds (Fig. 3). The N-terminal SMB domains are structurally similar to both the SMB domain of vitronectin<sup>23</sup> and that of ENPPI (PDB:2YS0, unpublished) (Fig. 3a). The catalytic PDE domain is most similar to the *Xanthomonas axonopodis* nucleotide pyrophosphatase<sup>1</sup> (XaNPP) (Fig. 3b). The catalytic

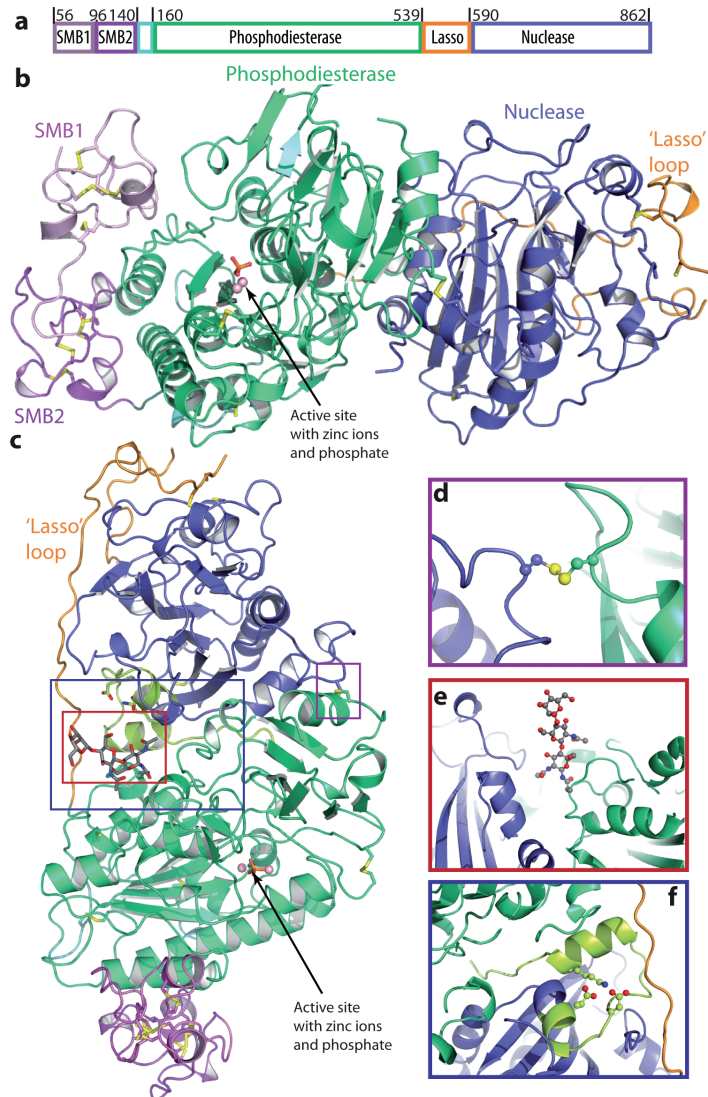


**Fig. 2: The structure of ATX.** (a) A schematic view of the domain structure of ATX; (b) Cartoon representation with the SMB domains coloured in pink and magenta, the PDE domain in green, the NUC domain in blue, the lasso loop wrapping around the NUC domain in orange (the lasso loop interacts with the rest of the proteins through 18 hydrogen bonds, 8 salt bridges, and a disulphide bond between residues 566 and 666) and the short loop connecting the SMB domains to the PDE domain in cyan; the phosphate and the zinc ions bound to the active site as well as cystine bridges are shown in stick-and-sphere representation, with the  $S_{\gamma}$  atoms in yellow, phosphorous in orange, zinc in pink; (c) The same cartoon as above in a different orientation, showing the active site with the bound phosphate and zinc ions and the lasso loop wrapping around the NUC domain to the left; the colored boxes relate to panels (d,e,f) showing the interface between the PDE and NUC domains; (d) The essential Cys-bridge that connects the PDE and NUC domains. (e) The essential glycan chain; (f) the C-terminal helix highlighted in lemon-green, with the important Lys-852 and its two salt-bridge partners, Glu-830 and Asp-836. All structural figures were created with Pymol (<http://www.pymol.org>).

residues of ATX and XaNPP, including the catalytic Thr209 and Thr90 respectively, are also well conserved (Fig. 3a). The closest structural match to the C-terminal NUC domain is the cyanobacterial nuclease NucA<sup>41</sup> (Fig. 3c), but none of the catalytic residues in NucA is conserved in the ATX NUC domain, accounting for its previously observed catalytic inactivity.

### The PDE-NUC domain interface

The PDE and NUC domains are tethered together in a strikingly rigid manner. The interface area is 1280 Å<sup>2</sup>, reinforced by seven hydrogen bonds and nine salt bridges. Many elements of the PDE domain participate in this interaction, while only the C-terminal region (802-859) of the NUC domain is involved. The two domains are tethered by an intermolecular Cys-bridge between residues 413 and 805 (Fig. 2d) that is essential for retaining catalytic activity<sup>25</sup>. Moreover, a large 'lasso' loop of 50 residues (540-589), starting at the end of the PDE domain, wraps tightly around the NUC domain (Fig. 2c), finally entering the fold from the side opposite to the PDE

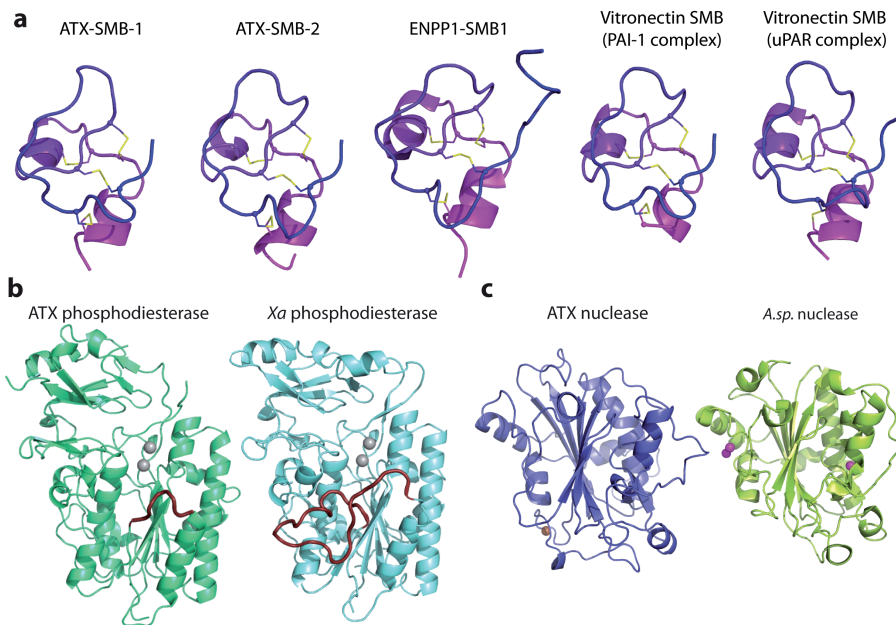


**Fig. 3: ATX domains and closest structural homologues.** (a) The two SMB domains of ATX/ENPP2, the ENPP1 SMB1 domain (PDB:2Y50, unpublished), and two structures of the vitronectin SMB domain (PDB:1OC0<sup>42</sup>, 3BT1<sup>43</sup>) are shown side by side, colored blue to magenta from N to C terminus with cystine bridges shown as sticks, with the S<sub>γ</sub> atom atoms in yellow. The ATX SMB domains share 38% sequence identity with the SMB domain of vitronectin, and 56% with that of ENPP1, displaying in both cases an rmsd of about 1.3 Å over 40 superposed C $\alpha$ s; (b) The ATX and XaNPP phosphodiesterase (PDB:2GSN<sup>1</sup>) domains shown in matched orientations; the short loop (residues 274-280) that is more extended in XaNPP (residues 154-178) is shown thicker and in ruby and the bound zinc ions are shown as grey spheres; the sequence identity between the two is 32%, with 1.5 Å rmsd over 335 superposed C $\alpha$ s; (c) Side by side comparison of the ATX nuclease domain with the *A.sp.* nuclease (PDB:1ZM8<sup>41</sup>); the sequence identity is 19%, with 2.1 Å rmsd over 335 superposed C $\alpha$ s. The EF-hand-like calcium (brown sphere) binding motif is at the bottom left and is absent in the bacterial nuclease; the *A.sp.* ion binding sites are indicated with magenta spheres and are absent in the ATX domain.

domain. Furthermore, the first two N-acetyl-glucosamine moieties of the essential Asn-524-linked glycan chain<sup>40</sup> are packed between the PDE and NUC domains (Fig. 2e), forming an interface area of 321 Å<sup>2</sup>. Finally, the C-terminal region from residues 829-850, which is essential for secretion<sup>25</sup>, as well as Lys852, which is required for catalytic activity<sup>25</sup>, are also in the domain interface (Fig. 2f). In the structure, Lys852 makes two salt bridges with Glu830 and Asp836 and is presumably important for positioning the C-terminal helix. It thus appears that evolution has selected for an extended range of interactions that bind the catalytically dead NUC domain to the active PDE domain.

The NUC domain of ATX (and ENPP1 and ENPP3) encompasses an EF-hand-like (EFL) motif<sup>26</sup> (<sup>739</sup>DYNYDGLRDETEDE<sup>751</sup>), crucial for activity for ENPP1 and ENPP3<sup>44</sup>, but reportedly not for ENPP2<sup>45</sup>. This 13-residue EFL motif binds Ca<sup>2+</sup> (Fig. 4a), but is not flanked by helices. Notably, its first residue, Asp739, bridges to Lys430 and is the only residue outside the C-terminus of the NUC domain that interacts with the PDE domain (Fig. 4b). ATX mutated at this site (K430A) was as active as the wild-type enzyme, but a significant amount was retained intracellularly (Fig. 4d). Furthermore, the secreted fraction of ATX (K430A) was more sensitive to thermal denaturation than wild-type ATX (Fig. 4e), suggesting that the salt bridge between Lys430 and Asp739 contributes to stabilization of the PDE-NUC interface. Mutation of three residues of the EFL motif (D739S/N741A/D743S) abolished secretion of ATX (Fig. 4d). The mutant proteins that accumulated intracellularly showed strongly reduced activity (Fig. 4e), consistent with previous findings for ENPP1 and ENPP3<sup>44</sup>.

### The phosphodiesterase catalytic site

The PDE domains of ATX and XaNPPI share similar architectures with fully conserved catalytic residues (Fig. 5a,b). At the active site, the Zn<sup>2+</sup> atom proximal to the catalytic Thr209 (Thr210 in *hATX*) is coordinated by the side chains of two aspartates and one histidine (Asp171, Asp358, His359), whereas the distal zinc is coordinated by one aspartate and two histidines (Asp311, His315, His474).

An asparagine residue (Asn230; Asn231 in *hATX*) faces the two metal ions in a position similar to that of Asn111 in XaNPPI. Asn111 was shown in XaNPPI not only to be important for catalysis but also to confer specificity for phosphodiester bond hydrolysis<sup>1</sup>; an arginine substitution at this position favoured phosphatase activity. In *hATX*, the N231A mutation significantly impairs the catalytic activity against both phospholipid and nucleotide substrates (Fig. 7a,b). Since ATX hydrolyzes ATP to generate AMP and pyrophosphate rather than ADP and phosphate, Asn230 is likely responsible for this preference for diester against monoester hydrolysis.

In one of the ATX crystal forms we located a phosphate ion (Fig. 3a and Fig. 6a) that matches the positions occupied in XaNPPI complex structures by the α-phosphate of AMP, or the transition state analogue vanadate (Fig. 5b). These similarities suggest a conserved catalytic mechanism, in which the activated Oγ nucleophile of Thr209 attacks the phosphate group of a substrate, resulting in the formation of a transition state involving a phosphate ester linkage<sup>1</sup>. The intermediate can then be hydrolyzed to the products, i.e. LPA or AMP.

### The substrate and inhibitor binding pocket

ATX hydrolyzes both nucleotide and phospholipid substrates, at least *in vitro*. The location of the nucleotide binding site in ATX can be inferred from the structure of XaNPPI bound to AMP (Fig. 5f). The shape of this site remains fully conserved in ATX (Fig. 5e). These two enzymes, and other ENPP family members, are therefore expected to bind nucleotides in a similar manner.

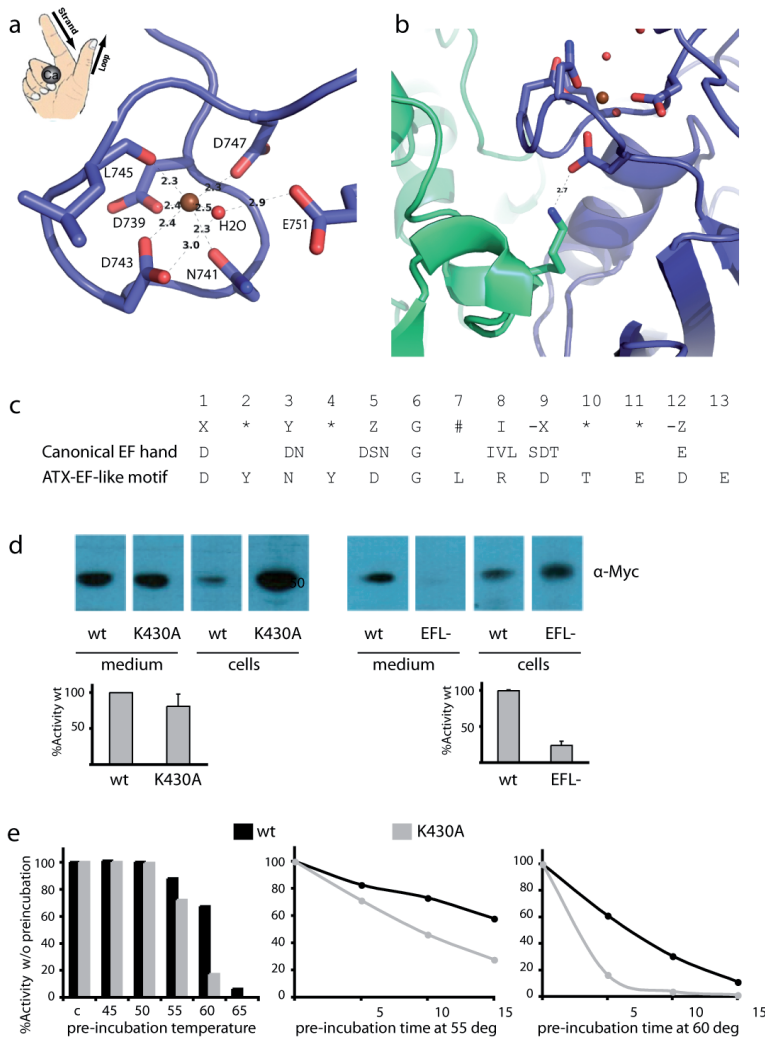


**Fig. 4: The EF-hand-like motif.** (a) The bound ion has structural and chemical characteristics consistent with  $\text{Ca}^{2+}$  (typical coordination sphere and absence of anomalous density); the coordinating residues are shown, together with the coordination distances. (b) The EF-hand-like motif contact with the phosphodiesterase domain is mediated by the salt bridge between Asp739 and Lys430. (c) The canonical EF-hand motif positions and most commonly identified residues, aligned to the ATX EF-hand-like motif. The residues in positions 1,3,5,9 (or X,Y,Z,-X; S.F.3C) are typical (Asp, Asn, Asp, Asp); and the position 7 ligand (-Y) is provided by the expected carbonyl of a hydrophobic Leu, uncommon for that position, but usually present at position 8, which in ATX is a very unusual Arg. The typical Gly is also conserved in position 6. However, the bidentate binder at position 12 (-Z, typically Asp or Glu), although an Asp in sequence, is not participating in ion binding; the -Z position ligand is instead provided by a water molecule fixed by the Glu residue in position 13 of this motif. (d) Expression of wtATX and K430A mutant and the triple EF-hand-like mutant in cell lysates and the culture medium (upper panels). Also shown is the specific lysophospholipase D activity, as compared to that of wtATX, of the secreted fraction for the K430A mutant and the intracellular fraction of the EF-hand-like mutant. (e) Activity of wtATX and K430A mutant after thermal denaturation at various temperatures, and as function of the pre-incubation time in various temperatures, indicating that the stability of the K430A mutant is compromised.

ATX-mediated LPC hydrolysis is specifically and potentially inhibited by a series of small-molecule boronic acid inhibitors that lower plasma LPA levels in mice following intravenous administration<sup>22</sup>. We determined a structure of *r*ATX in complex with one of these inhibitors, HA155<sup>46</sup> (Fig. 5c and Fig. 6b,c, Table 1), which enables us to correlate the activity of this inhibitor with its binding mode and make inferences about lipid substrate binding. The boron atom on one end of the inhibitor forms a reversible covalent bond with the nucleophile hydroxyl group of Thr209. One of the two boron hydroxyl groups is further stabilized between the two zinc ions. A search of the protein data bank did not yield any other structures in which a borate moiety is similarly complexed by two zinc ions and a threonyl nucleophile<sup>47</sup>. The rest of the hydrophobic four-ring system of HA155 forms an extended network of van der Waals contacts, with an interaction interface of 574 Å<sup>2</sup>. The first two aromatic rings of HA155 assume positions similar to those of the ribose and the adenine in the structure of XaNPP bound to AMP (Fig. 5c,e). The third, thiazolidinedione, ring would not be accommodated by the XaNPP structure (Fig. 5d). The last aromatic ring, a hydrophobic fluoro-benzene, is pointing directly into a deep hydrophobic pocket, oriented perpendicular to the protein surface.

We hypothesize that this hydrophobic pocket also binds the acyl chain of lysophospholipid substrates. We used High Ambiguity Driven DOCKing (HADDOCK<sup>38</sup>) to create a model of the binding of LPC(14:0) to our structure of *r*ATX. Fig. 5g and h show how the acyl chain can be easily accommodated in this pocket. The model also demonstrates that the pocket is large enough to accommodate only a single aliphatic chain, and explains how ATX sterically excludes di-acyl phospholipids. It is noteworthy that our model is consistent with previously reported biochemical data: for example, the change of Leu213 (Leu214 in *h*ATX), one of the hydrophobic residues lining the pocket and contacting the modeled substrate, to a polar histidine has been shown to decrease LPC hydrolysis<sup>48</sup>.

To validate our model further, we constructed additional binding site mutants and examined their activity. These mutagenesis studies employed *h*ATX (residue numbers in the human enzyme are n+1 compared to the rat enzyme above, owing to a single residue insertion after residue 37). *h*ATX and catalytically inactive *h*ATX T210A were used as controls to evaluate activity of the hydrophobic binding pocket mutants: F211A, Y307Q, L214H, F275Q, A305E, F274E, A218V, S170E (Fig. 7a). All mutants were expressed at levels similar to the wild-type enzyme. They were quantified and assayed in an LPC hydrolysis assay using saturating concentrations of LPC(14:0), the optimal substrate *in vitro* (Fig. 7c). All of these hydrophobic pocket mutants showed reduced lysoPLD activity levels when compared to wild-type *h*ATX (Fig. 7b).

The A218V mutant, which has about half the activity of *h*ATX, targets a residue deep in the hydrophobic pocket and alters LPC selectivity (Fig. 7a). This mutant hydrolyzes short-chain LPCs more efficiently than the wild-type protein (Fig. 7c). This can be explained by the presence of a bulkier valine residue at the bottom of the pocket, which possibly mediates a better contact with e.g. LPC(12:0), but excludes substrates with longer acyl chains. A218V and similar mutations that alter the acyl chain length selectivity could provide useful tools for probing the biological role and significance of ATX in generating distinct molecular species of LPA.

Many of the binding cleft variants differentially affect LPC and nucleotide hydrolysis. Although all of them are less active in the LPC hydrolysis assay, some can still hydrolyze nucleotide

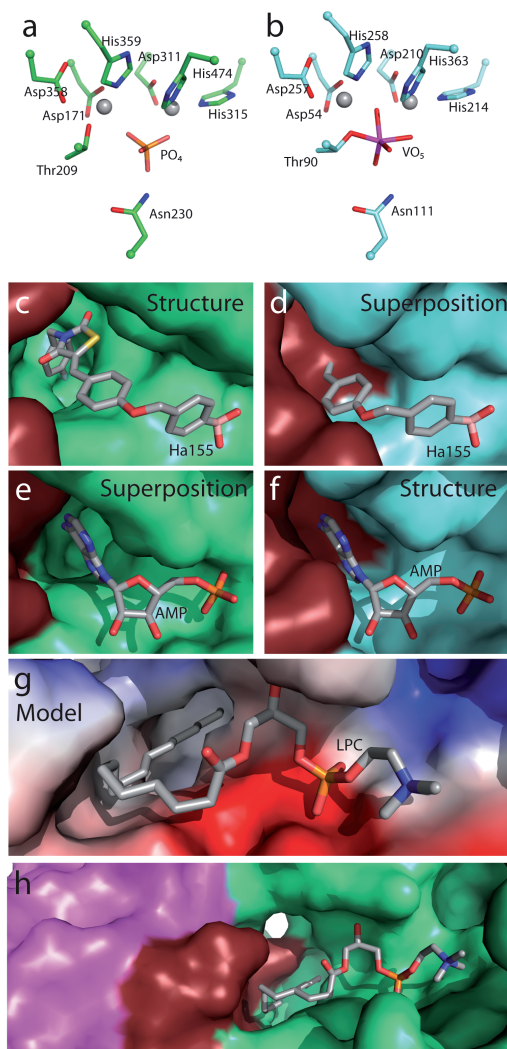


**Fig. 5: The ATX catalytic site and substrate binding pocket.** (a) The active site of ATX and (b) of XaNPP (PDB: 2GSO<sup>1</sup>). Side chain atoms are shown as sticks, with the C<sub>α</sub> atoms as spheres; all oxygen and nitrogen atoms are in red and blue respectively; Zn<sup>+2</sup> ions are grey spheres; phosphate atoms are coloured orange; and vanadium atoms magenta; (c) A surface representation of the ATX binding site with the HA155 inhibitor buried in the binding pocket and shown as sticks with carbon atoms colored grey and the covalently bound boron pink; the ATX surface is green with the short loop that is more extended in XaNPP and ENPPI (residues 274-280) colored ruby; (d) The surface of XaNPP coloured in aquamarine, superposed on the ATX complex with HA155; the extended XaNPP- and ENPPI-specific loop (residues 154-178) in ruby, highlighting the absence of the hydrophobic pocket in XaNPP; (e) The ATX substrate binding site shown as in (c) but with AMP superposed from the XaNPP complex structure; (f) The XaNPP surface with bound AMP (PDB: 2GSU<sup>1</sup>) shown as sticks; (g) The ATX surface colored by electrostatic potential (-70 to 70 kT) to highlight the hydrophobic nature of the binding pocket, is shown together with a stick model of a docked LPC molecule; (h) A view similar to (g) colored as in (c),(e) and with the second SMB domain in magenta, highlighting the close interaction of the SMB domain with the lipid binding groove. The narrow tunnel is visible as a white hole in the middle.

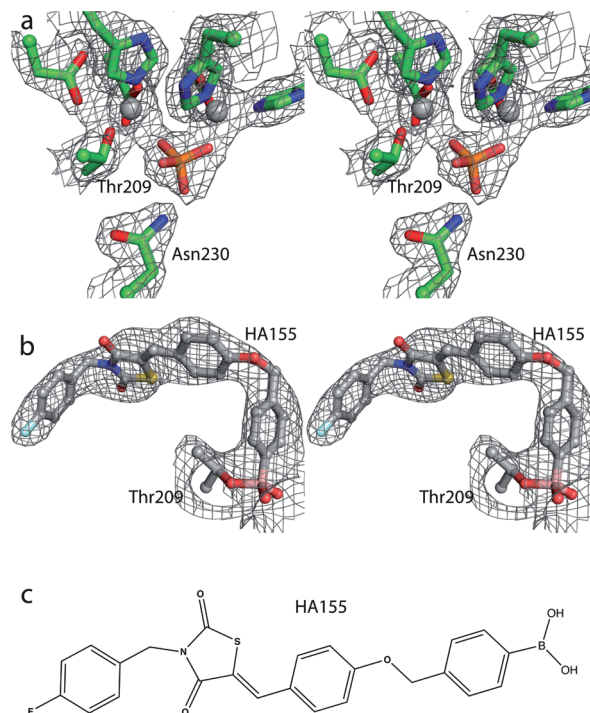


**Fig. 6: Electron density maps for bound PO4 for HA155 and chemical structure of HA155.** (a) Stereo pair of the 2mFo-DFc Fourier synthesis contoured at 1.2 rms of the 2.1 Å map, showing the density for the active site residue, the Zn ions and the bound PO4. (b) Stereo pair of the bias-removed composite omit map at 3.2 Å, showing the bound ligand and the covalent linkage to Thr209. (c) Chemical structure of the HA155 inhibitor.

substrates with near wild-type activity. These include the previously reported L214H mutant and the novel mutants S170E, A218V and A305E (Fig. 7b), which target the acyl chain lipid binding region of the pocket. In contrast, the Y307Q or F211Y mutants, which target the region of the binding site that accommodates both nucleotides and lipids, are significantly less active against both lipid and nucleotide substrates. In fact, these two variants are comparatively less active against nucleotides than lipids, possibly because these mutations have a greater effect on the bulkier nucleoside moiety than the glycerol group of the lipid substrates. These observations suggest that the hydrophobic binding pocket is an extension of the nucleotide binding site that specifically accommodate lysophospholipid acyl chains, without affecting nucleotide binding.

When the structures of ATX and XaNPP are superimposed, a stretch of 18 amino acids in XaNPP occupies the space corresponding to the hydrophobic binding pocket of ATX. This stretch of amino acids in XaNPP thus precludes it from accommodating lysophospholipids (Fig. 3b). Sequence alignments indicate that while ATX has a deletion in this region, XaNPP and ENPP1 do not (Fig. 1). The presence of this stretch of amino acids in ENPP1 and XaNPP therefore explains why they cannot hydrolyze lysophospholipids, and why ENPP1 is insensitive to ATX inhibitors such as HA155<sup>22</sup>.

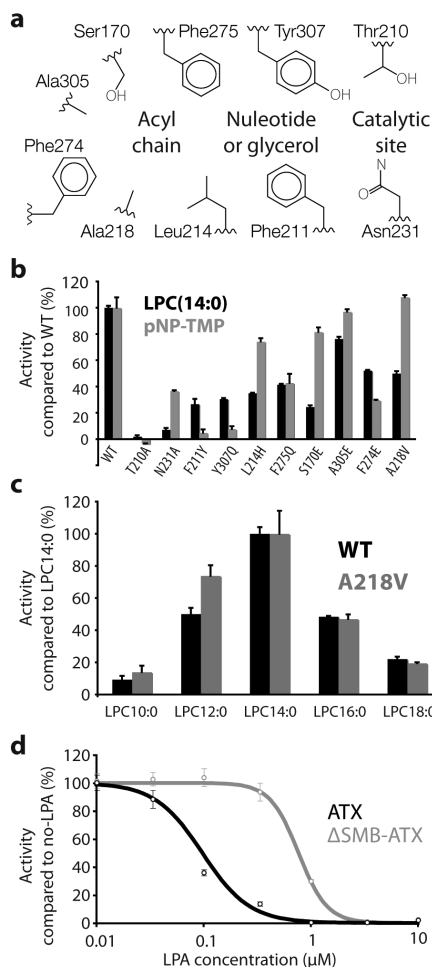


**Fig. 7: Biochemical analysis of human ATX and mutants.** (a) A simplified drawing of the ATX binding pocket. The residues used for mutagenesis studies are indicated; (b) Modulation of LPC and pNP-TMP hydrolysis activity by ATX mutants, indicating the importance of specific residues for selectivity in LPC and nucleotide hydrolysis; (c) The A218V mutants prefers shorter chain lengths; the activity for WT *h*ATX and A218V mutant was normalized to 100% for LPC(14:0); (d) LPA(18:1) inhibition of nucleotide hydrolysis for wild-type ATX and ΔSMB-ATX. All error bars represent the s.e.m.

### The SMB domains and interaction with integrins

The two N-terminal Cys-rich SMB domains in ATX (atxSMB1 and atxSMB2) provide the first structural instances of these domains in the context of an intact protein. The structure of the SMB domain of the plasma protein vitronectin (vSMB) is known, both alone and in complex with the plasminogen activator inhibitor-1<sup>42</sup> (PAI-1, Fig. 10a) and the urokinase-type plasminogen activator<sup>43</sup> (uPAR) (Fig. 10b). The structural organization of the SMB domain cysteine knot fold, comprising four pairs of crossed disulfide bonds, had been the subject of considerable debate<sup>23,49</sup>.

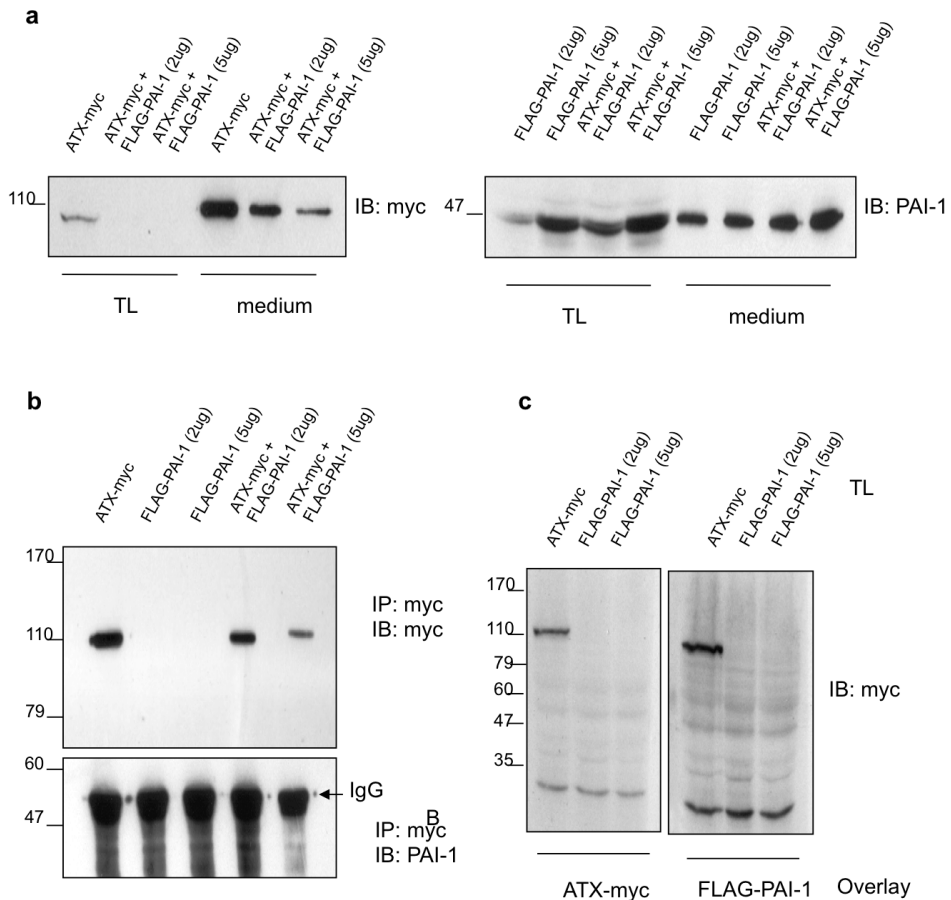


**Fig. 8: ATX does not bind to PAI-1.** (a) Expression of ATX-myc and FLAG-tagged PAI-1 in HEK 293 cell lysates and in the medium. (b) Immunoprecipitation of ATX-myc from HEK293 cell lysates expressing ATX-myc and/or FLAG-PAI-1, as indicated. IPs were immunoblotted for Myc or PAI-1. (c) Total lysates from cells expressing ATX-myc or FLAG-PAI-1 were separated by SDS-page and blotted onto a nitrocellulose membrane. The membranes were exposed either to medium containing secreted ATX-myc (secreted FLAG-PAI-1 was used as a negative control). Binding of ATX-myc to the membrane was assessed by immunoblotting using anti-myc antibody.

The organization of the atxSMB domains is consistent with the vitronectin SMB X-ray and NMR structures, as well as with the NMR structure of the ENPPI SMB domain (PDB:2YSO, unpublished).

Both atxSMB domains form extensive interactions with the catalytic PDE domain (Fig. 10c,d). The interaction between the atxSMB1 domain and the PDE domain involves approximately the same surface that mediates the vSMB to PAI-1 and uPAR interactions. However, atxSMB2 uses an unusual interface for interaction with the PDE domain, leaving the surface more typically used for protein-protein interactions available to engage with other binding partners (Fig. 10d). We examined whether hATX can interact with PAI-1 by co-expression and immuno-precipitation experiments, but detected no interaction (Fig. 7).

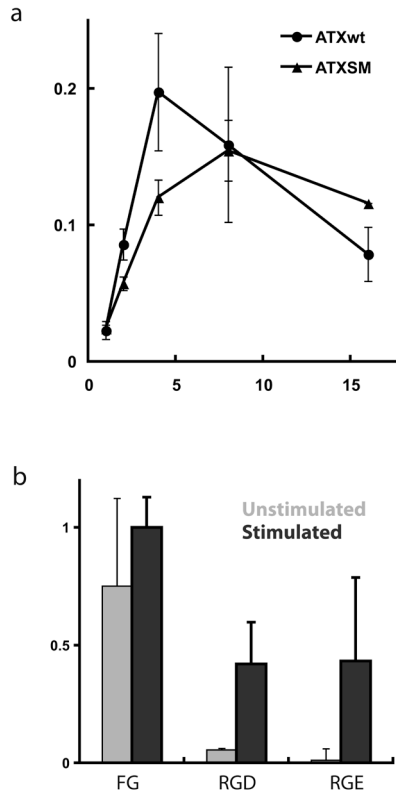


**Fig. 9: wtATX and SMB-ATX domains binding to integrins is concentration dependent.** (a) Binding of platelets to varying concentrations of immobilized ATX or ATX SMB domain was determined as described in the methods. The data are normalized to binding observed with 10mg/ml fibrinogen and are means  $\pm$  SD of triplicate determinations. (b) Binding of platelets to fibrinogen, hATX and hATX RGD→RGE mutant. The data are normalized to binding observed with 10mg/ml fibrinogen and are means  $\pm$  SD of triplicate determinations. Error bars represent the s.e.m.

ATX binds to activated platelets in a  $\beta_3$  integrin-dependent manner and mediates static adhesion of platelets to immobilized ATX<sup>24</sup>. By analogy with the well characterized vSMB-mediated interactions with integrins, we considered the possibility that the ATX SMB domains also interact with platelet integrins. We found that a truncated protein containing only the two ATX SMB domains (53-143, atxSMB) strongly binds to activated human platelets (Fig. 10f,g). Binding to the SMB domains is enhanced by stimulating the platelets with ADP or the integrin activator  $Mn^{2+}$  and is substantially attenuated by the  $\beta_3$  integrin blocking antibody 7E3 (Fig. 10f). Moreover, binding of the isolated SMB domains to platelets is comparable to that of full-length ATX, in both avidity and concentration dependence (Fig. 9a). From these results we conclude that the N-terminal SMB domains are the primary mediators of the ATX-platelet interaction with  $\beta_3$  integrins on the agonist-stimulated platelet surface. The atxSMB2 domain contains an integrin-binding sequence RGD motif (126-128, Fig. 10d,e). However, this motif lies within the atxSMB2

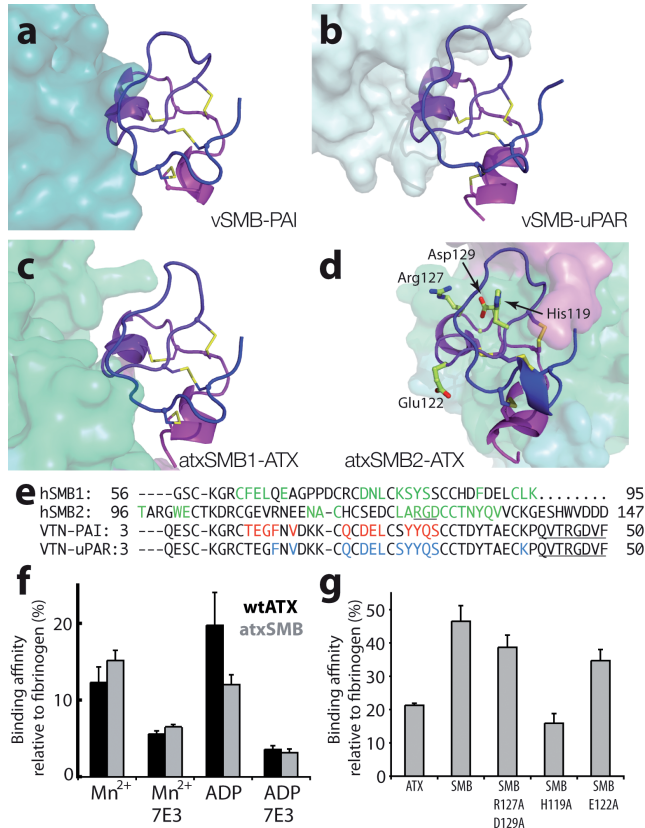


**Fig. 10: The SMB domains and integrin-mediated interaction with activated platelets.** (a) The structure of the vitronectin SMB domain (vSMB) with plasminogen activator inhibitor 1 (PAI-1, PDB:1OOC<sup>42</sup>). The SMB domain is shown as a cartoon, colored from purple through blue from the N- to the C-terminus, and the Cys-bridges are shown as yellow sticks. PAI-1 is shown as a surface colored aquamarine. The vSMB interaction surface with PAI-1 is 656 Å<sup>2</sup>, making five hydrogen bonds and five salt bridges; (b) vSMB in complex with the urokinase-type plasminogen activator receptor (uPAR complex, PDB:3BT1<sup>43</sup>) in light cyan. The vSMB interaction surface with uPAR is 620 Å<sup>2</sup>, making seven hydrogen bonds and five salt bridges; (c) The first SMB domain of ATX (atxSMB1) highlighting the interaction with the rest of ATX, shown as a surface colored as in Fig.1. The atxSMB1 interaction surface with the PDE is 620 Å<sup>2</sup>, making nine hydrogen bonds and a salt bridge; (d) The second SMB domain (atxSMB2) with the rest of ATX. The atxSMB2 interaction surface with the PDE is 571 Å<sup>2</sup>, but forming only three hydrogen bonds; (e) An alignment of vitronectin and ATX SMB sequences; residues involved in interaction with binding partners are in color; the RGD motifs are underlined; (f) Binding of wild-type ATX and atxSMB to activated platelets is similar in magnitude, depends on Mn<sup>2+</sup> and ADP, and can be lowered by interference with an integrin β3 binding antibody. (g) Binding of the atxSMB domains to platelets is significantly attenuated by mutation of His-119 to alanine and less affected by mutation of the RDB motif. All error bars represent the s.e.m.

domain, whereas the vitronectin RGD motif is located several residues downstream from its SMB domain and is disordered<sup>42</sup>. In vitronectin, an RGD to RGE mutation disrupts an Asp-mediated Mn<sup>2+</sup> interaction between the ligand and integrin thereby severely attenuating integrin binding. An ATX RGE mutant, however, shows binding to activated platelets indistinguishable from that

of wild-type ATX (Fig. 9b). Binding of platelets to the isolated SMB domains containing an AGA mutant (R127A/D129A) showed less binding compared to the wild-type SMB domain protein (Fig. 10g and Fig. 11), but did not abolish it as expected. This suggested that the interaction of ATX with platelet  $\beta 3$  integrins is mechanistically distinct from the binding of the vitronectin SMB domain to these receptors, and involves residues separate from the RGD motif. To examine this notion further, we created five additional mutants of the atxSMB2 domain: E110A, R112A, H119A, D121A and E122A. Of these, only H119A and E122A were expressed in amounts sufficient for purification and further experiments. While E122A abrogated binding to an extent similar to that of the AGA mutant, the H119A mutation showed significantly reduced binding. Glu122 is conserved in the vSMB, while His119 is a Gln (maintaining the nitrogen donor at a similar position), and both these residues participate in the interaction of vSMB with PAI-1 and uPAR. These experiments confirm that binding of ATX to integrins involves a wider portion of the available atxSMB2 surface, which includes His119, Asp122 as well as Asp129.

### The SMB domains are involved in LPA binding

AtxSMB2 abuts the lipid-binding pocket and a nearby narrow tunnel (the ‘white hole’ in Fig. 5h). In both crystal forms residual electron density occupies this tunnel (Fig. 12), likely indicating the presence of a molecule that we were unable to model, possibly a lipid acquired from the growth medium.

The proximity of the SMB domains to the lipid-binding site and the tunnel raises the possibility that they might be involved in product binding and release. To test if the SMB domains modulate the enzymatic activity of ATX, we expressed an ATX variant lacking both SMB1 and SMB2 ( $\Delta$ SMB-ATX; residues 145-863 of *h*ATX). We have previously reported that LPA acts as a mixed-type inhibitor of ATX activity against a variety of substrates<sup>39</sup>. We could thus probe the role played by the SMB domains in product binding and release by comparing LPA-mediated inhibition of nucleotide hydrolysis in wild-type ATX and  $\Delta$ SMB-ATX. Both wild-type ATX and the  $\Delta$ SMB-ATX protein exhibited comparable activity against the classical nucleotide substrate pNP-TMP, with  $k_M$  values of  $1.93 \pm 0.20$  and  $2.87 \pm 0.9$  mM respectively (Fig. 13). However, whereas wild-type ATX activity against this substrate was potently inhibited by LPA (18:1)

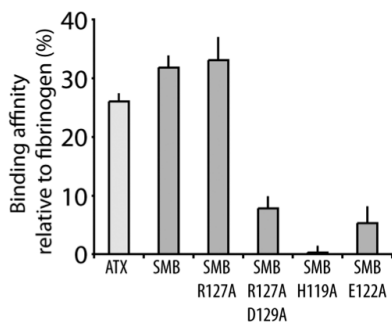


**Fig. 11: Binding of atxSMB domains and mutants to platelets.** In this alternative platelet preparation, binding of the atxSMB domains to platelets is attenuated by mutation of the RGD motif, but is totally abolished by mutation of His-119 to alanine. All error bars represent the s.e.m..

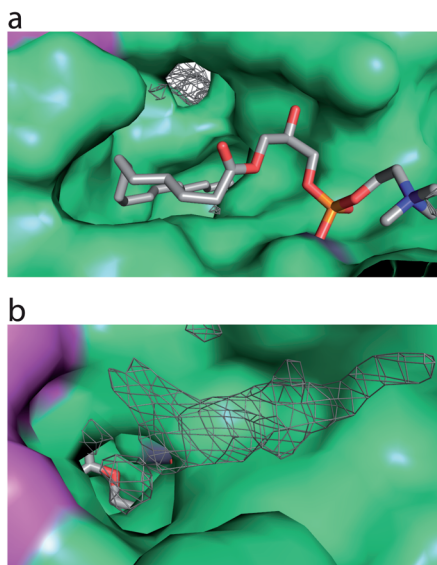


**Fig. 12: Residual electron density near the tunnel in the structure of native ATX.** (a) The view and coloring and settings are as in Figure 3. The difference electron density maps with coefficients  $mF_o - DF_c, \Phi_{calc}$  is shown as a grey grid contoured at 3.5 *rms*. (b) The same as in a, looking from the back - the density indicating a bound ligand is now visible through the tunnel but the additional electron density is more clear.

( $EC_{50}$  0.08  $\mu M$ ),  $\Delta$ SMB-ATX was approximately 10-fold less sensitive ( $EC_{50}$  0.72  $\mu M$ ) to inhibition by this LPA species (Fig. 7d). These results identify a role for the SMB domains as a determinant of the affinity of the interaction between ATX and LPA, and are consistent with our suggestion that SMB2 participates in substrate recognition and/or product release. Processes that impact on the interaction between SMB2 and the PDE domain, for example integrin binding, could constitute a mechanism for physiological regulation of ATX activity.

## DISCUSSION

We have determined the crystal structure of rat ATX and tested the activities of structurally guided site- directed mutants in human ATX. Since the enzymes from the two species are 93% identical, the biochemical and structural experiments readily complement one another.

A deep, hydrophobic pocket of the type observed in ATX is a thermodynamically unstable structure. We suggest that the formation of strong interactions between the NUC and PDE domains during the course of evolution, may have stabilized the fold sufficiently for it to accommodate the deletion of eighteen residues (Fig. 1) and the consequent formation of the hydrophobic pocket.

The determinants of the substrate specificity of the ENPPs have long been a mystery. The ATX structure provides a possible explanation. Both nucleotides and lipids partially share the same binding pocket, but the acyl-chain of lipid substrates form additional hydrophobic contacts with ATX. This model implies that the LPA product likely has higher affinity for ATX than

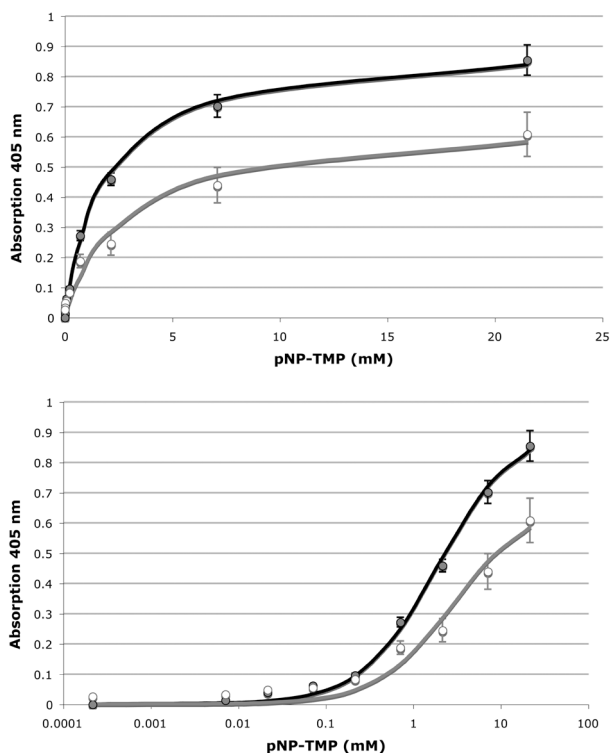


**Fig. 13: Activity of wild-type ATX and  $\Delta$ SMB-ATX in pNP-TMP hydrolysis.** Observed hydrolysis rates for varying substrate concentrations presented in black for wild-type ATX and grey for  $\Delta$ SMB-ATX. The same data are shown in a linear (**top**) and logarithmic (**bottom**) x-axis for clarity. Error bars represent the s.e.m.

any nucleotide substrate. This hypothesis is consistent with our previous finding that LPA acts as an inhibitor of ATX activity against a variety of substrates<sup>39</sup>, but not of LPC hydrolysis<sup>46</sup>. Thus, LPA formed by the enzyme may act as a “substrate specifying factor” that effectively inhibits the hydrolysis of nucleotides because it can only be displaced by lysophospholipid substrates such as LPC. This mechanism could dictate ATX activity *in vivo*, because the spectrum of available LPA species could define ATX activity against specific lysophospholipid substrates. Our findings also suggest that further analysis of structural determinants of substrate discrimination could lead to the identification of molecules that inhibit the hydrolysis of specific substrates, e.g. long-chain rather than short-chain LPC species.

The ATX SMB domains function as protein interaction modules, mediating platelet interaction through integrin binding. However, the binding mode appears to be structurally distinct from classical RGD-mediated integrin binding. Instead, ATX-SMB2 may interact with integrins using a surface similar to that employed by the related vitronectin SMB domains in their interactions with PAI-1 and uPAR.

We also have shown that the SMB domains are important for binding the LPA product to ATX, and we speculate that they might be involved in LPA release. In this scenario, SMB-

mediated interactions with integrins might not only provide a mechanism for recruiting ATX to the cell surface to generate LPA in proximity of its receptors, but could also mediate a conformational change to promote product release. Localized LPA production by integrin-mediated recruitment of ATX (e.g. at the platelet surface) may account for the observed increase in plasma LPA levels following platelet activation<sup>50</sup>. Similar reasoning may also be applied to ENPP1, where a natural mutation of lysine 173 (K173Q, often described in literature as 'K121Q'), that is equivalent to the Arg128 of the ATX RGD motif, has severe physiological consequences<sup>51</sup> suggesting that modulation of integrin binding to the SMB domains through such mutations may result in altered ENPP1/2 activities *in vivo*.

Further structural and biochemical studies examining ATX with its physiological substrates, products and specific integrin subunits, will be necessary to unravel how exactly LPA production is regulated by ATX.

**Accession codes.** The models and structure factors for *r*ATX and *r*ATX+HA155 respectively are deposited in the PDB with accession codes 2xr9 and 2xrg respectively.

## ACKNOWLEDGEMENTS

Crystallographic experiments were performed at the PX beamline at the Swiss Light Source, Paul Scherrer Institut, Villigen, Switzerland; at the European Synchrotron Radiation Facility beamline ID23-2; at the Diamond Light Source ID19 microfocus beamline; and the GM/CA-CAT, NE-CAT, and LS-CAT beamlines at the Advanced Photon Source. We thank all beamline scientists and especially Sean McSweeney, David Flo, Klemens Schultze-Briese, Takashi Tomizaki, Gwyndaf Evans and Jonathan Grimes for data collection assistance. E.C. and A.P. thank Valeria De Marco, Dene Littler and Prakash Rucktooa for assistance with crystal mounting and data collection. J.H. and A.P. thank Tom Walter, Patrick Celie, Mariano Sturnaiolo and Tatjana Heidebrecht for advice and assistance, the NKI and Pfizer for jointly providing a pre-doctoral fellowship to J.H., Titia Sixma for feedback on the manuscript, and the NKI Protein Facility for infrastructure access.

## REFERENCES

1. Zalatan, J.G., Fenn, T.D., Brunger, A.T. & Herschlag, D. Structural and functional comparisons of nucleotide pyrophosphatase/phosphodiesterase and alkaline phosphatase: implications for mechanism and evolution. *Biochemistry* **45**, 9788-803 (2006).
2. Stracke, M.L. et al. Identification, purification, and partial sequence analysis of autotaxin, a novel motility-stimulating protein. *J Biol Chem* **267**, 2524-9 (1992).
3. Tokumura, A. et al. Identification of human plasmalysophospholipase D, a lysophosphatidic acid-producing enzyme, as autotaxin, a multifunctional phosphodiesterase. *J Biol Chem* **277**, 39436-42 (2002).
4. Umezu-Goto, M. et al. Autotaxin has lysophospholipase D activity leading to tumor cell growth and motility by lysophosphatidic acid production. *J Cell Biol* **158**, 227-33 (2002).
5. Noguchi, K., Herr, D., Mutoh, T. & Chun, J. Lysophosphatidic acid (LPA) and its receptors. *Curr Opin Pharmacol* **9**, 15-23 (2009).
6. van Meeteren, L.A. & Moolenaar, W.H. Regulation and biological activities of the autotaxin-LPA axis. *Prog Lipid Res* **46**, 145-60 (2007).
7. van Meeteren, L.A. et al. Autotaxin, a secreted lysophospholipase D, is essential for blood vessel formation during development. *Mol Cell Biol* **26**, 5015-22 (2006).
8. Tanaka, M. et al. Autotaxin stabilizes blood vessels and is required for embryonic vasculature by producing lysophosphatidic acid. *J Biol Chem* **281**, 25822-30 (2006).
9. Koike, S. et al. Autotaxin/lysophospholipase D-mediated lysophosphatidic acid signaling is required to form distinctive large lysosomes in the visceral endoderm cells of the mouse yolk sac. *J Biol Chem* **284**, 33561-70 (2009).
10. Fotopoulou, S. et al. ATX expression and LPA signalling are vital for the development of the nervous system. *Dev Biol* **339**, 451-64.
11. Lin, S. et al. The absence of LPA2 attenuates tumor formation in an experimental model of colitis-associated cancer. *Gastroenterology* **136**, 1711-20 (2009).
12. Liu, S. et al. Expression of autotaxin and lysophosphatidic acid receptors increases mammary tumorigenesis, invasion, and metastases. *Cancer Cell* **15**, 539-50 (2009).
13. Mills, G.B. & Moolenaar, W.H. The emerging role of lysophosphatidic acid in cancer. *Nat Rev Cancer* **3**, 582-91 (2003).
14. Nam, S.W. et al. Autotaxin (ATX), a potent tumor motogen, augments invasive and metastatic potential of ras-transformed cells. *Oncogene* **19**, 241-7 (2000).
15. Taghavi, P. et al. In vitro genetic screen identifies a cooperative role for LPA signaling and c-Myc in cell transformation. *Oncogene* **27**, 6806-16 (2008).
16. David, M. et al. Cancer cell expression of autotaxin controls bone metastasis formation in mouse through lysophosphatidic acid-dependent activation of osteoclasts. *PLoS One* **5**, e9741.
17. Kanda, H. et al. Autotaxin, an ectoenzyme that produces lysophosphatidic acid, promotes the entry of lymphocytes into secondary lymphoid organs. *Nat Immunol* **9**, 415-23 (2008).
18. Pradere, J.P. et al. LPA1 receptor activation promotes renal interstitial fibrosis. *J Am Soc Nephrol* **18**, 3110-8 (2007).
19. Tager, A.M. et al. The lysophosphatidic acid receptor LPA1 links pulmonary fibrosis to lung injury by mediating fibroblast recruitment and vascular leak. *Nat Med* **14**, 45-54 (2008).
20. Inoue, M. et al. Initiation of neuropathic pain requires lysophosphatidic acid receptor signaling. *Nat Med* **10**, 712-8 (2004).
21. Gierse, J.K. et al. A Novel Autotaxin Inhibitor Reduces Lysophosphatidic Acid Levels in Plasma and the Site of Inflammation. *J Pharmacol Exp Ther* (2010).
22. Albers, H.M. et al. Boronic acid-based inhibitor of autotaxin reveals rapid turnover of LPA in the circulation. *Proc Natl Acad Sci U S A*.
23. Zhou, A. Functional structure of the somatomedin B domain of vitronectin. *Protein Sci* **16**, 1502-8 (2007).
24. Pamuklar, Z. et al. Autotaxin/lysophospholipase D and lysophosphatidic acid regulate murine hemostasis and thrombosis. *J Biol Chem* **284**, 7385-94 (2009).
25. Jansen, S., Andries, M., Derua, R., Waelkens, E. & Bollen, M. Domain interplay mediated by an essential disulfide linkage is critical for the activity and secretion of the metastasis-promoting enzyme autotaxin. *J Biol Chem* **284**, 14296-302 (2009).

26. Stefan, C., Jansen, S. & Bollen, M. NPP-type ectophosphodiesterases: unity in diversity. *Trends Biochem Sci* **30**, 542-50 (2005).
27. Day, J.E. et al. Crystallization and preliminary X-ray diffraction analysis of rat autotaxin. *Acta Crystallographica Section F* **66**, 1127-1129 (2010).
28. Hausmann, J. et al. Mammalian cell expression, purification, crystallization and microcrystal data collection of autotaxin/ENPP2, a secreted mammalian glycoprotein. *Acta Crystallographica Section F* **66**, 1130-1135 (2010).
29. McCoy, A.J. Solving structures of protein complexes by molecular replacement with Phaser. *Acta Crystallogr D Biol Crystallogr* **63**, 32-41 (2007).
30. Langer, G., Cohen, S.X., Lamzin, V.S. & Perrakis, A. Automated macromolecular model building for X-ray crystallography using ARP/wARP version 7. *Nat Protoc* **3**, 1171-9 (2008).
31. Emsley, P. & Cowtan, K. Coot: model-building tools for molecular graphics. *Acta Crystallogr D Biol Crystallogr* **60**, 2126-32 (2004).
32. Murshudov, G.N., Vagin, A.A. & Dodson, E.J. Refinement of macromolecular structures by the maximum-likelihood method. *Acta Crystallogr D Biol Crystallogr* **53**, 240-255 (1997).
33. Davis, I.W. et al. MolProbity: all-atom contacts and structure validation for proteins and nucleic acids. *Nucleic Acids Res* **35**, W375-83 (2007).
34. Blanc, E. et al. Refinement of severely incomplete structures with maximum likelihood in BUSTER-TNT. *Acta Crystallogr D Biol Crystallogr* **60**, 2210-21 (2004).
35. Schuttelkopf, A.W. & van Aalten, D.M. PRODRG: a tool for high-throughput crystallography of protein-ligand complexes. *Acta Crystallogr D Biol Crystallogr* **60**, 1355-63 (2004).
36. Krissinel, E. & Henrick, K. Secondary-structure matching (SSM), a new tool for fast protein structure alignment in three dimensions. *Acta Crystallogr D Biol Crystallogr* **60**, 2256-68 (2004).
37. Krissinel, E. & Henrick, K. Inference of macromolecular assemblies from crystalline state. *J Mol Biol* **372**, 774-97 (2007).
38. de Vries, S.J., van Dijk, M. & Bonvin, A.M. The HADDOCK web server for data-driven biomolecular docking. *Nat Protoc* **5**, 883-97 (2010).
39. van Meeteren, L.A. et al. Inhibition of autotaxin by lysophosphatidic acid and sphingosine 1-phosphate. *J Biol Chem* **280**, 21155-61 (2005).
40. Jansen, S. et al. An essential oligomannosidic glycan chain in the catalytic domain of autotaxin, a secreted lysophospholipase-D. *J Biol Chem* **282**, 11084-91 (2007).
41. Ghosh, M., Meiss, G., Pingoud, A., London, R.E. & Pedersen, L.C. Structural insights into the mechanism of nuclease A, a betabeta alpha metal nuclease from *Anabaena*. *J Biol Chem* **280**, 27990-7 (2005).
42. Zhou, A., Huntington, J.A., Pannu, N.S., Carrell, R.W. & Read, R.J. How vitronectin binds PAI-1 to modulate fibrinolysis and cell migration. *Nat Struct Biol* **10**, 541-4 (2003).
43. Huai, Q. et al. Crystal structures of two human vitronectin, urokinase and urokinase receptor complexes. *Nat Struct Mol Biol* **15**, 422-3 (2008).
44. Bollen, M., Gijsbers, R., Ceulemans, H., Stalmans, W. & Stefan, C. Nucleotide pyrophosphatases/phosphodiesterases on the move. *Crit Rev Biochem Mol Biol* **35**, 393-432 (2000).
45. Lee, J. et al. Enzymatic activation of autotaxin by divalent cations without EF-hand loop region involvement. *Biochem Pharmacol* **62**, 219-24 (2001).
46. Albers, H.M. et al. Boronic acid-based inhibitor of autotaxin reveals rapid turnover of LPA in the circulation. *Proc Natl Acad Sci U S A* **107**, 7257-62 (2010).
47. Golovin, A. & Henrick, K. MSDmotif: exploring protein sites and motifs. *BMC Bioinformatics* **9**, 312 (2008).
48. Cimpean, A., Stefan, C., Gijsbers, R., Stalmans, W. & Bollen, M. Substrate-specifying determinants of the nucleotide pyrophosphatases/phosphodiesterases NPPI and NPP2. *Biochem J* **381**, 71-7 (2004).
49. Li, X., Zou, G., Yuan, W. & Lu, W. Defining the native disulfide topology in the somatomedin B domain of human vitronectin. *J Biol Chem* **282**, 5318-26 (2007).
50. Eichholtz, T., Jalink, K., Fahrenfort, I. & Moolenaar, W.H. The bioactive phospholipid lysophosphatidic acid is released from activated platelets. *Biochem J* **291** ( Pt 3), 677-80 (1993).
51. Prudente, S., Morini, E. & Trischitta, V. Insulin signaling regulating genes: effect on T2DM and cardiovascular risk. *Nat Rev Endocrinol* **5**, 682-93 (2009).







STRUCTURAL SNAPSHOTS  
OF AUTOTAXIN/ENPP2 AND THEIR  
IMPLICATIONS FOR CATALYSIS

To be submitted to *Journal of Molecular Biology*

## ABSTRACT

Autotaxin (ATX) is a secreted ecto-nucleotide pyrophosphatase / phosphodiesterase with lysophospholipase D activity, producing the signalling lipid lysophosphatidic acid (LPA) from lysophosphatidylcholine (LPC). The bimetallic active site of ATX is structurally similar to other members of the alkaline phosphatase superfamily. Here, we examine two new crystal structures of ATX, namely ATX-VO<sub>5</sub>, a complex of ATX with orthovanadate, and ATX-pThr, where the active site nucleophile Thr209 of ATX is phosphorylated. We postulate that both structures mimic reaction steps of the substrate hydrolysis by ATX. In the ATX-VO<sub>5</sub> structure the vanadate anion adopts a trigonal bipyramidal conformation and is covalently bound to the O<sub>γ</sub> nucleophile of Thr209, mimicking the transition state of the enzymatic reaction after the nucleophilic attack onto the substrate. The phosphorylated Thr209 structure likely represents the reaction intermediate prior to the second nucleophilic attack of an activated water molecule to form the product. These two structures, together with our previous structure of ATX complexed to a phosphate ion, offer three catalytic snapshots. In these structures we observe a movement of Thr209 and of the position of the zinc ions relative to each other and to the rest of the active site, and the water molecule that likely fulfils the second nucleophilic attack. Our data support the concept of an associative two-step in-line displacement mechanism for ATX.

---

Jens Hausmann, Leonie van Zeijl, Wouter H. Moolenaar & Anastassis Perrakis

---

## INTRODUCTION

Autotaxin (ATX) is a secreted 100 kDa glycoprotein<sup>1</sup>. It is a unique member of the ectonucleotide pyrophosphatase / phosphodiesterase (ENPP) family<sup>2</sup> as it is the only family member that has also lysoPLD activity and hydrolyses lysophosphatidylcholine (LPC) into lysophosphatidic acid (LPA)<sup>3, 4</sup>. LPA is a signalling lipid that activates many cellular pathways by binding to specific G-protein coupled receptors (LPA<sub>1-6</sub>) (Fig. 1)<sup>5</sup>. The ATX-LPA signalling axis is implicated in vascular and neural development, tumour progression and metastasis, inflammation, fibrotic disease and neuropathic pain<sup>6, 7</sup>. Others and we have recently crystallized and determined the structure of ATX<sup>8, 9</sup>, which shows a compact and robust architecture for a multi-domain protein; it consists of four domains, two N-terminal somatomedin-B-like domains, the catalytic phosphodiesterase domain (PDE) and an inert nuclease domain (NUC). The crystal structures of ATX showed that the architecture of the active site around the Threonine 209 (Thr209) nucleophile, including the two zinc ions (Zn<sub>1</sub> and Zn<sub>2</sub>) and their coordination shell, are similar to the closest structural homologue of ATX, the nucleotide pyrophosphatase from *Xanthomonas axonopodis* (XaNPP PDB: 2GSO)<sup>10</sup>. The hydrophilic substrate binding groove is a further conserved structural feature of both enzymes. In analogy to XaNPP structure<sup>10</sup>, this groove should accommodate the ribose and base moieties of nucleotide substrates, and in ATX accommodates the glycerol backbone of the lipid substrates<sup>9</sup>. This shallow groove in ATX extends into a deep hydrophobic pocket, which is not present in XaNPP, and results from a deletion of an 18 amino acid stretch that is specific to ATX within the ENPP family. It has been shown, that this hydrophobic pocket binds the alkyl chain of lipid substrates<sup>9</sup>, as well as the hydrophobic fluoro-benzene ring of HA155<sup>8</sup>, a nanomolar inhibitor of ATX<sup>11</sup>. In addition, the crystal structures also revealed a unique tunnel, which starts from the shallow hydrophilic groove exiting on the opposing side of the PDE domain. This tunnel is putatively involved in LPA binding, and has also been suggested by Nishimasu *et al.* to potentially present the LPA product to its cognate receptor<sup>9</sup>.

The superfamily of alkaline phosphatases groups a diverse set of metalloenzymes<sup>12</sup>, including for example XaNPP<sup>10</sup>, the name-giving member of this superfamily the alkaline phosphatase (AP) of *E.coli*<sup>13</sup>, but also ATX<sup>14</sup>. The AP preferentially hydrolyses phosphomonoesters<sup>15</sup>, while XaNPP preferentially hydrolyses phosphodiester<sup>10, 14</sup>, like ATX<sup>2</sup>. Phosphate monoester and diester hydrolysis are considered to follow a two-step in-line displacement mechanism, in a dissociative fashion for phosphomonoesterases and in an associative fashion for phosphodiesterases<sup>16, 17</sup>. During the dissociative reaction mechanism (D<sub>N</sub> + A<sub>N</sub> mechanism) the cleavage of the phosphorus leaving group bond precedes the formation of the new phosphorus-nucleophile bond. In contrast, in the associative mechanism (A<sub>N</sub> + D<sub>N</sub> mechanism) no significant bond cleavage to the leaving group occurs while the new bond to the nucleophile is established<sup>18, 19</sup>.

Here, we present two new crystal structures of ATX complexes. The first complex is with the transition state mimic orthovanadate and in the second complex the Thr209 nucleophile is phosphorylated. We postulate that both structures mimic reaction steps during the catalysis of ATX, and based on that information, we propose an associative two-step in-line displacement mechanism for the substrate catalysis by ATX.

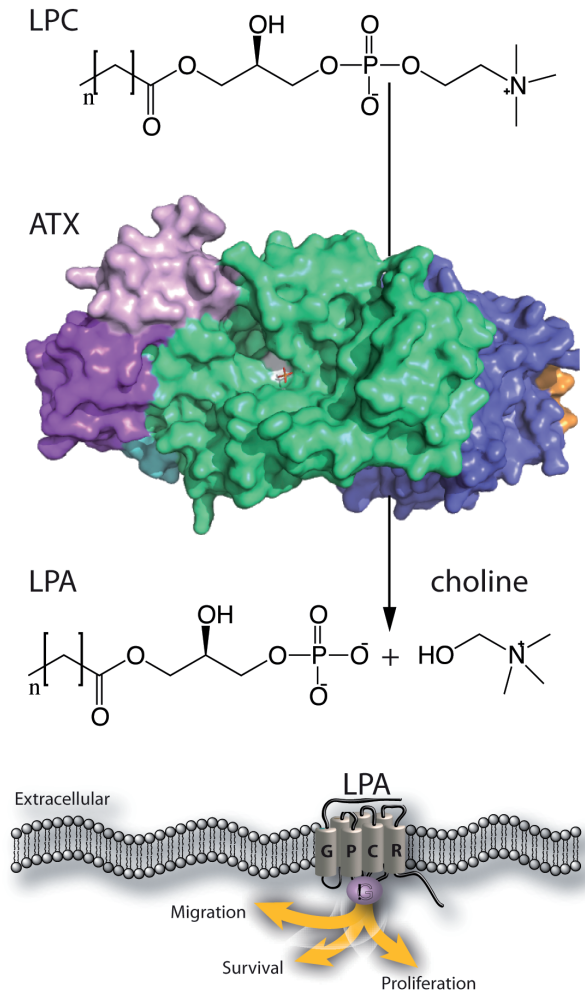


**Fig. 1: Schematic presentation of ATX-LPA axis.** ATX cleaves the choline headgroup from various LPC molecules to produce LPA. LPA can then bind to its cognated G-protein coupled receptors ( $LPA_{1-6}$ ) to transduce the signal and triggers cellular responses.

## MATERIAL AND METHODS

### Expression and Purification of rATX for crystallization

Recombinant His-tagged ATX was expressed and purified from HEK293 medium using POROS-20 MC columns pre-loaded with  $Cu^{2+}$  as previously published<sup>20</sup>. Briefly, the column was washed with eight to ten column volumes of buffer A (20 mM HEPES pH 7.4, 150 mM NaCl). ATX was eluted with a linear gradient of buffer B (20 mM HEPES pH 7.4, 150 mM NaCl and 500 mM imidazole). Subsequently the recombinant protein was further purified using a Superose 6 (10/300) gel filtration column. The rATX protein was concentrated to 4.5 mg/ml using a Amicon

Ultra 0.5 ml 10 kDa concentrator. The recombinant protein concentration was determined using Nanodrop1000. The purity of ATX (<95%) was monitored on a SDS-PAGE.

### Expression and Purification of rATX for vanadate inhibition assays

His-tagged rat ATX (isoform 2) from a stable Flp-In cell line was expressed in roller bottles and purified from medium using Talon affinity resin (Clontech) (1 ml slurry per 50 ml of medium). Purified protein was eluted from the beads in 150 mM NaCl/50 mM Hepes/500 mM Imidazole. Subsequently, Imidazole was removed by dialysis (150 mM NaCl, 50 mM Hepes).

### ATX/lysoPLD activity assay

ATX lysoPLD activity was measured by the release of choline from LPC 18:1. Briefly, 30 nM ATX (863 aa) was incubated with 150  $\mu$ M LPC 18:1 in Tris-HCl buffer (pH 7.4), 0.01% (w/v) Triton X-100 at 37 C. Liberated choline was detected colorimetrically using choline oxidase (1 Unit mL<sup>-1</sup>), horseradish peroxidase (2 Unit mL<sup>-1</sup>) and homovanillic acid (HVA) (2 mM). Fluorescence was determined at  $\lambda_{ex}/\lambda_{em}$ =320/450nm in 96-well plates. Measurements were taken every 90 seconds for 90 minutes. For inhibition investigations varying concentrations of Na<sub>3</sub>VO<sub>4</sub> were used. The maximum velocity of each sample was determined by data analysis using prism graph pad software.

### Nucleotide phosphodiesterase assay

ATX nucleotide phosphodiesterase activity was measured colorimetrically using the nucleotide derivative pNP-TMP (p-nitrophenyl thymidine 5'-monophosphate) as a substrate. 30 nM ATX (recombinant protein like above) was incubated with 1 mM pNP-TMP in Trizma buffered saline at pH 7.8 in 96-well plates. The amount of liberated para-nitrophenolate (pNP) was determined by the absorbance at 405 nm for 1.5 h. For investigations of Na<sub>3</sub>VO<sub>4</sub> inhibition, incubations contained varying concentrations of Na<sub>3</sub>VO<sub>4</sub>. The maximum velocity of each sample was determined by data analysis using prism graph pad software

### Crystallization of ATX-VO<sub>5</sub>

Crystallization experiment was performed at 293 K using the hanging-drop variant of the vapour-diffusion method in Limbro plates as previously published.<sup>21</sup> The reservoir solution (1ml) consisted of 18% (w/v) PEG 3350, 0.2 M NH<sub>4</sub>I and 0.4 M NaSCN. The drop was made by mixing 1  $\mu$ l of rATX (4.5 mg/ml) pre-incubated with 1 mM orthovanadate and 1  $\mu$ l of reservoir solution on siliconized cover slips (pH: 7.4). Typically after two weeks the first crystals appeared, but had to grow for another two weeks to obtain a crystal of 0.05 x 0.05 x 0.02 mm<sup>3</sup>. Crystals were vitrified in reservoir solution with the addition of 20% glycerol and 3.6 mM orthovanadate.

### Crystallization of ATX-pThr

This crystallization experiment was performed in the same setting as above. The reservoir solution contained 20% (w/v) PEG 3350, 0.1 M NH<sub>4</sub>I and 0.3 M NaSCN. The drop was made by mixing 1  $\mu$ l of rATX (4.5 mg/ml) pre-incubated with 2mg/ml heparin sulfate and 1  $\mu$ l of reservoir solution (pH: 6.3). After one week the first crystals formed, but they had to grow for a couple of more days, to obtain a crystal of 0.15 x 0.02 x 0.02 mm<sup>3</sup>. Crystals were vitrified in cryoprotectant, which consisted of reservoir solution with the addition of 20% (v/v) glycerol and a final concentration of 2 mg/ml heparin sulfate.

**Data Collection, Structure Determination, Refinement and Deposition of ATX-VO<sub>5</sub>**

X-ray diffraction data were collected on X06DA (PXIII) at the SLS at 100° K. The crystallographic diffraction data were recorded on a PILATUS detector to a resolution of 2.2 Å. The space group was determined as P1 with cell dimension of a=53.8 Å, b=63.5 Å, c=70.6 Å and  $\alpha=99.3^\circ$ ,  $\beta=105.9^\circ$ ,  $\gamma=99.5^\circ$ . The data were processed with iMOSFLM<sup>22</sup> and scaled with SCALA<sup>23</sup>. The ATX-pThr structure was taken as a model for the ATX-VO<sub>5</sub> structure. These initial coordinates were chosen because both structures are in the same space group (P1) and have almost identical unit cell dimensions. The structure was solved using Molecular Replacement using PHASER<sup>24</sup>. All ligands and waters were removed from the model apart from Zn<sub>1</sub>, Zn<sub>2</sub> and the Ca site. Manual model building and subsequent refinement were performed iteratively with COOT<sup>25</sup> and REFMAC5<sup>26</sup>. PDB-Redo<sup>27</sup> was finally used and the  $R_{\text{factor}}/R_{\text{free}}$  converged to 0.224/0.259 (Table1). The quality of this final structure model was validated with the MolProbidity<sup>28</sup> server and ranks in the 99<sup>th</sup> best percentile of PDB structures in this resolution with no Ramachandran outliers. Atomic coordinates and experimental structure factors of ATX-VO<sub>5</sub> have been deposited in PDB database under the code XXXX. All presentations of structures within this work were made using PyMol.

**Data Collection, Structure Determination, Refinement and Deposition of ATX-pThr**

X-ray diffraction data were collected on ID29 at the ESRF 100° K. The crystallographic diffraction data were recorded on a PILATUS detector to a resolution of 1.65 Å. The apparent crystal space group was P1 with cell dimension of a=53.7 Å, b=63.5 Å, c=70.7 Å and  $\alpha=98.7^\circ$ ,  $\beta=105.8^\circ$ ,  $\gamma=100.0^\circ$ . All data were processed and integrated with XDS<sup>29</sup> and scaled with SCALA<sup>23</sup>. The structure was determined by molecular replacement using PHASER<sup>24</sup> with four ensemble searches for the PDE-, NUC-, SMB1 and SMB2 domain. Manual model building and subsequent refinement was performed iteratively with COOT and REFMAC5<sup>30</sup>. Finally PDB-REDO was used and the  $R_{\text{factor}}/R_{\text{free}}$  converged to 0.184 and 0.216 (Table 1). The quality of the structure was validated with MolProbidity and ranks in the 91<sup>th</sup> best percentile of PDB structures in this resolution with no Ramachandran outliers. Atomic coordinates and experimental structure factors of ATX-pThr have been deposited in PDB under the code XXXX.

NOTE: The ATX-pThr structure was obtained in a co-crystallization approach with unfractionated heparin. We detect well-defined sugar-like electron density in the tunnel of the ATX-pThr structure. However, since an undefined mixture of heparin sulphate was used and these sugar chains can be very divers, it was not possible to model it unambiguously. Noteworthy, a similar density within the tunnel at a comparable location is recognizable in ATX-VO<sub>5</sub> structure, which was not incubated with any other ligand than orthovanadate, as well as in the native ATX-PO<sub>4</sub> structure. The occurrence of this ligand electron density must therefore be a co-purified product of the recombinant expression of ATX. To model this electron density and to validate, whether this is an artifact or of physiological relevance, is beyond scope of this paper, but surely interesting to pursue.

**RESULTS & DISCUSSION****Vanadate inhibition data of pNP-TMP and LPC hydrolysis**

The vanadate anion closely mimics phosphate, structurally and chemically, and the concept of vanadate as a phosphoryl transfer transition state mimic has become widely accepted<sup>31,32</sup>. Orthovanadate (VO<sub>4</sub><sup>3-</sup>) is a well-known micromolar inhibitor for protein tyrosine phosphatases and alkaline phosphatases.

To test if this transition metal oxoanion also inhibits the catalytic phosphodiesterase activity of ATX, we performed a vanadate inhibition analysis of ATX using lysophosphatidylcholine (LPC 18:1) and the nucleotide phosphodiester analogue pNP-TMP as substrates. Our data (Fig. 2) show that, as expected, vanadate is a weak inhibitor of both the LPC and pNP-TMP hydrolysis, with  $K_i$ -values of  $160 \pm 50 \mu\text{M}$  and  $35.0 \pm 8 \mu\text{M}$  respectively. These  $K_i$  values are comparable to reported values in the literature for the closely related XaNPP protein<sup>10</sup>. The inhibitor dissociation constants of vanadate in both assays are in a similar range, supporting the notion that orthovanadate functions as a transition state mimic for ATX. From that data we concluded that structural complex data of ATX with orthovanadate as a transition state mimic would be helpful to characterize the catalytic mechanism in more detail.

### Crystal Structure of ATX with orthovanadate (ATX-VO<sub>5</sub>)

We obtained a 2.2 Å complex structure of ATX with orthovanadate (ATX-VO<sub>5</sub>) and refined it to an  $R_{\text{free}}$  of 0.259. The characteristic trigonal bipyramidal shape of the penta-covalent vanadium, which is linked covalently to the enzyme via the O $\gamma$  of Thr209, could be observed in the electron density maps (Fig. 3b). The O $\gamma$  atom of Thr209 occupies one of the two axial oxygen positions in that configuration. The opposing axial oxygen is 2.6 Å away from the Zn<sub>1</sub>, similar to the vanadylated AP structure, where this free axial oxygen is 2.4 Å from the Zn<sub>1</sub> site<sup>33</sup> (PDB: 1B8J). The three equatorial oxygens and the vanadium are aligned in a plane. The first equatorial vanadate oxygen is coordinated between the two zinc ions, with 1.9 Å to the Zn<sub>1</sub> and 2.5 Å to the Zn<sub>2</sub> site. The second equatorial oxygen forms hydrogen bonds to the amide nitrogens of the backbone of Thr209 and of the side chain of Asn230 (Fig. 4b).

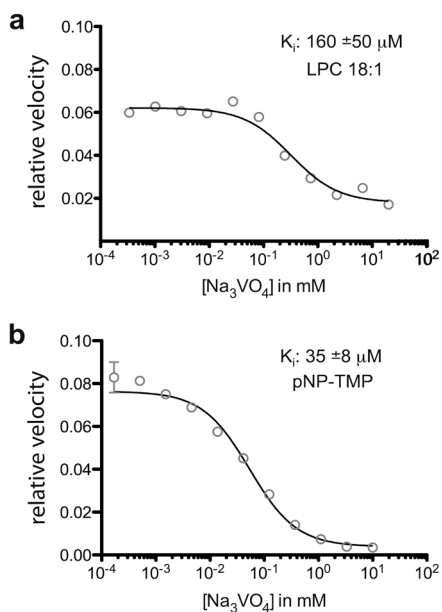


**Fig. 2:** Michaelis-Menten vanadate inhibition analysis of (a) LPC (18:1) and (b) pNP-TMP hydrolysis catalyzed by ATX.

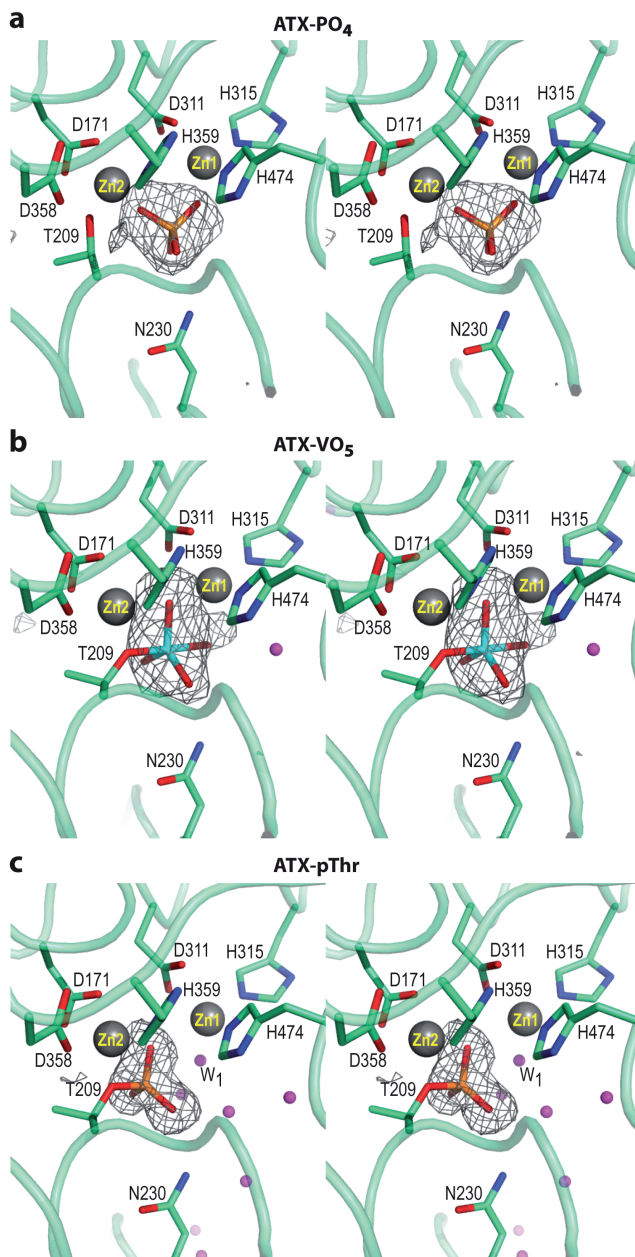


**Fig. 3:** Stereo images showing close-up views of the active site of ATX. The structure of ATX is shown as transparent ribbon presentation in light green. Active site residues and ligands are depicted as sticks with oxygens in red, nitrogens in blue, phosphorous in yellow and vanadium in cyan (a) In the ATX-PO<sub>4</sub> the  $F_o - F_c$  electron density omit map contoured at  $3.5\sigma$  with the modeled phosphate from the PDB 2XR9. (b) The  $F_o - F_c$  electron density map presented as grey mesh at  $3.5\sigma$  in the ATX-VO<sub>5</sub> structure before modeling the vanadate into the structure. (c) The  $F_o - F_c$  electron density map obtained from the ATX-pThr structure, before modeling the phosphorylated Thr209, depicted at  $3.5\sigma$  as grey mesh.

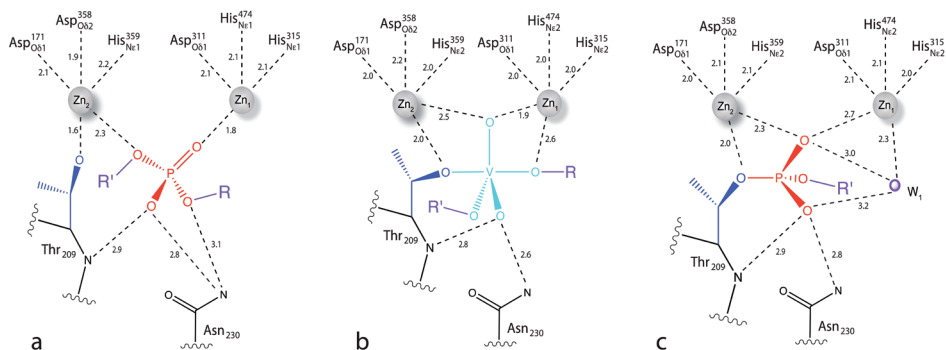


**Fig. 4:** Schematic presentation of the active site from (a) the ATX- $\text{PO}_4$ , (b) the ATX- $\text{VO}_5$  and (c) the ATX-pThr structure. The active site side chain of Thr209 is colored in dark blue and its backbone in black, the bound phosphate and the covalently bound phosphate are shown in red, and the vanadate ion is presented in light blue. Hypothesized R and R'-groups are added in purple. Atomic interactions are depicted as dashed lines.

**Table 1:** Data collection and refinement statistics of ATX- $\text{VO}_5$  and ATX-pThr structure

	ATX- $\text{VO}_5$	ATX-pThr
Data collection		
Space group	P1	P1
Cell dimensions		
a, b, c (Å)	53.8, 63.5, 70.6	53.7, 63.5, 70.7
$\alpha$ , $\beta$ , $\gamma$ (°)	99.4, 105.9, 99.5	98.7, 105.8, 100.0
Resolution (Å) <sup>a</sup>	40-2.20 (2.32-2.20)	44-1.65 (1.74-1.65)
$R_{\text{merge}}$ <sup>a</sup>	0.116 (0.825)	0.059 (0.619)
$I / \sigma(I)$	4.9 (1.4)	7.9 (1.2)
Completeness (%) <sup>a</sup>	90.2 (90.7)	92.5 (91.6)
Redundancy <sup>a</sup>	1.6 (1.7)	2.0 (2.0)
Refinement		
Resolution (Å)	40-2.20	44-1.65
No. Reflections	63704	188720
$R_{\text{work}} / R_{\text{free}}$ (%)	22.4/25.9	18.4/21.6
No. atoms		
Protein	6281	6384
Ligand/Ion/Glycan	35	39
Water	138	469
B-factors		
Protein	37.7	28.2
Ligand/Ion/Glycan	29.4	29.0
Water	32.5	30.5
R.m.s. deviations		
Bond lengths (Å)	0.016	0.019
Bond angles (°)	1.92	1.66

<sup>a</sup>Data in parentheses correspond to the highest resolution shell.

The third equatorial oxygen does not appear to make any specific bonds with the protein. The geometry of orthovanadate mimicking transition states, is represented with great variety in the PDB database<sup>32</sup>. Generally it can be divided into distorted or non-distorted trigonal bipyramidal geometry. The vanadate anion was observed to be distorted with an angle between the axial oxygens of 157° for XaNPP (PDB: 2GSO) and of 172° for AP<sup>10; 33</sup> (PDB: 1B8J). Since our vanadate complex data are only of medium resolution (2.2 Å) and the vanadate geometry was restrained it is hard to conclude about the nature of these bonds; however, no clear evidence of distortion was evident in the electron density maps.

### Crystal Structure of ATX with a phosphorylated Thr209 (ATX-pThr)

We obtained a 1.65 Å complex structure of ATX (ATX-pThr) and refined it to an  $R_{free}$  of 0.216. Here, we observed additional electron density extending from the O<sub>γ</sub> of Thr209 into the active site, but in a tetrahedral shape, which suggests the presence of a phosphorylated Thr209 (Fig 3c). This complex has been crystallized in more acidic conditions (pH: 6.3) compared to previous crystallization conditions (pH: 7.4); at that pH the hydrolysis of the phosphorylated active site becomes rate-limiting at acid pH and allowed trapping of this intermediate in our structure<sup>34; 35</sup>.

We were able to identify only two structures of phosphorylated active site nucleophiles from the AP superfamily exist in the PDB. However, both structures are made with mutant versions of the AP phosphomonoesterase. In the first structure the Zn<sub>1</sub> coordinating histidine (His331) was mutated to glutamine (PDB: 1HJK) and in the second one the serine nucleophile (Ser102) was substituted for a threonine<sup>36; 37</sup> (PDB: 2GA3). Thus this structure is the first to show a phosphorylated active site intermediate for a phosphodiesterase member of the AP superfamily.

In this structure we observe a water network in the active site. The core of this network consists of five water molecules, which interact with the protein via hydrogen bonds to Asp473, Asn230 and Lys208. The most intriguing water molecule of this network is the W<sub>1</sub> molecule, which is 2.2 Å from the Zn<sub>1</sub> (Fig 3c). This water is suitably oriented to fulfil a water-based nucleophilic attack on the phosphorous atom of the phosphorylated Thr209, as it is expected for the second step of the catalytic sequence of phosphodiesterases.

### Comparison of ATX-PO<sub>4</sub>, ATX-VO<sub>5</sub> and ATX-pThr structures

The ATX-VO<sub>5</sub> and ATX-pThr structures constitute two snapshots of the catalysis by ATX. In our first structure of ATX (PDB: 2XR9, ATX-PO<sub>4</sub> therein), we have observed a phosphate ion close to Thr209 (Fig 3a and Fig 4a). The ATX-PO<sub>4</sub> structure provides a third snapshot that mimics the substrate bound state, the first step in the reaction sequence of ATX. Collectively, ATX-PO<sub>4</sub>, ATX-VO<sub>5</sub> and the ATX-pThr structures mimic consecutive reaction steps during the catalysis by ATX and allow a more detailed description of the two-step catalytic mechanism that has been put forward<sup>14</sup>.

A comparison of the ATX-PO<sub>4</sub>, ATX-VO<sub>5</sub> and ATX-pThr protein structures show they are overall nearly identical with RMSD of 0.39 Å over 771 aligned C<sub>α</sub> atoms (calculated by the RAPIDO server)<sup>38</sup> and demonstrate no significant conformational domain changes of ATX during catalysis. However, the three structures have a wealth of local changes that allows to follow the catalytic mechanism in more detail.

In the ATX-PO<sub>4</sub> structure, the zinc ions are 4.3 Å from each other and each is bound to the phosphate oxygen that represent the attachment positions of the R and R' groups of the

substrate, while Zn<sub>2</sub> is activating the O<sub>γ</sub> of the threonine nucleophile that is 1.6 Å from it. The third oxygen, presumably the one that has a partial negative charge in the alkaline pH that the reaction takes place, is bound to the amine group of Asn230, that is characteristic of the phosphodiester but not the monoester cleaving enzymes<sup>39</sup>. The fourth oxygen, the one bearing to the double bond to the phosphate, is not constrained by any interactions.

In the next step, likely represented by the ATX-VO<sub>5</sub> structure, one equatorial oxygen atom of the vanadate, representing the free oxygen in the real substrate, is inserted between the two zinc ions almost in the same line as the one connecting the two zinc ions that are still 4.3 Å from each other. This oxygen is now significantly closer to the Zn<sub>1</sub> (1.9 Å) rather than the Zn<sub>2</sub> (2.7 Å). The axial oxygen where the R leaving group of the substrate would normally lie, is now far from the Zn<sub>1</sub> and would thus allow the first product to depart. As the R group leaves we move to the next step that is represented by the ATX-pThr structure. Here, the two zinc ions are further apart, 4.5 Å from each other. The phosphate oxygen now moves away from the line connecting the two zincs, and it is significantly further away from Zn<sub>1</sub> (2.7 Å) than in the previous step (1.9 Å). In proximity to the Zn<sub>1</sub> is in that structure the water molecule (W1, 2.2 Å) that likely comes into place to fulfil the second nucleophilic displacement event and facilitate the departure of the R' leaving group.

The most prominent change in these catalytic snapshots is however the movement of the active site side chain of Thr209. The χ<sub>1</sub> of Thr209 in the ATX-PO<sub>4</sub> structure is -87°, while the χ<sub>1</sub> of Thr209 in the ATX-VO<sub>5</sub> structure is -58° and in the ATX-pThr structure -59°, respectively. These different χ<sub>1</sub> angles translate into a 1.8 Å movement of the O<sub>γ</sub> of Thr209 towards the Zn<sub>1</sub> in the ATX-VO<sub>5</sub> structure relative to the ATX-PO<sub>4</sub> structure (Fig. 4), while at the same time it moves away from the Zn<sub>2</sub> atom. In the ATX-pThr structure the O<sub>γ</sub> of Thr209 moves 0.4 Å backwards relative to the observed position in the ATX-VO<sub>5</sub> structure. The difference in the χ<sub>1</sub> angles do not reflect the observed 0.4 Å movement of the O<sub>γ</sub> of Thr209, but this movement is mediated by changes along the backbone. A similar albeit smaller movement of the active site nucleophile has also been observed in the vanadate AP complex structure<sup>33</sup> (PDB: 1B8J). In this structure the nucleophile of Ser102 had moved 0.8 Å towards the Zn<sub>1</sub> site compared to the non-covalently bound phosphate complex<sup>13,33</sup> (PDB: 1ALK). The close distance of the O<sub>γ</sub> nucleophile to Zn<sub>2</sub> is important to allow it to perform the nucleophilic attack. It remains to be investigated if movements of the same magnitude are also taking place when the actual substrate hydrolysis takes place, but our observations are well in line with the well-established first nucleophilic attack and can serve well to rearrange the positioning of the intermediate to come in place for the second nucleophilic attack.

### Mechanistic Implications for Catalysis by ATX

Phosphodiesterases are considered to have an associative mechanism, where no significant bond cleavage of the leaving group occurs while the new bond to the nucleophile is established<sup>25, 26</sup>. The transition-state mimic structure of ATX-VO<sub>5</sub> strongly suggests an associative catalytic mechanism for ATX, as it is of a pentacovalent nature. According to this scenario, the phosphorous atom of the substrate is nucleophilically attacked by the O<sub>γ</sub> of Thr209, which leads to the destabilization of the double-bonded oxygen and the formation of a pentacovalent transition state. The bond between the phosphorous atom and the oxygen atom, which bridges the R-group, is then cleaved, allowing departure of the R-group. The next reaction step in the mechanism is the nucleophilic water-based attack on the substrate-

nucleophile intermediate, to form the product and release the R group. Our ATX-pThr structure likely represents the reaction state prior to the attack on the phosphorylated Thr209. The Zn<sub>1</sub> coordinated water molecule is optimally positioned to fulfil this nucleophilic bimolecular S<sub>N</sub>2 attack on the intermediate. The stereochemistry of the phosphate ion supports this concept, as it could be inverted between the ATX-PO<sub>4</sub> and the ATX-pThr structure (Fig. 5).

## CONCLUSIONS

We presented two crystal structures of ATX that we postulate they represent snapshots of the ATX catalytic cycle. The ATX-VO<sub>5</sub> structure mimics the transition state of the enzymatic reaction after the nucleophilic attack onto the substrate. The transition state analogue orthovanadate adopts in this structure a pentacovalent configuration. The ATX-pThr structure represents the reaction state prior to the second nucleophilic attack of an activated water molecule on the phosphorylated Thr209 to form the product. We observe specific conformational changes in the active site of these structures, which likely facilitate the positioning of the real substrates for catalysis. Our structures support the concept of an associative two-step in-line mechanism for the substrate hydrolysis by ATX.

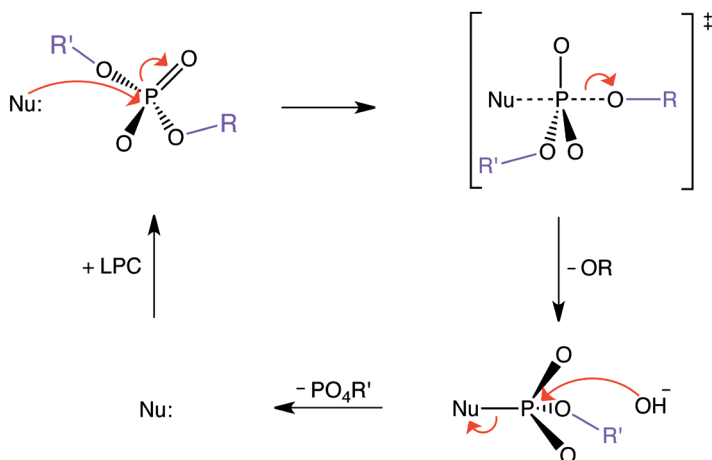


Fig. 5: Suggested catalytic mechanism of ATX.

## ACKNOWLEDGEMENTS

Crystallographic experiments were performed at the PX beamline at the Swiss Light Source, Paul Scherrer Institut, Villigen, Switzerland and at the European Synchrotron Radiation Facility beamline ID29. A.P. and J. H. would like to thank the beamline scientists for technical support. J.H. would also like to thank Drs. Mariano Stornaiuolo, Prakash Rucktooa and Robbie Joosten for helpful discussion and technical advice and the NKI Protein Facility for infrastructure. This work was supported by a KWF grant for AP and an NWO-TOP grant to A.P. and W.H.M..

## REFERENCES

1. Stracke, M. L., Krutzsch, H. C., Unsworth, E. J., Arestad, A., Ciocco, V., Schiffmann, E. & Liotta, L. A. (1992). Identification, purification, and partial sequence analysis of autotaxin, a novel motility-stimulating protein. *J Biol Chem* **267**, 2524-9.
2. Stefan, C., Jansen, S. & Bollen, M. (2005). NPP-type ectophosphodiesterases: unity in diversity. *Trends Biochem Sci* **30**, 542-50.
3. Tokumura, A., Majima, E., Kariya, Y., Tominaga, K., Kogure, K., Yasuda, K. & Fukuzawa, K. (2002). Identification of human plasma lysophospholipase D, a lysophosphatidic acid-producing enzyme, as autotaxin, a multifunctional phosphodiesterase. *J Biol Chem* **277**, 39436-42.
4. Umezu-Goto, M., Kishi, Y., Taira, A., Hama, K., Dohmae, N., Takio, K., Yamori, T., Mills, G. B., Inoue, K., Aoki, J. & Arai, H. (2002). Autotaxin has lysophospholipase D activity leading to tumor cell growth and motility by lysophosphatidic acid production. *J Cell Biol* **158**, 227-33.
5. Noguchi, K., Herr, D., Mutoh, T. & Chun, J. (2009). Lysophosphatidic acid (LPA) and its receptors. *Curr Opin Pharmacol* **9**, 15-23.
6. Moolenaar, W. H. & Hla, T. (2012). SnapShot: Bioactive lysophospholipids. *Cell* **148**, 378-378 e2.
7. Moolenaar, W. H. & Perrakis, A. (2011). Insights into autotaxin: how to produce and present a lipid mediator. *Nat Rev Mol Cell Biol* **12**, 674-9.
8. Hausmann, J., Kamtekar, S., Christodoulou, E., Day, J. E., Wu, T., Fulkerson, Z., Albers, H. M., van Meeteren, L. A., Houben, A. J., van Zeijl, L., Jansen, S., Andries, M., Hall, T., Pegg, L. E., Benson, T. E., Kasiem, M., Harlos, K., Kooi, C. W., Smyth, S. S., Ovaa, H., Bollen, M., Morris, A. J., Moolenaar, W. H. & Perrakis, A. (2011). Structural basis of substrate discrimination and integrin binding by autotaxin. *Nat Struct Mol Biol* **18**, 198-204.
9. Nishimasu, H., Okudaira, S., Hama, K., Mihara, E., Dohmae, N., Inoue, A., Ishitani, R., Takagi, J., Aoki, J. & Nureki, O. (2011). Crystal structure of autotaxin and insight into GPCR activation by lipid mediators. *Nat Struct Mol Biol* **18**, 205-12.
10. Zalatan, J. G., Fenn, T. D., Brunger, A. T. & Herschlag, D. (2006). Structural and functional comparisons of nucleotide pyrophosphatase/phosphodiesterase and alkaline phosphatase: implications for mechanism and evolution. *Biochemistry* **45**, 9788-803.
11. Albers, H. M., Dong, A., van Meeteren, L. A., Egan, D. A., Sunkara, M., van Tilburg, E. W., Schuurman, K., van Tellingén, O., Morris, A. J., Smyth, S. S., Moolenaar, W. H. & Ovaa, H. (2010). Boronic acid-based inhibitor of autotaxin reveals rapid turnover of LPA in the circulation. *Proc Natl Acad Sci USA* **107**, 7257-62.
12. Galperin, M. Y., Bairoch, A. & Koonin, E. V. (1998). A superfamily of metalloenzymes unifies phosphopentomutase and cofactor-independent phosphoglycerate mutase with alkaline phosphatases and sulfatases. *Protein Sci* **7**, 1829-35.
13. Kim, E. E. & Wyckoff, H. W. (1991). Reaction mechanism of alkaline phosphatase based on crystal structures. Two-metal ion catalysis. *J Mol Biol* **218**, 449-64.
14. Gijssbers, R., Ceulemans, H., Stalmans, W. & Bollen, M. (2001). Structural and catalytic similarities between nucleotide pyrophosphatases/phosphodiesterases and alkaline phosphatases. *J Biol Chem* **276**, 1361-8.
15. Coleman, J. E. (1992). Structure and mechanism of alkaline phosphatase. *Annu Rev Biophys Biomol Struct* **21**, 441-83.
16. Cleland, W. W. & Hengge, A. C. (1995). Mechanisms of phosphoryl and acyl transfer. *FASEB J* **9**, 1585-94.
17. Cassano, A. G., Anderson, V. E. & Harris, M. E. (2002). Evidence for direct attack by hydroxide in phosphodiester hydrolysis. *J Am Chem Soc* **124**, 10964-5.
18. Lopez-Canut, V., Roca, M., Bertran, J., Moliner, V. & Tunon, I. (2010). Theoretical study of phosphodiester hydrolysis in nucleotide pyrophosphatase/phosphodiesterase. Environmental effects on the reaction mechanism. *J Am Chem Soc* **132**, 6955-63.
19. Lassila, J. K., Zalatan, J. G. & Herschlag, D. (2011). Biological phosphoryl-transfer reactions: understanding mechanism and catalysis. *Annu Rev Biochem* **80**, 669-702.
20. Hausmann, J., Christodoulou, E., Kasiem, M., De Marco, V., van Meeteren, L. A., Moolenaar, W. H., Axford, D., Owen, R. L., Evans, G. & Perrakis, A. (2010). Mammalian cell expression, purification, crystallization and microcrystal data collection of autotaxin/ENPP2, a secreted mammalian glycoprotein. *Acta Crystallographica Section F* **66**, 1130-1135.

21. Day, J. E., Hall, T., Pegg, L. E., Benson, T. E., Hausmann, J. & Kamtekar, S. (2010). Crystallization and preliminary X-ray diffraction analysis of rat autotaxin. *Acta Crystallographica Section F* **66**, 1127-1129.
22. Leslie, A. G. W. & Powell, H. R. (2007). Processing Diffraction Data with Mosflm. *Evolving Methods for Macromolecular Crystallography* **245**, 41-51.
23. Evans, P. (2006). Scaling and assessment of data quality. *Acta Crystallogr D Biol Crystallogr* **62**, 72-82.
24. McCoy, A. J. (2007). Solving structures of protein complexes by molecular replacement with Phaser. *Acta Crystallogr D Biol Crystallogr* **63**, 32-41.
25. Emsley, P. & Cowtan, K. (2004). Coot: model-building tools for molecular graphics. *Acta Crystallogr D Biol Crystallogr* **60**, 2126-32.
26. Murshudov, G. N., Vagin, A. A. & Dodson, E. J. (1997). Refinement of macromolecular structures by the maximum-likelihood method. *Acta Crystallogr D Biol Crystallogr* **53**, 240-55.
27. Joosten, R. P., Joosten, K., Murshudov, G. N. & Perrakis, A. PDB\_REDO: constructive validation, more than just looking for errors. *Acta Crystallogr D Biol Crystallogr* **68**, 484-96.
28. Davis, I. W., Leaver-Fay, A., Chen, V. B., Block, J. N., Kapral, G. J., Wang, X., Murray, L. W., Arendall, W. B., 3rd, Snoeyink, J., Richardson, J. S. & Richardson, D. C. (2007). MolProbity: all-atom contacts and structure validation for proteins and nucleic acids. *Nucleic Acids Res* **35**, W375-83.
29. Kabsch, W. Xds. *Acta Crystallogr D Biol Crystallogr* **66**, 125-32.
30. Murshudov, G. N., Vagin, A. A. & Dodson, E. J. (1997). Refinement of macromolecular structures by the maximum-likelihood method. *Acta Crystallogr D Biol Crystallogr* **53**, 240-255.
31. Crans, D. C., Smee, J. J., Gaidamauskas, E. & Yang, L. (2004). The chemistry and biochemistry of vanadium and the biological activities exerted by vanadium compounds. *Chem Rev* **104**, 849-902.
32. Davies, D. R. & Hol, W. G. (2004). The power of vanadate in crystallographic investigations of phosphoryl transfer enzymes. *FEBS Lett* **577**, 315-21.
33. Holtz, K. M., Stec, B. & Kantrowitz, E. R. (1999). A model of the transition state in the alkaline phosphatase reaction. *J Biol Chem* **274**, 8351-4.
34. Hulett, F. M., Kim, E. E., Bookstein, C., Kapp, N. V., Edwards, C. W. & Wyckoff, H. W. (1991). Bacillus subtilis alkaline phosphatases III and IV. Cloning, sequencing, and comparisons of deduced amino acid sequence with Escherichia coli alkaline phosphatase three-dimensional structure. *J Biol Chem* **266**, 1077-84.
35. Gettins, P. & Coleman, J. E. (1983). 31P nuclear magnetic resonance of phosphoenzyme intermediates of alkaline phosphatase. *J Biol Chem* **258**, 408-16.
36. Murphy, J. E., Stec, B., Ma, L. & Kantrowitz, E. R. (1997). Trapping and visualization of a covalent enzyme-phosphate intermediate. *Nat Struct Biol* **4**, 618-22.
37. Wang, J. & Kantrowitz, E. R. (2006). Trapping the tetrahedral intermediate in the alkaline phosphatase reaction by substitution of the active site serine with threonine. *Protein Sci* **15**, 2395-401.
38. Mosca, R. & Schneider, T. R. (2008). RAPIDO: a web server for the alignment of protein structures in the presence of conformational changes. *Nucleic Acids Res* **36**, W42-6.
39. Zalatan, J. G. & Herschlag, D. (2006). Alkaline phosphatase mono- and diesterase reactions: comparative transition state analysis. *J Am Chem Soc* **128**, 1293-303.





A large, light gray outline of the number 5 is centered on the page. The number is composed of several straight lines forming a stylized shape. The top part is a horizontal bar, followed by a vertical line on the left, a horizontal line on the right, and a curved line that loops back to the left and then down to the right, forming a large 'S' shape.

# SUMMARY AND DISCUSSION

## SUMMARY AND DISCUSSION

The present thesis concerns the structure of autotaxin (ATX) alone and in complex with a small-molecule inhibitor (HA155), as well as its biochemical characterization. ATX was originally discovered as an “autocrine motility factor” from melanoma cells, more than two decades ago, but its biochemical function remained elusive. It took another decade to show that ATX functions as a lysophospholipase D that generates the lipid growth factor LPA. It is now known that ATX is essential for embryonic development, while numerous studies associate the ATX-LPA signaling axis with various diseases, including cancer, fibrosis, neuropathic pain and immune-mediated diseases<sup>1</sup>. This makes ATX an interesting target for therapeutic intervention, and pharmaceutical companies and academia invest great effort into the development of ATX inhibitors; the number of ATX inhibitors is increasing steadily. Insight into the structure of ATX will help to accelerate the development of ATX inhibitors as therapeutic agents. Here I briefly summarize and discuss the results of my thesis work.

### Crystallization and Structure Determination of ATX

To optimize crystallisation conditions for a large protein like ATX, basic requirements towards sample preparation have to be met. The protein sample has to be expressed in high quantity and quality. Mammalian cell expression systems allow large-scale production of secreted proteins<sup>2</sup>, such as ATX. Combining this approach with the Flp-In™ technology<sup>3</sup>, optimizes the time- and cost-efficiency even further, as intensive preparation labour for transient transfection is omitted and reproducibility of the expression is more reliable. Under these conditions, enzymatically active ATX (from rat) was expressed in amounts suitable for crystallisation experiments (**Chapter 2**).

The sample used in crystallisation screens has usually more than 95% purity and has to be concentrated to 5-10 mg/ml. The introduction of a size exclusion chromatography step improved the sample purity and revealed new crystallisation conditions. Further optimization (by adding 0.3 M sodium thiocyanate) yielded crystals that diffracted to high resolution

The size and shape of the crystal and the experimental set-up provided by individual synchrotron beam lines are important parameters for structure determination. The development of tuneable microfocus beams with different beam sizes in combination with a grid-scan procedure, offers the possibility to optimize data collection from thin plate-like crystals (Chapter 2)<sup>4</sup>. Changes in crystal size that appear during data collection could be accounted for by three-dimensional data collection software, which considers the volume, the variation of beam sizes and exposure times, to routinely collect data with higher efficiency (Chapter 2).

### The structure of ATX

To understand the function of ATX in more detail, the full length structure of rat ATX alone and in complex with the inhibitor HA155 were determined (**Chapter 3**). The structures obtained gave important new insights into the domain organization of ATX and ATX catalysis, however they also gave rise to new questions.

The crystal structure revealed that the catalytic PDE domain is the central element of the domain architecture of ATX. The N-terminal SMB1 and SMB2 domains are located on one side of the PDE domain. On the opposite side, the C-terminal NUC domain forms a large interface with

the central PDE domain. The close relative of ATX, ENPPI, also possesses this large interface between the PDE and NUC domain, but the SMB domains of ENPPI show a complete different orientation and a higher degree of flexibility compared to the SMB domains of ATX. These observations suggest functional differences between the SMB domains of ENPPI and ATX.

The catalytic site of ATX is similar to that in ENPPI and other members of the alkaline phosphatase superfamily<sup>5</sup>. We could show that residue Asn230 is crucial for catalysis by ATX. In the alkaline phosphatase of *E. coli* this asparagine is exchanged for an arginine (**Chapter 4**). Interestingly, the latter enzyme is a phosphomonesterase, suggesting that the substrate specificity is alternated by the substitution of asparagine to arginine, as indicated by others<sup>6</sup>. It would be of interest to examine how an Asn230 to arginine mutant of ATX would alter phosphomonesterase vs. phosphodiesterase activity.

The crystal structures of ATX revealed a hydrophobic pocket, which is adjacent to the active site and not present in ENPPI<sup>5</sup>. The biochemical analysis of ATX mutants, described in Chapter 3, suggests that the pocket accommodates the aliphatic chain of lipid substrates. This conclusion is supported by concurrent crystallographic complex data of ATX with various LPA species, where the aliphatic chains are bound in the pocket<sup>7</sup>. Additionally, the hydrophobic pocket has been observed to be lockable by the fluorobenzene ring of HA155. However, it would be of great interest to see where and how other inhibitors, such as PF8380, bind to ATX and how they generate their specificity towards ATX.

An open tunnel near the hydrophobic pocket of ATX was an unexpected and intriguing observation in the crystal structure. The tunnel is formed by a tight interaction between the PDE and SMB domains and adjacent to both the hydrophobic pocket and the active site. The tunnel might be involved in product release or substrate entry (Chapter 3). However, so far neither crystallographic nor biochemical data could hint at a functional role for the tunnel. Therefore, the function of the tunnel remains elusive. It is not known if newly formed LPA is released from ATX and if LPA is specifically targeted to its receptors<sup>8</sup>. Further studies should address the concept of a complex between ATX and its cognate LPA receptors (LPA<sub>1-6</sub>), as well as the possible involvement of the tunnel in the delivery of LPA.

Further questions that arise from the crystal structure concern the binding of substrates, such as LPC, ATP, and FS3, for the catalysis by ATX. The key questions here are: how do these ligands bind exactly, how is the leaving group orientated? Is the tunnel also involved in the binding of either substrate or product? To address these questions, it will be necessary to use catalytically inactive ATX in co-crystallization experiments with substrates.

### ATX Interaction with the cell surface

Cells achieve specificity in their signaling networks by organizing discrete subsets of proteins in space and time<sup>9</sup>. A spatial and temporal recruitment of ATX to LPA-responsive cells can be achieved via the interaction with cell-surface molecules. The binding of ATX to cell-surface integrins described in Chapter 3 and elsewhere<sup>10</sup>, is an important observation for the understanding of ATX-driven LPA signaling. The results in Chapter 3 show that ATX binds to integrin  $\beta 3$  subunits via its N-terminal SMB domains. Recently it was shown that the G-protein subunit  $G_{\alpha 13}$  binds to  $\beta 3$  of the platelet integrin  $\alpha IIb\beta 3$  and thereby triggers an inside-out signaling event, leading the modulation of ligand binding affinity. Interestingly,  $G_{\alpha 13}$  is coupled

to the “platelet-type” LPA receptor LPA<sub>5</sub><sup>11</sup>. LPA stimulation of platelets and activation of LPA<sub>5</sub> could stimulate G<sub>α13</sub> dependent inside-out signaling via αIIbβ3, which might alter the binding specificity of ATX to αIIbβ3. Future investigations should test hypothesis.

Moreover, ATX immobilization can also be achieved by binding to the cell-surface heparan sulfate proteoglycans. This binding appears to be isoform-specific, as only the ATXα isoform is a heparin-binding protein (Houben et al., JBC 288: 510-519, 2013). Thus, ATX can use distinct mechanisms to bind to target cells and deliver LPA to the cell surface.

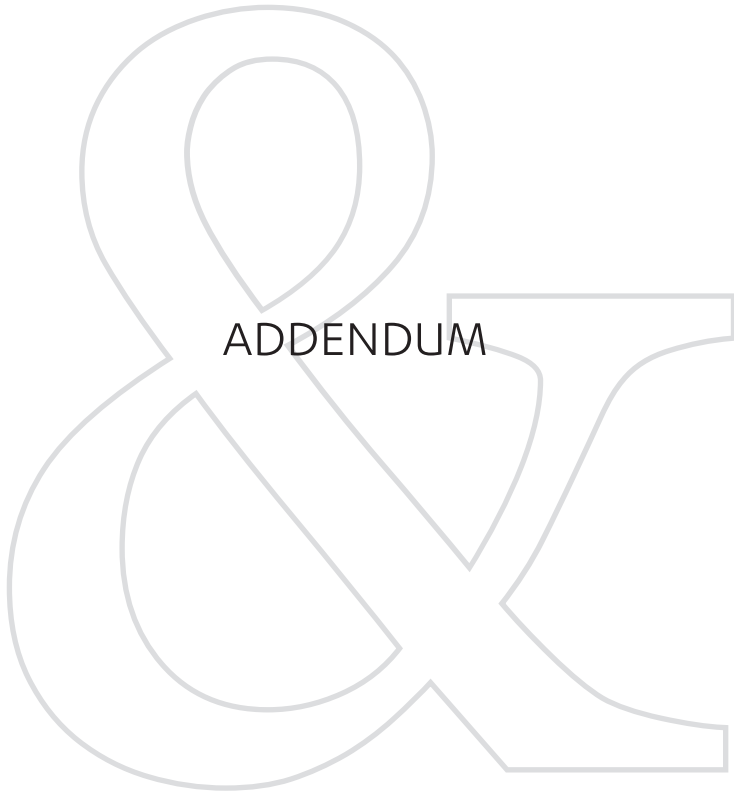
## PERSPECTIVES

ATX is a fascinating and vital enzyme for life that is involved in many biological processes with its intrinsic capability to generate LPA under physiological and pathophysiological conditions. Due to the recent structural insights of ATX, we start to understand more and more the biology of ATX and the implied LPA axis. Additionally, the determination of the ENPP1 structure and hopefully more members of the ENPP family will deepen our knowledge about the biochemical specificity of these family members in general and for ATX in particular. The ever increasing list of publications on the ATX-LPA signaling axis reflect the enormous scientific efforts that are undertaken to understand this signaling axis in more detail, in order to address it with therapeutic intervention in the near future.

## REFERENCES

1. Moolenaar, W.H. & Hla, T. SnapShot: Bioactive lysophospholipids. *Cell* **148**, 378-378 e2 (2012).
2. Aricescu, A.R., Lu, W. & Jones, E.Y. A time- and cost-efficient system for high-level protein production in mammalian cells. *Acta Crystallogr D Biol Crystallogr* **62**, 1243-50 (2006).
3. O'Gorman, S., Fox, D.T. & Wahl, G.M. Recombinase-mediated gene activation and site-specific integration in mammalian cells. *Science* **251**, 1351-5 (1991).
4. Aishima, J. et al. High-speed crystal detection and characterization using a fast-readout detector. *Acta Crystallogr D Biol Crystallogr* **66**, 1032-5 (2010).
5. Jansen, S. et al. Structure of NPPI, an Ecto-nucleotide Pyrophosphatase/Phosphodiesterase Involved in Tissue Calcification. *Structure* (2012).
6. Zalatan, J.G., Fenn, T.D., Brunger, A.T. & Herschlag, D. Structural and functional comparisons of nucleotide pyrophosphatase/phosphodiesterase and alkaline phosphatase: implications for mechanism and evolution. *Biochemistry* **45**, 9788-803 (2006).
7. Nishimasu, H. et al. Crystal structure of autotaxin and insight into GPCR activation by lipid mediators. *Nat Struct Mol Biol* **18**, 205-12 (2011).
8. Moolenaar, W.H. & Perrakis, A. Insights into autotaxin: how to produce and present a lipid mediator. *Nat Rev Mol Cell Biol* **12**, 674-9 (2011).
9. Good, M.C., Zalatan, J.G. & Lim, W.A. Scaffold proteins: hubs for controlling the flow of cellular information. *Science* **332**, 680-6 (2011).
10. Kanda, H. et al. Autotaxin, an ectoenzyme that produces lysophosphatidic acid, promotes the entry of lymphocytes into secondary lymphoid organs. *Nat Immunol* **9**, 415-23 (2008).
11. Yanagida, K. & Ishii, S. Non-Edg family LPA receptors: the cutting edge of LPA research. *J Biochem* **150**, 223-32 (2011).







## NEDERLANDSE SAMENVATTING

Autotaxin (ATX) werd meer dan twee decennia geleden ontdekt als een “autocrine motility factor” afkomstig van melanomacellen, maar de precieze biochemische functie van ATX was in eerste instantie onbekend. Het duurde echter nog ruim een decennium voordat duidelijk werd dat ATX een lysofosfolipase D is dat zorgt voor de productie van lysofosfatidezuur (LPA), een lipide groeifactor, en vrij choline door de hydrolyse van lysofosfatidylcholine (LPC). Tegenwoordig weten we dat ATX essentieel is voor de embryonale ontwikkeling, terwijl talrijke onderzoeken de ATX-LPA “signaal-as” associëren met verschillende aandoeningen, waaronder kanker, fibrose, neuropathische pijn en auto-immuun ziektes zoals reumatoïde artritis en chronische ontsteking. ATX is derhalve een belangrijk doelwit voor therapeutische interventie, en zowel de farmaceutische industrie als de academische wereld hebben veel middelen ingezet voor de ontwikkeling van ATX remmers. Dit proefschrift bevat de structurele en biochemische karakterisatie van ATX.

Het eerste hoofdstuk is een algemene introductie tot ATX met nadruk op de structuur-functie relaties van het enzym. Het tweede hoofdstuk beschrijft methodes voor de expressie en opzuivering van ATX in hoeveelheden en kwaliteit die geschikt zijn voor zowel Röntgenkristallografie als voor datacollectie van microkristallen. Verder worden geavanceerde datacollectie strategieën behandeld voor dunne plaatachtige kristallen.

Het derde hoofdstuk bevat de structurele analyse van ATX in zijn apo-vorm en in complex met de potente remmer HA155. Verder beschrijft dit hoofdstuk hoe ATX de diverse substraten onderscheidt en hydrolyseert. Bovendien laten we zien hoe ATX aan bloedplaatjes bindt via integrine  $\beta 3$  op het celoppervlak.

Het vierde hoofdstuk beschrijft de katalytische mechanisme van ATX in verder detail met behulp van Röntgenkristallografie. De resultaten ondersteunen het concept van een “associative two-step in-line displacement mechanism” voor ATX.

De verkregen resultaten verschaffen nieuwe inzichten in de functie van ATX en de ATX-LPA signaal-as, en zullen ook de ontwikkeling van therapeutische remmers van ATX bespoedigen.





## CURRICULUM VITAE

Jens Hausmann was born on the 24<sup>th</sup> of August in 1979 in Bochum, Germany. In 2000 he obtained the higher education entrance qualification from Private School Schloss Buldern in Buldern, Germany. In October 2002, he started to study biology at the Westphalian Wilhelms-University (WWU) in Münster, Germany. In the beginning of 2004, he became student assistance at the Institute of Human Genetics at the Medical Department of the WWU and he continued this work till the end of 2006. Here, he performed additionally several extracurricular cell biological internships in the context of polycystic kidney disease under the supervision of Dr. Petra Pennekamp. Furthermore, he gained experience in the topic of pathogen-host interaction during a 3-month extracurricular internship in the lab of Prof. Dr. Berenike Maier at the Institute of Molecular Cellbiology in the Biology Department of the WWU. From February to June 2007 Jens worked in the lab of Prof. Dr. Ursula Jakob on the structural basis of the activation mechanism of Hsp33 in the Department of Molecular, Cellular and Developmental Biology at University of Michigan in Ann Arbor, United States of America. In December 2007, he started an internship for 10 month in the group of Dr. Stefan Rüdiger in the Bijvoet Center for Biomolecular Research of Utrecht University on the characterization of Hsp90 by segmental isotope labeling, as an external Diploma student in Utrecht, The Netherlands. In December 2008, Jens finished his diploma studies at the WWU and started in the same month with his PhD-project in the group of Dr. Anastassis Perrakis at the Netherlands Cancer Institute in Amsterdam, The Netherlands.





## LIST OF PUBLICATIONS

1. **Hausmann J**, van Zeijl L, Moolenaar WH, and Perrakis A. Structural Snapshots of Autotaxin/ENPP2 and their Implications for Catalysis. To be submitted to *Journal of Molecular Biology*
2. Houben AJ, van Wijk XM, van Meeteren LA, van Zeijl L, van de Westerloo EM, **Hausmann J**, Fish A, Perrakis A, van Kuppevelt TH, and Moolenaar WH. The Polybasic Insertion in Autotaxin alpha Confers Specific Binding to Heparin and Cell Surface Heparan Sulfate Proteoglycans. *The Journal of Biological Chemistry* 288: 510-519, 2013.
3. **Hausmann J**, Perrakis A, and Moolenaar WH. Structure-function relationships of autotaxin, a secreted lysophospholipase D. *Advances in Biological Regulation* 53 (2013) 112–117.
4. Kryshtafovych A, Moulton J, Bartual SG, Bazan JF, Berman H, Casteel DE, Christodoulou E, Everett JK, **Hausmann J**, Heidebrecht T, Hills T, Hui R, Hunt JF, Seetharaman J, Joachimiak A, Kennedy MA, Kim C, Lingel A, Michalska K, Montelione GT, Otero JM, Perrakis A, Pizarro JC, van Raaij MJ, Ramelot TA, Rousseau F, Tong L, Wernimont AK, Young J, and Schwede T. Target highlights in CASP9: Experimental target structures for the critical assessment of techniques for protein structure prediction. *Proteins* 79 Suppl 10: 6-20, 2011.
5. Albers HM, Hendrickx LJ, van Tol RJ, **Hausmann J**, Perrakis A, and Ovaa H. Structure-based design of novel boronic acid-based inhibitors of autotaxin. *Journal of Medicinal Chemistry* 54: 4619-4626, 2011.
6. **Hausmann J**, Kamtekar S, Christodoulou E, Day JE, Wu T, Fulkerson Z, Albers HM, van Meeteren LA, Houben AJ, van Zeijl L, Jansen S, Andries M, Hall T, Pegg LE, Benson TE, Kasiem M, Harlos K, Kooi CW, Smyth SS, Ovaa H, Bollen M, Morris AJ, Moolenaar WH, and Perrakis A. Structural basis of substrate discrimination and integrin binding by autotaxin. *Nature Structural & Molecular Biology* 18: 198-204, 2011.
7. Karagoz GE, Duarte AM, Ippel H, Utrecht C, Sinnige T, van Rosmalen M, **Hausmann J**, Heck AJ, Boelens R, and Rudiger SG. N-terminal domain of human Hsp90 triggers binding to the cochaperone p23. *Proceedings of the National Academy of Sciences of the United States of America* 108: 580-585, 2011.
8. **Hausmann J**, Christodoulou E, Kasiem M, De Marco V, van Meeteren LA, Moolenaar WH, Axford D, Owen RL, Evans G, and Perrakis A. Mammalian cell expression, purification, crystallization and microcrystal data collection of autotaxin/ENPP2, a secreted mammalian glycoprotein. *Acta Crystallographica Section F* 66: 1130-1135, 2010.
9. Day JE, Hall T, Pegg LE, Benson TE, **Hausmann J**, and Kamtekar S. Crystallization and preliminary X-ray diffraction analysis of rat autotaxin. *Acta Crystallographica Section F* 66: 1127-1129, 2010.
10. Cremers CM, Reichmann D, **Hausmann J**, Ilbert M, and Jakob U. Unfolding of metastable linker region is at the core of Hsp33 activation as a redox-regulated chaperone. *The Journal of Biological Chemistry* 285: 11243-11251, 2010.





## ACKNOWLEDGEMENTS

I WISH TO EXPRESS MY GRATITUDE TO THOSE WHO HAVE CONTRIBUTED TO THIS THESIS



